# Whiskers of IB, VIII Metals and Their Alloys: Synthesis and Microscopic Studies

Zur Erlangung des akademischen Grades
**Doktor der Ingenieurwissenschaften**
der Fakultät für Maschinenbau
Karlsruher Institut für Technologie (KIT)

genehmigte
**Dissertation**
von

Wenting Huang
aus Shaxian, China

| | |
|---|---|
| Tag der mündlichen Prüfung: | 24.05.2017 |
| Hauptreferent: | Prof. Dr. rer. nat. Oliver Kraft |
| Korreferent: | Prof. Dr. Eugen Rabkin |

# Abstract

This work focuses on the whiskers of IB, VIII metals and their alloys. The whiskers were synthesized using physical vapor deposition. Their structural, morphological and magnetic properties were studied by electron microscopy techniques. Special effort is made to understand the growth mechanism and growth process as well as the effect of size on the whisker properties.

Most of the whiskers were single crystal structures without any defects. Their cross-sectional area followed what is predicted by the Wulff theorem. Some of the Ni whiskers were grown with a Σ3 twin, its twin boundary being parallel to the whisker axis. The stable crystal structure of Co whiskers at ambient condition was FCC. HCP crystals can also be observed in the FCC whiskers, in the form of microtwins. They were the result of the fast kinetic growth and of the incomplete phase transformation during the cool-down process. The HCP phase was eliminated by slow cool-down after annealing and did not appear upon reheating. The FCC-HCP transformation can be promoted by applying an external tensile stress.

Both root and tip growth were observed. Root growth was the default mode of growth, since the majority of the adatoms were found at the surface. Root growth was directly observed during the growth of whisker heterostructures on Si substrates. It was also indirectly proven by the cross-sectional shape evolution on $FeSi_2$ whiskers. The root part of the $FeSi_2$ whiskers had a smaller diameter and a different shape compared to the rest, due to the lack of radial overgrowth as it was freshly grown. When incorporation at the root site was not possible, tip growth was observed instead. Whisker segment formed by tip growth was often shorter, as it was mainly fueled by the adatoms directly impinged on the whisker sidewalls. The axial elongation was accompanied by the inevitable albeit often slight diameter expansion of the whiskers.

Finally, the magnetic whiskers (Fe, Ni, Co) synthesized in this work were all single domain structures. The large shape anisotropy induced by the high aspect ratio of the whiskers forced the magnetization to be aligned with the whisker axis. The direction of the magnetization may change with the shape of the nanostructures. The cross section lamella cut from a Ni whisker had its magnetization direction along the direction of the longer diagonal. Vortex state was observed in highly symmetric small platelets. Larger platelets with lower level of symmetry, on the other hand, exhibited a multi-domain structure.

# Kurzfassung

Diese Arbeit beschäftigt sich mit Haarkristallen (englisch: Whisker) der Metalle der IB und VIII Hauptgruppe, sowie deren Legierungen. Die Whisker wurden durch physikalische Gasphasenabscheidung synthetisiert. Ihre Morphologie, Gefüge und magnetischen Eigenschaften wurden mittels elektronenmikroskopischer Techniken untersucht. Besonders die Wachstumsmechanismen und –prozesse sowie die Größenabhängigkeit der Eigenschaften lagen im Augenmerk der Arbeit.

Die meisten Haarkristalle waren einkristallin und ohne Defekte. Ihre Querschnittsgeometrie entsprach der aus dem Wulff´schen Theorem vorhergesagten. Einige der Ni Whisker wiesen einen Σ3 Zwilling nach dem Wachstum auf, die Zwillingsebene war parallel zur Whiskerachse. Die stabile Co-Modifikation unter Umgebungsbedingungen ist die kubisch-flächenzentrierte (englisch: face centered cubic, FCC) Phase. Hexagonal dichtgepackte (englisch: hexagonal close packed, HCP) Kreisallstrukturen sind ebenfalls beobachtet worden, als Mikrozwillinge. Sie sind das Resultat des schnellen kinetischen Wachstums und der nichtvollständigen Phasentransformation während des Abkühlvorganges. Die HCP Phase konnte durch langsames Abkühlen nach Auslagern eliminiert werden, und trat nicht wieder bei erneutem Auslagern auf. Die FCC-HCP Phasentransformation kann durch äußere Zugspannungen eingeleitet werden.

Sowohl Spitzen als auch Fußwachstum wurde beobachtet. Fußwachstum ist die Standardvariante des Wachstums, da die Mehrheit der Adatome auf der Substratoberfläche zu finden ist. Fußwachstum konnte direkt durch das Herstellen von Heterostrukturen auf Si beobachtet werden. Es wurde auch indirekt durch die Querschnittsänderungen an $FeSi_2$ Whiskern nachgewiesen. The Fuß von $FeSi_2$ Haarkristallen ist geringer im Durchmesser und weist eine andere Form im Vergleich zum Restlichen Whisker auf. Dies ist dadurch bedingt, dass der Fuß nicht überwachsen wurde sondern im frisch gewachsenen Zustand verblieb. Wenn der Einbau nicht am Fußpunkt möglich war, dann konnte Spitzenwachstum beobachtet werden. Der Teil des Whiskers der an der Spitze wuchs ist oft kleiner, da er nur durch Adatome die direkte auf den Seitenfacetten auftrafen wachsen konnte. Das Längenwachstum war immer durch das unvermeidliche Anwachsen des Durchmessers begleitet.

Die in dieser Arbeit synthetisierten magnetischen Haarkristalle (Fe, Ni, Co) zeigten alle eine einzige magnetische Domäne. Die große Formanisotropie, aufgrund des hohen Langen zu Durchmesser Verhältnisses, zwang die Richtung der Magnetisierung sich an der Whiskerachse auszurichten. Die Richtung der Magnetisierung mag sich durch die Geometrie der Nanostruktur verändern. Die aus einem Whisker geschnittene Quer-

schnittslamelle hatte die Magnetisierungsrichtung parallel zur langen Diagonalen. Große Platten mit niedriger Symmetrie zeigen dagegen mehrere Weiß´sche Domänen.

# Acknowledgement

Immeasurable appreciation and deepest gratitude for the help and support are extended to the following people who in one way or another have contributed to making this study possible.

My highest, most respectful gratitude goes to my mentor Prof. Dr. rer. nat. Oliver Kraft, who provided me the precious opportunity to carry out this study. It was his patience, motivation, and immense knowledge that guided me through the study.

It is a genuine pleasure to express my deep sense of thanks and gratitude to Dr. Gunther Richter for his support in every stage of my research, for the most inspiring discussions and timely suggestions.

I thank profusely Prof. Dr. Eugen Rabkin for taking the time to read the manuscript and to participate in the defense of this thesis, and for his stimulating discussions on this work.

I owe a deep sense of gratitude to my collaborators, Dr. Vesna Srot from StEM group for the EELS and EDX measurements on the $FeSi_2$ whiskers, Dr. Christophe Gatel, Dr. Etienne Snoeck from CEMES-CNRS France, Dr. Zi'an Li and Dongsheng Song from ER-C Jülich for the electron holography and Lorentz microscopy experiments, and Dr. Julia Wagner from INT, KIT for the APT measurement.

None of the experimental work would have been completed without the assistance of Reinhart Völker, and Ilse Lakemeyer from the thin film laboratory, MPI. Their experience on physical deposition assured the high quality of the specimens. I am also grateful to Frank Thiele for all his help.

I am also hugely indebted to Marion Kelsch, Peter Kopold, Kersten Hahn, Ute Salzberger, Birgit Bußmann from StEM group for all their supports on sample preparations and TEM experiments, Ulrike Eigenthaler from Schütz department for the FIB sample preparation, Dr. Ruth Schwaiger for the HIM sample preparation.

I am also extremely thankful to my fellow colleague Charlotte Ensslen and Mark Wobrock for carrying out the tensile tests and XRD measurement, Christian Kappel for the exchange of ideas both inside and outside work, as well as Semanur Baylan and Lisa Weissmayer for their helpful discussion.

I would like to thank all the other people who have provided help over the course of this study. Dr. Kepeng Song, Dr. Xiaoyan Li, Dr. Xiaoke Mu, Dr. Yuren Wen, the former

colleagues from StEM group, for their help in TEM experiments and analysis, my colleagues in IAM-WBM, especially our secretaries, Karin Mäule and Jana Herzog for their unwavering support, and all the other Chinese colleagues in the MPI, without them, the years of study would not be as fun and enjoyable.

Last but not least, I would like to thank my parents for their unfailing support and continuous encouragement throughout the years of study and my life in general.

# Table of contents

**Abstract** ..... i

**Kurzfassung** ..... iii

**Acknowledgement** ..... v

**Table of contents** ..... vii

**Abbreviations** ..... ix

**1 Introduction and Motivation** ..... 1

**1.1 Motivation and Background** ..... 1

**1.2 Overview of the Thesis** ..... 2

**1.3 Nucleation and Growth Mechanism** ..... 3

1.3.1 Screw Dislocation Theory ..... 3

1.3.2 Nucleation in Thin Film Growth ..... 5

1.3.3 Kinetic Growth Model ..... 8

1.3.4 Our Previous Studies ..... 9

**1.4 Size Related Properties of Whiskers** ..... 10

1.4.1 Mechanical Properties ..... 11

1.4.2 Phase Transformation ..... 11

1.4.3 Magnetic Properties ..... 13

1.4.4 Others ..... 22

**2 Experimental Methods** ..... 25

**2.1 PVD and Whisker Growth** ..... 25

2.1.1 Experimental Setup ..... 25

2.1.2 Sample Preparations ..... 26

**2.2 Scanning Electron Microscopy** ..... 28

**2.3 Transmission Electron Microscopy** ..... 29

2.3.1 Bright Field and Dark Field Imaging ..... 31

2.3.2 High-Resolution TEM ..... 32

2.3.3 STEM and HAADF ..... 33

2.3.4 X-ray Energy-Dispersive Spectroscopy ..... 34

2.3.5 Electron Energy Loss Spectroscopy ..... 34
**2.4 Electron Holography ..... 35**
**3 Morphology and Crystal Structure ..... 39**
**3.1 Whiskers of IB Metals and Alloy ..... 39**
3.1.1 Cu ..... 39
3.1.2 Cu-Si ..... 42
3.1.3 Ag ..... 44
**3.2 Whiskers of VIII Metals and Alloy ..... 48**
3.2.1 Ni ..... 48
3.2.2 Co ..... 53
3.2.3 Fe ..... 57
3.2.4 Fe-Si ..... 61
**3.3 Whisker Heterostructures ..... 67**
3.3.1 Cu-Fe ..... 68
3.3.2 Cu-Fe-Si ..... 71
3.3.3 Cu-Ni ..... 74
3.3.4 Cu-Ni-Si ..... 75
3.3.5 Au-Ni ..... 76
3.3.6 Fe-Cu ..... 78
3.3.7 Ni-Ag ..... 79
**4 Size Effects of Whiskers ..... 81**
**4.1 Phase Transformation of Co Whiskers ..... 81**
**4.2 Magnetic Domain Structures ..... 91**
**5 Discussion: Growth Mechanism and Process ..... 101**
**5.1 Conditions for Whisker Growth ..... 101**
**5.2 Whisker Growth Mechanism: Incorporation Site ..... 103**
**5.3 Defects, Shape and Oxidation ..... 106**
**6 Summary ..... 109**
**Bibliography ..... 113**

# Abbreviations

| | |
|---|---|
| ADF | Annular Dark Field |
| APT | Atom Probe Tomography |
| BCC | Body Centered Cubic |
| BCML | Block Copolymer Micelle Lithography |
| BF | Bright Field |
| DF | Dark Field |
| DP | Diffraction Pattern |
| EDX | Energy-Dispersive X-ray Spectroscopy |
| EELS | Electron Energy Loss Spectroscopy |
| FCC | Face Centered Cubic |
| FIB | Focused Ion Beam |
| HAADF | High-Angle Annular Dark Field |
| HCP | Hexagonal Close Packed |
| HIM | Helium Ion Microscope |
| HR | High-Resolution |
| MAG | MAGnetic field |
| MBE | Molecular Beam Epitaxy |
| MIP | Mean Inner Potential |
| PVD | Physical Vapor Deposition |
| SEM | Scanning Electron Microscope |
| STEM | Scanning Transmission Electron Microscope |
| STO | Strontium Titanium Oxide ($SrTiO_3$) |
| TEM | Transmission Electron Microscope |

# 1 Introduction and Motivation

## 1.1 Motivation and Background

The intensive research on “Nanotechnology” was inspired by Richard Feynman’s famous 1959 lecture *There is plenty of room at the bottom* [1], but the term "nanotechnology" was actually coined by the Japanese scientist Norio Taniguchi in 1974 [2]. Coincidently, K. Eric Drexler also used the term in his book ‘Engines of Creation: The Coming Era of Nanotechnology’ published in 1986 [3]. The concept of nanotechnology is to manipulate atoms or molecules to achieve peculiar properties unimaginable with bulk materials. The invention of scanning tunneling microscope (STM) in 1981 by Gerd Binnig and Heinrich Rohrer [4] was the first step to bring the nanotechnology concept into reality. 8 years later, the manipulation of atoms was realized by Don Eigler. Another important milestone in the path of nanotechnology is the discovery of carbon nanotubes. It was to synthesize (nano-) functional materials based on carbon nanotubes that has motivated the development of many groundbreaking approaches, some of which still hold their significance as of today [5–8].

Over the past 20 years, increasing amount of research effort has been devoted to the exploration of the world at the nanoscale. Some of the applications have already been changing the way we live and the world as we know. Nanomaterial refers to materials with at least one of their dimension in the nanometer range. This includes the so-called 0D, 1D and 2D nanomaterials (0, 1, 2 refers to the number of dimensions not in the nanometer range), with some well-known examples such as nanoparticles, nanowires and nano-sized thin films. Peculiar properties emerge as the result of the downsizing dimensions. High aspect ratios and high surface to volume ratio may give rise to enhanced surface effects such as higher sensitivity and higher reactivity [9–12]. For very small size, quantum confinement becomes visible which in turn changes the thermal [13,14], electrical and optical properties [15–17] of the material. Last but not least, excellent mechanical performances have been reported on nanocrystalline materials thanks to their low dislocation density and high grain boundary ratio [18,19].

Nanowire is perhaps one of the most studied nanomaterials in the past decade. Most of the nanowires being studied today are semiconductor nanowires. They are compatible with the booming microelectronics industry and have already shown promising future in other domains such as optoelectronics and biosensors [12,15,17]. Another important class of nanowires is the one of metallic nanowires. They are expected to be used as the interconnections in future nano-sized integrated circuits, but are also deemed to play an important role in transformable electronics for their extraordinary mechanical compli-

ance [20,21]. Historically, microscopic metal "wires" are called "whiskers" for their resemblance to mammalian hair. Although the two words are in principle interchangeable, the term "nano-whiskers" shall be used hereinafter to refer to the metal nanowires synthesized in this work.

The extrusion of metal whiskers from the ores has been noticed for centuries, especially in the field of mining and metallurgy. The observation can be found in metallurgical books that date back to the 16$^{th}$ and 17$^{th}$ centuries, where it was recorded the filamentary growth of metals from ores [22,23]. A major discovery was made in the 16$^{th}$ century by Larzarus Ercker von Schreckenfels the Münzwardein, Münzmeister, and mining inspector when he noticed the sprout of Ag whiskers from the ingots during fire assay [24]. In the following centuries, many scientists observed and reported the filamentary growth of different metals. Johann Friedrich Henckel [25] found metal filaments in solutions in 1755. Formations of filaments of pure metals reduced from metal sulfides were widely reported [26–28]. But it was not until the 1950s that metal whiskers started to attract major research interest, due to their role in short-circuit failures widely encountered with electroplated devices. As a result, the growth condition and growth mechanism were intensively studied to prevent failures in electronics caused by whisker formation. Whiskers of Cd and Sn were the focus at the time as they were widely used in electronics as coating and welding materials. Regarding the synthesis, a sophisticated system for metal whiskers growth was developed by Brenner [29–31] in the 1950s. By carefully controlling the growth conditions (*i.e.* halide precursors, temperature), various metal whiskers including Cu, Ag, Fe, Ni, Co and Pt were successfully obtained from the reduction of their respective halides. The whiskers synthesized with this method are single crystals and exhibit different properties from their bulk counterparts thanks to their high aspect ratio, absence of defects and lack of grain boundaries.

## 1.2 Overview of the Thesis

This work aims to synthesize whisker structures of IB and VIII metals and their alloys and to understand the mechanism behind their spontaneous growth. The main characterization method is electron microscopy, which was applied for the study of the shape, crystal structure and chemical composition of the whiskers. Preliminary analyses on mechanical, magnetic properties as well as on phase transformation were also carried out in order to explore their potential applications.

The thesis is structured as follows: the 1$^{st}$ chapter gives a brief introduction to the history of whisker research as well as to the outstanding progress and findings achieved in the domain. The theoretical considerations necessary for the understanding of this work are also found in this chapter. The 2$^{nd}$ chapter deals with the basic principles of the

characterization techniques as well as the synthesis process used in this work. The experimental results are presented in chapter 3. The structure and morphology of the nanostructures (whiskers, platelets, *etc.*) were studied with Electron Microscopy techniques. Chapter 4 holds discussion on the effects of size, thickness, shape on the whisker properties, notably regarding the phase transformation in Co whiskers and the magnetic domain structures of Co, Ni, Fe whiskers. Finally in the 5$^{th}$ chapter, a conclusion is given on the growth conditions and growth mechanisms of the whisker structures, based on a comparison made between the experimental observations throughout this work and theoretical considerations. This is followed by a short summary of all the important findings presented in this work.

## 1.3 Nucleation and Growth Mechanism

### 1.3.1 Screw Dislocation Theory

Although the metal whiskering phenomenon has been studied for over five hundred years, the exact mechanism of the spontaneous growth is still under debate. Most of the contemporary interpretations of the nucleation and growth process of the whiskers are the result of the intensive investigations started 60 years ago. Among those, the most popular theory for whisker growth is the screw dislocation theory, initially proposed by Frank [32] in 1949 to explain the crystal growth on a substrate from the vapor phase. The nucleation takes place on the step of a screw dislocation at low supersaturation. Crystal growth then progresses by extending these dislocations. This theory was applied by Peach [33] to explain the growth of Sn whiskers. Sn atoms migrate through a screw dislocation along the whisker axis and subsequently incorporate themselves at the whisker tip. This theory was later challenged by Koonce and Arnold [34] when they observed additional material being inserted at the root site rather than at the tip of the Sn whiskers. Eshelby [35] later proposed a mechanism based on dislocation loops emitted from a Frank-Read source at the substrate surface. The whisker growth in this case was progressed by the expansion and glide of the dislocation loops. Around the same time, Frank [36] further developed his theory by considering a rotating edge dislocation that pins to a screw dislocation perpendicular to the surface as the origin of the whisker growth. Both authors came to the same conclusion that the surface tension developed by the oxidation of the whisker surface is the driving force for the whisker growth. Similarly, J. Franks [37,38] proposed that the whiskers grow by the gliding of dislocations from lattice faults under stress. Amelinckx [39] also suggested a theory which involves a helical dislocation climbing towards the surface.

By studying the whisker growth by vapor condensation around an axial screw dislocation inherited from the substrate, Sears [40–43] and Brenner [29,31,44] came to conclude that the dislocation at the whisker tip acted as an effective sink for all the atoms impinged on the whisker sidewall within a certain distance (diffusion length). They also found out about the important role that supersaturation plays in the whisker growth process. The whiskers would only grow if supersaturation is less than what is required for 2D nucleation. Brenner [30] further reported the observation of both tip growth (Cu, Fe) and root growth (Ag) for different materials. The Cu, Fe and Ag whiskers each exhibits several different orientations and cross-sectional shapes. Some Co whiskers were found to be partially hexagonal and partially cubic in structure. The author proclaimed that the cross-sectional shape of the whiskers undergoes considerable changes during growth. The initial near circular cross section was not preserved due to the faster radial growth of high index planes. The high index planes then completely disappeared in the end, leaving behind only the low index planes. Note that the radial growth is limited by the rate of nucleation of surface steps.

Another widely accepted theory is the stress induced growth mechanism, well known for explaining Sn and Cd whiskers extruded from welding and connecting parts. Originally suggested by Galt and Herring [45], the theory considers the driving force for the growth of Sn whiskers to be internal stresses (the pressure gradient between the interior and the surface). This theory was recently adopted by Mittemeijer's group [46,47] who explains the growth of Sn whiskers as due to local stress difference (stress induced whisker growth). Finally, Carol Handwerker [48–51] also attributed the growth of their Ag whiskers, obtained on trilayers, to thermal expansion misfit stress and the reduction in interfacial energy.

There are also some new theories being developed in recent years. Karpov [52,53] explained the whisker growth as a result of electrostatic polarization in the electric field induced by surface imperfections (contaminations, oxide states, grain boundaries). Amram *et al.* [54] considered the growth of Fe nanowires from thin films dewetting during annealing to be capillary-driven. The nanowire growth is fueled by the incorporation/diffusion of the Fe atoms at/to the nanowire-substrate interface (root site). Another special case of whisker growth involves a twin boundary passing through the whisker axis, known as twin plane re-entrant mechanism (TPRE) in the field of semiconductor nanowires [55]. Notably, Gamalski and coworkers [56] observed the VLS growth of Au catalyzed Ge nanowires as mediated by a twin-plane (with {111} interface). They proposed that the existence of the twin-plane lowers the nucleation barrier, thus acting as a preferential nucleation site for nanowire growth.

## 1.3.2 Nucleation in Thin Film Growth

Since the whiskers in this work are synthesized with physical vapor deposition (PVD), which is the same process for classic thin film growth, the general crystal growth mechanism (nucleation, diffusion) for thin films should be therefore also applicable in our case.

A typical crystal growth process on an infinitely large substrate is illustrated in Figure 1.1. The atoms from the vapor phase first arrive at the substrate surface where they are adsorbed by the van der Waals force. These atoms, called adatoms, can then either desorb back to their vapor phase or diffuse at the substrate surface until they form chemical bonds (chemisorption) with other adatoms, nuclei or with the substrate itself. Once the size of the nuclei exceeds the critical value, they can further grow into stable structures, such as thin film and islands, or in this work, whiskers and platelets.

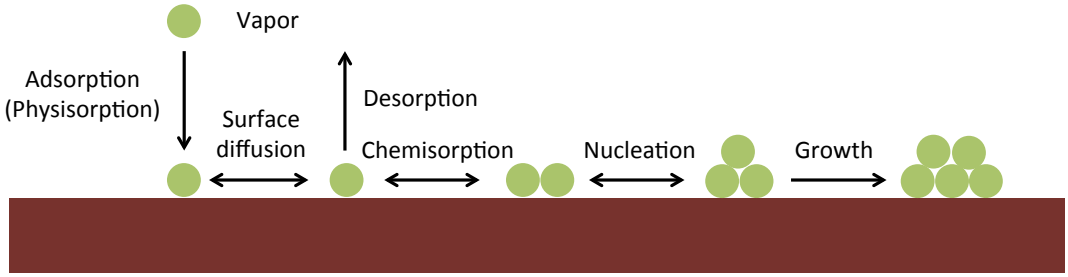


Figure 1.1 Schematic illustration of the thin film growth process with PVD.

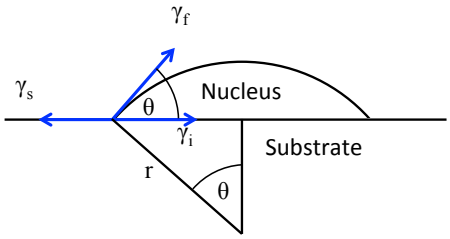


Figure 1.2 Schematic illustration of the capillary theory of nucleation.

Thermodynamically speaking, the formation of nuclei on the substrate surface changes the free energy by introducing new surfaces and new interfaces (Figure 1.2). The free energy change from the nucleation is expressed as

$$\Delta G = a_3 r^3 \Delta G_v + a_1 r^2 \gamma_{\mathrm{f}} + a_2 r^2 \gamma_{\mathrm{i}} - a_2 r^2 \gamma_{\mathrm{s}}. \qquad (1.1)$$

$\Delta G_v$ is the free-energy change per unit volume, which drives the nucleation reaction. $\gamma$ is the surface/interface energy (also called surface/interface tension) per unit area with the subscripts f, i and s denoting film, interface and substrate, respectively. $r$ is the mean radius of the nucleus. The geometric constants can be derived from the schematic in

Figure 1.2 as $a_1 = 2\pi(1-\cos\theta)$, $a_2 = \pi\sin^2\theta$ and $a_3 = \frac{\pi}{3}(2-3\cos\theta+\cos^3\theta)$. $\theta$ is called the contact angle or wetting angle, which quantifies the wetting status of the two contact phases. In mechanical equilibrium, the net force of the horizontal components should be zero

$$\gamma_s = \gamma_i + \gamma_f\cos\theta \quad \text{or} \quad \cos\theta = (\gamma_s - \gamma_i)/\gamma_f. \tag{1.2}$$

The thermodynamic equilibrium between the three phases is reached when $d\,\Delta G/dr = 0$, at which point the radius of the nucleus $r^*$ is

$$r^* = \frac{-2(a_1\gamma_f + a_2\gamma_i - a_2\gamma_s)}{3a_3\Delta G_v}. \tag{1.3}$$

$r^*$ is the critical size. Only nuclei with at least size $r^*$ can grow into stable structures. Smaller nuclei ($r < r^*$) are thermodynamically unstable and will shrink and disappear eventually. Further expansion of the critical nuclei is energetically favored as it lowers the total free energy change $\Delta G$. At $r = r^*$ we have

$$\Delta G^* = \frac{4(a_1\gamma_f + a_2\gamma_i - a_2\gamma_s)^3}{27a_3^2\Delta G_V^2} \tag{1.4}$$

$$= \frac{16\pi(\gamma_f)^3}{3(\Delta G_V)^2}\left(\frac{2-3\cos\theta+\cos^3\theta}{4}\right). \tag{1.5}$$

Equation (1.5) is obtained by substituting the geometric relation of interface tensions in equation (1.2), $\Delta G^*$ is defined as the activation barrier for nucleation. The thin film growth process can be discriminated into 3 different modes, depending on the surface and interface energies. When $\gamma_s \geq \gamma_i + \gamma_f$, the film wets the substrate ($\theta \cong 0$), layer by layer (Frank-Van Der Merwe) growth occurs. At $\theta = 0$, there is no barrier for 2D nucleation. When $\gamma_s < \gamma_i + \gamma_f$, $\theta > 0$, the surface tension of the film exceeds that of the substrate, island (Volmer-Weber) growth takes place. The extreme condition is achieved at $\theta = 180°$ where the dewetting of the nuclei on the substrate surface results in homogeneous nucleation. If $\theta$ changes during growth, layer plus island (Stranski-Krastanov) growth is observed.

The surface heterogeneities such as terrace, ledges, kinks, and impurities are energetically favored sites for adatoms to aggregate and form stable nuclei. This is because the binding energy of adatoms on these sites is greater than that on the planar surface due to the larger number of dangling bonds. For the same reason, nucleation occurs preferably on kinks than on ledges or terraces. This is known as the terrace-ledge-kink surface model (TLK) [57].

Kinetically speaking, upon arriving at the surface, the adatoms might not be desorbed immediately but would instead remain at the surface for a certain amount of time $\tau_s$,

$$\tau_s = \frac{1}{\nu}\exp\left(\frac{E_{des}}{k_B T}\right). \tag{1.6}$$

$\nu$ is the vibrational frequency of an adatom at the surface (typically of the order of $10^{-13}$ $s^{-1}$). $k_B$ is the Boltzmann constant. $E_{des}$ is the energy required for it to be desorbed back into vapor. Larger number of available atom bonds would lead to a higher $E_{des}$ value. During this time ($\tau_s$), the adatoms may diffuse freely at the surface, eventually rejoining other adatoms into forming stable nuclei, unlikely to return to the vapor phase. We can rewrite equation (1.6) to yield the desorption frequency

$$\omega = \nu\exp\left(-\frac{E_{des}}{k_B T}\right). \tag{1.7}$$

The nucleation rate $\dot{N}$ (in unit of nuclei/$cm^2$·s) is essentially proportional to the product of three terms, namely, $N^*$, the equilibrium number (per $cm^2$) of stable nuclei, $A^*$, the area of the critical nuclei ($cm^2$) and $\omega$, the rate of the impinging atoms ($cm^2$·s)

$$\dot{N} = N^* A^* \omega. \tag{1.8}$$

The equilibrium number of stable nuclei itself is

$$N^* = n_s \exp\left(-\frac{\Delta G^*}{k_B T}\right). \tag{1.9}$$

Here, $n_s$ is the total nucleation site density. It can be inferred from the above equations that the nucleation rate depends strongly on the activation barrier for nucleation $\Delta G^*$ and the temperature $T$.

The ability of the adatom to diffuse is measured by its diffusion length

$$\Gamma = a_0 \exp\left(\frac{E_{des} - E_s}{2k_B T}\right), \tag{1.10}$$

where $a_0$ is the neighboring lattice plane spacing, $E_s$ is the activation energy for surface diffusion, $E_{des} - E_s$ is the diffusion energy barrier. The diffusion length is also strongly temperature dependent.

Apart from being dependent on $\Delta G^*$ and $T$, the nucleation process is in addition affected by the deposition rate. The free-energy change in equation (1.1) of a condensation process writes

$$\Delta G_v = -\frac{k_B T}{\Omega} \ln\left(\frac{P_\mathrm{v}}{P_\mathrm{e}}\right) = -\frac{k_B T}{\Omega} \ln\left(\frac{\dot{R}}{\dot{R}_e}\right). \tag{1.11}$$

$\Omega$ is the atomic volume. $P_v$ is the pressure of the supersaturated vapor. $P_e$ is the equilibrium vapor pressure. $\dot{\mathrm{R}}$ and $\dot{\mathrm{R}}_\mathrm{e}$ are the deposition and the equilibrium re-evaporation rate, respectively. On an inert substrate, $\gamma_{\mathrm{fv}} = \gamma_{\mathrm{fs}}$, the differentiation of equation (1.3) becomes

$$\left(\frac{\partial r^*}{\partial T}\right)_{\dot{R}} = \frac{2}{3}\left[\frac{\gamma_\mathrm{f}(\partial \Delta G_\mathrm{V}/\partial T) - (a_1 + a_2)\Delta G_\mathrm{V} \partial\, \gamma_\mathrm{f}/\partial T}{a_3 (\Delta G_\mathrm{V})^2}\right]. \tag{1.12}$$

For $|\Delta G_\mathrm{V}| \ll 1.6\times10^{10}$ J/m$^3$, $\gamma_{\mathrm{fv}}\sim1$ J/m$^2$ and $\partial\, \gamma_{\mathrm{fv}}/\partial T \sim -0.05$ mJ/m$^2$·K. $\partial \Delta G_\mathrm{V}/\partial T$ is roughly $8\times10^6$ J/m$^3$·K for most metals, this yields

$$(\partial r^*/\partial T)_{\dot{R}} > 0, \tag{1.13}$$

$$(\Delta G^*/\partial T)_{\dot{R}} > 0, \tag{1.14}$$

$$\left(\partial r^*/\partial \dot{R}\right)_T < 0. \tag{1.15}$$

Direct chain-rule differentiation from equation (1.3) and (1.11) gives

$$\left(\frac{\partial r^*}{\partial \dot{R}}\right)_T = \left(\frac{\partial r^*}{\partial \Delta G_\mathrm{V}}\right)\left(\frac{\partial \Delta G_\mathrm{V}}{\partial \dot{R}}\right) = \left(-\frac{r^*}{\Delta G_\mathrm{V}}\right)\left(-\frac{k_B T}{\Omega \dot{R}}\right). \tag{1.16}$$

With a negative $\Delta G^*$, we obtain

$$\left(\partial \Delta G^*/\partial \dot{R}\right)_T < 0. \tag{1.17}$$

The effect of the temperature and of the deposition rate is thus the following: higher substrate temperature results in larger critical nucleus (1.13) and a higher energy barrier (1.14) for nucleation. The number of stable nuclei $N^*$ decreases exponentially with increasing $\Delta G^*$ and increasing $T$ (1.9). The direct implication is that higher temperature yields larger but fewer nuclei. Higher deposition rate, too, yields larger nuclei (1.15), but in this case the number of stable nuclei is also higher (1.17). In short, if the goal is to obtain single crystal structures with very large grains, the optimal growth parameter would be a high substrate temperature and a low deposition rate.

### 1.3.3 Kinetic Growth Model

The commonly accepted kinetic model for whisker growth, first proposed by Sears [44,58] and further developed by Ruth and Hirth [59], describes the growth of a

whisker as consisting of three stages, the adsorption of the impinging atoms from the supersaturated vapor phase, their diffusion along the whisker surface and their partial re-evaporation before reaching the whisker tip:

$$\frac{\partial C(x',t)}{\partial t} = D\frac{\partial^2 C(x',t)}{\partial \mathrm{x}'^2} - \omega C(\mathrm{x}',t) + J. \qquad (1.18)$$

Here, $C$ is the adatom concentration as a function of the distance $x'$ from the whisker base and of the time $t$. $D$ is the surface diffusion coefficient. $J$ is the impingement flux form the supersaturated vapor. The origin of the coordinate system $x' = 0$ is located at the tip of the whisker that moves as the whiskers grow. The choice was made as the tip was considered as a sink for the adatoms. This model unified the seemingly contradictive growth speed observed experimentally by different authors [58,60]. The linear growth law [61,62] can be obtained under the steady state condition if in addition the diffusion length of the adatoms on the whisker surface is shorter than the whisker length. If however, the diffusion length $\Gamma$ is longer than the whisker length (*i.e.* early stage of growth), the exponential growth law [60] is then derived. The above model also allowed Ruth and Hirth to calculate the conditions that reduce the exponential whisker growth to a linear one, either by re-evaporation of the adatoms or via rate controlled adatom exchange at the whisker tip. The linear growth law was derived respectively by Dittmar and Neumann [61] and by Blakely and Jackson [62]. These are further supported by experimental results listed in [61,63]. The linear growth could then be terminated by the annihilation of spiral dislocations [64–66] or by the poisoning of the whisker tip [63,67].

## 1.3.4 Our Previous Studies

The whisker growth obtained by our group cannot be simply explained by the screw dislocation theory as no screw dislocation has ever been detected along the whisker axis from our previous studies [68]. Instead, a defect-assisted theory was proposed which explains the metal whisker growth by PVD as due to the nucleation of diffused adatoms at defect sites. In our case, those defects were located in the mediating carbon film, and hence the incorporation sites for the adatoms were at the whisker root. This was further supported by a later work which relates the density of the whiskers obtained to the surface roughness of the deposited carbon layer [69]. More recently, we have deliberately introduced defects at the substrate surface by etching pits using Focused Ion Beam (FIB). The result showed that indeed more whiskers were observed near the pits than elsewhere [70]. Limited by the resolution, the smallest pit size that can be achieved was about several tenth of nanometers, which is much larger than the area of the whisker root. As a result, there are often more than one nanostructure (whisker, platelet or nanoparticle) found at each pit site.

The diffusion behavior of the metal adatoms on the mediating carbon film also affects the whisker growth. Mortimer and Nicholas [71,72] studied the wetting behavior of Cu and Cu alloys on carbon and carbides surfaces. They found that the wetting behavior of pure Cu on carbon surface is promoted by the formation of carbide layers from alloy additions, since the interfacial energy is much lower than the surface energy of carbon. According to the observation of Arthur and Cho [73], except at surface defect sites such as ledges, the two-dimensional nuclei of Au and Ag on graphite surface are in general unstable due to the weak bonding, especially at elevated temperature when the desorption rate is higher. The work of Lewis and Jordan [74] further showed that the surface vacancies produced by electron bombardment can serve as the preferred sites for nucleation, which in turn increased the nuclei density as well as the possibility of intercalating adatoms to form epitaxial relation with the substrate. Finally, Egelhoff and Tibbetts [75] reported that the nucleation is far more effective on amorphous carbon surface saturated with defects from ion bombardment than on graphite surface.

## 1.4 Size Related Properties of Whiskers

It has long been speculated that the size and the shape of the whiskers may have an impact on their growth process. Mohaddes [76] investigated the size and shape evolution of single crystal α-Fe nanowires synthesized from pulsed-laser deposition. The cross-sectional shape of the nanowires changes from circular to octahedral and then to square as the growth temperature increases from 560 to 840 °C. The same shape evolution would have been observed by increasing the nanowire diameter from 4 to 50 nm as predicted by their simulations. With that, they have come to the conclusion that the shape change is related to elastic energy effects and that the nanowire growth is kinetically driven by diffusion. Hayashi and coworkers [77] studied the formation of nanoparticles of various BCC and FCC metals from gas evaporation. They found out that the nanoparticles of FCC metals are more likely to contain twins. They also reported a strong dependence of the shape and the crystal habit (orientation) of the metal nanoparticles on the growth conditions (temperature, pressure).

In the last paragraph, we have briefly mentioned the possible effect of whisker size on their cross-sectional shape, but the more general use of the term “size effect” refers to the changes in material properties (mechanical [68,78], electrical [79,80], optical [81,82], magnetic [83–86] or reactivity [87,88]) when at least one of the dimensions is reduced to the nanometer range. Size effects are usually explained by a more prominent surface/interface effect as the result of an increase in the specific surface area and/or in the aspect ratio [18]. The decrease in the number of imperfections in smaller structures may also play an important role [89]. In the case of whiskers, because of their

perfect single crystal structure and their highly anisotropic shape, remarkable size effects are often observed [68,80,81,84].

### 1.4.1 Mechanical Properties

Size effect is nothing new to the mechanical engineering community. The idea of "smaller is stronger" has been the driving force of intensive researches for centuries. Mechanical size effects have been confirmed on different classes of nanomaterials (thin films [90,91], nanopillars [78,92,93] and nanowires [68,94,95]) by means of versatile testing methods such as indentation, compression, tensile tests and fatigue tests.

It has long been proven by Herring and Galt [45] that the elastic and plastic behaviors under bending of the Sn whiskers extruded from Sn-plated layer are close to those of a perfect crystal. They credited the extraordinary strength (the large range of elastic deformation) to the absence of dislocations within the crystal structure. A few years later, Brenner [31] measured the strength of various metal whiskers produced by different methods. Some of the whiskers he measured were found to be much stronger than their bulk counterparts, reaching even the predicted theoretical values. Although no quantitative conclusion was made, the observed increase in mechanical strength was credited to the smaller size, surface perfection and structural perfection of the metal whiskers. We have previously performed bending tests [96] and tensile test [68] on the PVD Cu whiskers prepared in our laboratory. The mechanical response of the Cu whiskers under both tests was within range of their theoretical value. Ideal strength was also recorded during tensile tests on Au nanowhiskers [97]. Moreover, twinning mode of plastic deformation was found on these pristine dislocation free whiskers.

### 1.4.2 Phase Transformation

Because of the constraints imposed by the surface, the interface and grain boundaries, size effects are expected in phase transformations. Martensitic transformation is a first order diffusion-less solid phase transformation. The process is reversible with hysteresis, leading to a shape-memory effect. The reversible transformation strains can be manipulated with temperature and by applying external stress or magnetic fields. As a result, martensitic materials are widely adopted in medical devices [98], implantations [99], damping devices [100], sensors and actuators [101].

Co is one of the materials capable of undergoing martensitic transformation. When cooling down from high temperatures, bulk Co transforms from hexagonal close-packed (HCP) structure to face-centered cubic (FCC) structure. This phase transformation process has been actively studied over the past few decades. It is now understood that

the phase transformation of Co is accomplished by the motion of type $\frac{1}{6}<112>_{FCC}$ (martensitic transformation) and $\frac{1}{3}<1\bar{1}00>_{HCP}$ (reverse transformation) Shockley partial dislocations, which glide on every other $\{111\}_{FCC}/\{0001\}_{HCP}$ plane (the habit plane). The energy of a perfect dislocation is reduced by its dissociation into two Shockley partial dislocations, and the stacking fault energy in both allotropes is relatively trivial [102]. The minimum free energy of the system is achieved with a mixture of the two crystal structures (HCP and FCC). The hysteresis is present in both the cooling and the heating process, and is understood as the difference in free-energy to start the dislocation motion [103]. During the phase transformation, twin structures and stacking faults are frequently formed. They can be used to mark the region of the transformation [103,104]. The stacking faults can also be viewed as the transitional area between the HCP and the FCC phase. For instance, the stacking fault in the AB<u>A-BC</u>BCBC sequence can be seen as the beginning of a FCC phase (underlined part) in a HCP to FCC transformation. Similarly, the twin in the ABC<u>ABA</u>CBA sequence can be seen as the beginning of a HCP phase (underlined part) in a FCC to HCP transformation. Christian [103] discussed the mechanism of the martensitic transformation in Co crystals with a dislocation theory. A pair of partial dislocations in the FCC part produces a HCP segment of about 2 atomic layers thick. This latter is then used to seed the transformation. The formations of stacking faults in the HCP phase and twin structures in the FCC phase are attributed to the motion of partial dislocations during phase transformations.

The transformation process is strongly affected by the shape and the size of the crystals (grains). Edwards and Lipson [105] found coexistence of HCP and FCC structures in powder Co samples but only HCP structures in coarse grained samples. The HCP structure in Co crystals was found to contain stacking faults, which is explained as due to a lowered free energy. Owen [106] examined the crystal structures of Co with different grain size and at different temperature. He concluded that smaller the grain size, more stable the FCC phase is at room temperature. Meanwhile, Fisher [107] reported that the FCC structure is stable for Co thin films of up to 100 nm thick at temperature between 150 and 870 K. Hesemann [108,109] found that the martensitic transformation of Co thin films is constrained by the orientation of the thin film with regard to the substrate. The transformation is in addition impeded by the tensile stress in the thin films. Luborsky [110] synthesized Fe and Co whiskers of 10 microns diameter on Mo substrates via vapor deposition. Among the numerous HCP Co whiskers, one FCC whisker was found. The anomaly was explained by an inhibited FCC to HCP transformation due to the small size and/or high degree of perfection of the whisker. Bauer [111] investigated the kinetic process of the transformation upon thermal cycling to reach a fully reversible allotropic phase transformation. He concluded that the transformation proceeds by

dislocation glide. Sato [112] reported that the FCC-HCP transformation of Co nanoparticles can be influenced by the particle size and defects (dislocations and stacking faults). This is supported by the findings of Kitakami [113] that, growth of the FCC phase is favored for smaller particles. The preferential growth was explained by the slightly smaller surface free energy of the FCC phase.

The martensitic transformation is also affected by deformation. Zhang [114] performed high-resolution TEM analysis on the mechanism of deformation induced martensitic transformation in high manganese TRIP steel. They observed nanotwins formation during FCC austenite to HCP ε-martensite transformation and the nucleation of secondary ε-martensite phase at stacking faults near the deformation twins.

## 1.4.3 Magnetic Properties

Thanks to the absence of structural defects and chemical impurities, the single crystal whiskers with perfect facets are ideal for the investigations of the magnetic properties of transition metals (Fe, Ni and Co), as they allows the theoretical limits of the material to be reached. Research interest on the magnetic properties of the transition metal whiskers was stimulated by their potential applications. The large aspect ratio (shape anisotropy) makes the whiskers potentially interesting for making ultra-high-density magnetic recording system [115]; They are also expected to be used to induce hyperthermia with minimal damage to untargeted cells during cancer treatment [116]; Magnetic nanowire–enhanced opto-magnetic tweezers have already shown promising results with high spatial resolution and full 3D manipulation [117]; Electro-drive actuators made of metal nanowires are both lightweight and easy to fabricate [118]. Most importantly, it is possible to tailor the properties of nanowhiskers by combining different materials into one single structure. For instance, the multilayer nanowire with alternating periodic magnetic and nonmagnetic parts was reported to possess at the same time excellent electrical and excellent magnetic properties [119–122].

### 1.4.3.1 Magnetic Energies

The total free energy of a ferromagnet is given by

$$G(\mathbf{M};\mathbf{H}_a) = \int_V (e_{ex} + e_{an} + e_H + e_{ms} + e^0)dV. \qquad (1.19)$$

$e_{ex}$ is the exchange energy density. $e_{an}$ is the anisotropy energy density. $e_H$ is the external field energy density. $e_{ms}$ is the stray field (magnetostatic) energy density. $e^0$ is the magnetostrictive energy density. The exchange energy arises from the interactions between neighboring atoms with angle $\phi$

$$E_{ex} = -2JS^2 \cos\phi_{ij}. \tag{1.20}$$

The continuum expression writes

$$E_{ex} = -A\cos\left(\frac{d\phi}{dx}\right). \tag{1.21}$$

Where $A = 2nJS^2/a$ is a material constant, called the exchange stiffness constant (erg/cm), $n$ is the number of atoms per unit cell, and $a$ is the lattice parameter. $J$ is the exchange energy integral and $S$ is the spin. The quantity $d\phi/dx$ represents the rate at which the direction of local magnetization rotates. With Taylor expansion, the above equation can be further reduced to

$$E_{ex} = -2A + A\left(\frac{d\phi}{dx}\right)^2. \tag{1.22}$$

The exchange energy alone does not show any anisotropic behavior, regardless of the actual geometrical anisotropy of the crystal structure. However, the magnetic property of a material can indeed be directional dependent, the associated energy is the anisotropy energy $e_{an}$. Its most common form is the magnetocrystalline anisotropy energy $e_{mc}$. The magnetocrystalline anisotropy energy describes the dependence of the energy of a ferromagnet on the magnetization direction relative to its crystal axes. It results in a magnetic easy axis and a hard axis in crystals. For a cubic material, we have

$$e_{mc} = K_0 + K_1(\alpha_1^2\alpha_2^2 + \alpha_2^2\alpha_3^2 + \alpha_3^2\alpha_1^2) + K_2(\alpha_1^2\alpha_2^2\alpha_3^2) + \cdots. \tag{1.23}$$

$\alpha_1, \alpha_2, \alpha_3$ are the cosines of the angles between the magnetization $M_s$ and the crystal axes $a, b, c$. The anisotropy constants (in erg/cm$^3$) $K_0, K_1, K_2$ are material and temperature specific. Table 1.1 gives some typical values of $e_{mc}$ for low index $M_s$ directions.

Table 1.1 Magnetocrystalline anisotropy energy density in a cubic crystal.

| $M_s$ | $a$ | $b$ | $c$ | $\alpha_1$ | $\alpha_2$ | $\alpha_3$ | $e_{mc}$ |
|---|---|---|---|---|---|---|---|
| [100] | 0 | 90° | 90° | 1 | 0 | 0 | $K_0$ |
| [110] | 45° | 45° | 90° | $\frac{1}{\sqrt{2}}$ | $\frac{1}{\sqrt{2}}$ | 0 | $K_0 + \frac{K_1}{4}$ |
| [111] | 54.7° | 54.7° | 54.7° | $\frac{1}{\sqrt{3}}$ | $\frac{1}{\sqrt{3}}$ | $\frac{1}{\sqrt{3}}$ | $K_0 + \frac{K_1}{3} + \frac{K_2}{27}$ |

When $K_2$ in equation (1.23) is negligible, the direction of easy magnetization is entirely determined by the sign of $K_1$. For a positive $K_1$, $e_{mc<100>} < e_{mc<110>} < e_{mc<111>}$, <100> are the easy directions. For a negative $K_1$, $e_{mc<100>} > e_{mc<110>} > e_{mc<111>}$,

and <111> become the easy directions. The easy axes for BCC Fe (positive $K_1$) are <100> [123], while the easy axes for FCC Ni and FCC Co (negative $K_1$) are <111> [124–126]. As for a HCP crystal, we have

$$e_{mc} = K_0 + K_1 \sin^2\theta + K_2 \sin^4\theta + \cdots. \tag{1.24}$$

The anisotropy energy depends only on the angle $\theta$ between $M_s$ and the hexagonal $c$ axis. When $K_0$ and $K_1$ are both positive (*e.g.* HCP Co), the magnetocrystalline energy is minimum only at $\theta = 0$. The easy axis is thus along the c-axis, *i.e.* the <0001> direction [124]. The anisotropy is described as uniaxial as all the other directions in the basal plane are equally hard.

When applying an external magnetic field, the interaction energy of the magnetization vector field $m$ with the external field $H_{ex}$ gives the external field (Zeeman) energy ($M_s$ is the saturation magnetization):

$$E_H = -M_s \int H_{ex} m dV. \tag{1.25}$$

The magnetic field energy also accounts for the magnetic field generated by the magnetic body itself. The latter is known as stray field energy or demagnetization energy, or magnetostatic energy $E_{ms}$

$$E_{ms} = \frac{1}{8\pi}\int H_d^2 dV = \frac{1}{2} N_d M^2 V. \tag{1.26}$$

$H_d$ is the demagnetization field. $N_d$ is the demagnetizing coefficient. If the specimen is non-spherical, the demagnetizing field is stronger along a short axis than along a long axis. In other words, it is easier to be magnetized along the long axes than along the short axes. As a result, the shape of the object by itself is a source of magnetic anisotropy. This is known as shape anisotropy. In the case of a prolate spheroid (rod), the demagnetizing coefficient along the long axis $c$ and the short axis $a$ are $N_c$ and $N_a$, respectively. $\theta$ is the angle of magnetization $M$ with regard to the $c$ axis. The magnetostatic energy density after taking into account shape anisotropy is

$$e_{ms} = \frac{1}{2} N_c M^2 + \frac{1}{2}(N_a - N_c) M^2 \sin^2\theta, \tag{1.27}$$

where the shape anisotropy constant is defined as

$$K_s = \frac{1}{2}(N_a - N_c) M^2. \tag{1.28}$$

For a prolate spheroid of polycrystalline cobalt with no preferred orientation ($M_s =$ 1422 emu/cm$^3$) and an axial ratio of 3.5, $K_s$ is about 4.5×10$^6$ erg/cm$^3$ [127], which equals the first crystal anisotropy constant $K_1$ of HCP cobalt. In other word, the shape anisotropy is comparable to the crystal anisotropy for a prolate spheroid of saturated cobalt with an axial ratio of 3.5. In this intermediate region, when the long axis of the prolate spheroid is not aligned with the easy axis dictated by magnetocrystalline anisotropy, the easiest magnetization is found in the direction that causes minimum anisotropy energy. For a much larger aspect ratio, the shape anisotropy becomes predominant, the easiest magnetization direction is then no longer dependent on the crystal orientation of the material.

Magnetostriction refers to the changes in shape or dimensions of ferro-magnetic materials during magnetization. The effect is mainly caused by spin-orbit coupling. The direct magnetostrictive effect itself is usually small, but it may indirectly (and strongly) affect the other free energy components. The most significant impact is on magnetocrystalline anisotropy. The result is known as anisotropic magnetostriction. Because both magnetostriction and crystal anisotropy are originated from spin-orbit coupling, a strong correlation is not unexpected. In fact, a large value of the anisotropy constant is usually accompanied by a large value of magnetostriction. For a cubic crystal subjected to a magnetic field for instance, spontaneous deformation of the lattice occurs to reduce the anisotropy energy, at the cost of increasing the elastic energy. The total energy (density) of magneto-elastic interaction for cubic crystals under tension writes

$$e^0 = \frac{3}{2} C_2 \lambda_{100}^2 - \frac{9}{2}(C_3 \lambda_{111}^2 - C_2 \lambda_{100}^2) \sum_{i \neq k} m_i^2 \, m_k^2, \tag{1.29}$$

$m_{i,k} = (m_1, m_2, m_3)$ is the direction vector of the magnetization.

The spontaneous magnetostrictive elongation is

$$\frac{\delta l}{l} = \frac{3}{2} \lambda_{100} \left( \sum_{i=1}^{3} \alpha_i^2 m_i^2 - \frac{1}{3} \right) + 3 \lambda_{111} \sum_{i>k} m_i m_k \, \alpha_i \alpha_k. \tag{1.30}$$

$C_2 = \frac{1}{2}(c_{11} - c_{12})$, $C_3 = c_{44}$ are the two shear moduli of the cubic crystal in Voigt's notation. $\alpha = (\alpha_1, \alpha_2, \alpha_3)$ is the unit vector along the direction of $\delta l$. $\lambda_{100}$, $\lambda_{111}$ are the saturation magnetostrictions in the their respective directions. The magneto-elastic energy is by definition zero for an unstrained lattice [128].

The resulted strain depends on the shape of the specimen, and is therefore referred to as the form effect. This effect occurs solely for the purpose of minimizing the magnetostatic energy as a longer specimen has a smaller $N_d$. The form effect is of the system. To be more specific, the magnetostatic energy (1.26) is reduced when the specimen is elon-

gated in the direction of $M_s$, generally small, negligible in the case of whiskers with high aspect ratio, but may not be neglected for shorter structures. The application of external stress can cause domain wall motion hence creating an easy axis of magnetization. However, in the absence of external stress, the spontaneous magnetostriction effect is often ignored.

### 1.4.3.2 Domain Formation

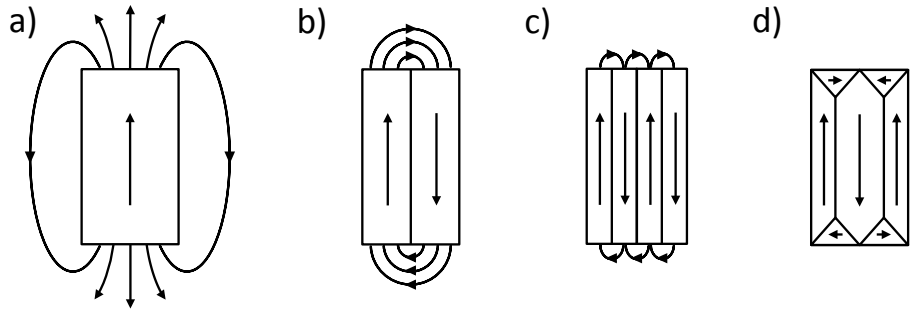


Figure 1.3 Different domain structures: (a) single domain; (b) two domains; (c) four domains; (d) closure multi-domain structure.

According to Landau and Lifshitz [129], domains are preferentially formed to minimize the total free energy, especially the stray field energy. As shown in Figure 1.3-a, the single domain structure causes magnetic "poles" on the crystal surface, resulting in a large value of the demagnetization energy. $N_d = 1/3$ for a cubic crystal along one of its edges, $L$ is the thickness of the crystal. The magnetostatic energy of the single-domain cubic crystal per unit area of its top surface is thus

$$e_{ms} = \frac{1}{6} {M_s}^2 L. \tag{1.31}$$

The demagnetization energy is reduced by a factor of ~2 by simply dividing the crystal into two domains with opposite magnetization direction (Figure 1.3-b). The magnetostatic energy of a multi-domain crystal (Figure 1.3-c) per unit area of its top surface is

$$e_{ms} = 0.85 {M_s}^2 D. \tag{1.32}$$

$D$ is the thickness of the slab-like domains [128]. The demagnetization energy is further reduced to zero for closure domain structures (Figure 1.3-d). The magnetic poles are removed with the introduction of the triangular prism domains at the boundaries near the crystal surfaces.

It costs extra energy to form the domain walls, which are the transition area between adjacent domains with different magnetization orientations. The cost of exchange energy is the lowest when the adjacent spins are parallel and the highest when they are antiparallel. The large exchange energy can be reduced if the 180° change in spin direc-

tion takes place over $N$ atomic planes, in which case the angle between adjacent spins is about $\pi/N$. However, the crystal anisotropy energy is also increased in this way as the spins are pointing away from the easy direction. The thickness of the domain wall is therefore the result of the competition between the exchange energy and the crystal anisotropy energy. In the case of a cubic crystal with $K_1 > 0$ and domain walls in the {100} plane, the energy per unit area of a 90° domain wall is approximately

$$\sigma_w^{90} = \sqrt{AK_1}. \tag{1.33}$$

$A$ is the exchange stiffness constant. The energy per unit area of a 180° domain wall is twice that value with

$$\sigma_w^{180} = 2\sqrt{AK_1}. \tag{1.34}$$

The thickness of domain walls is approximately

$$D_w = \pi\sqrt{A/K_1}. \tag{1.35}$$

In reality, the value of the domain wall thickness is usually much larger under the effects of the magnetoelastic energy [130].

The gradually change of magnetization can be realized either out of or in the plane of the domain wall. This is known as a Bloch wall (Figure 1.4-a) or a Néel wall (Figure 1.4-b), respectively. The Néel walls are usually found in thin films, as the in plane rotation of magnetization gives overall a lower energy for sample thickness comparable to the thickness of the domain wall. In a small disc-like (*i.e.* thickness much smaller than width) ferromagnetic sample, all spins tend to align in plane forming the so-called vortex structure (Figure 1.4-c). At the very core of the vortex structure, the magnetization is parallel to the normal of the disk plane. The vortex structure has the advantage of low exchange energy and zero stray field energy [131]. It has been observed experimentally by Shinjo [132] in the circular dots of Permalloy ($Ni_{80}Fe_{20}$) using magnetic force microscopy (MFM).

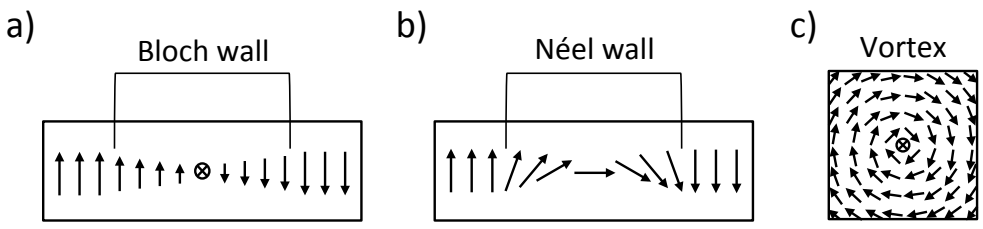


Figure 1.4 Schematic illustrations of (a) Bloch wall; (b) Néel wall; (c) magnetic vortex structures.

### 1.4.3.3 Size and Shape Effects

We have previously mentioned that the out of plane magnetization rotation in the Bloch wall structure is not energetically favorable for thin film samples. This is just one of the examples showing the domain wall structure being strongly affected by the dimensionality of the samples. In very small ferromagnetic particles, single domain nano-magnets can be found as a result of the suppressed domain wall formation [133]. This is because the surface energy terms (*e.g.* domain wall energy) in the total free energy become more prominent when the dimensions of the sample are reduced compared to the volume energy terms (*e.g.* demagnetization energy). Below a certain point (the critical size), it is no longer energetically favorable to form the domain walls, the sample is thus left with one single magnetized domain. Another way to understand this is by considering an object with its size smaller than the thickness of the domain walls. This object can only consist of one single magnetized domain.

Recall that the domains are formed mainly to reduce the magnetostatic (demagnetization) energy of the system. For a saturated single domain in a small spherical ferromagnetic particle of radius $r$, we obtain

$$E_{ms} = \frac{1}{2} N_d M^2 V = \frac{1}{2}\left(\frac{4}{3}\pi\right)^2 r^3 M^2. \tag{1.36}$$

The magnetostatic energy decreases dramatically with the size of the particle. In the case of Fe, the magnetostatic energy is approximately $24\times10^6$ ergs for $r = 1$ cm and $24\times10^{-12}$ ergs for $r = 10$ nm [128]. For a very small $r$, the energy cost for forming the domain walls would eventually overweigh the (magnetostatic) energy saved from it.

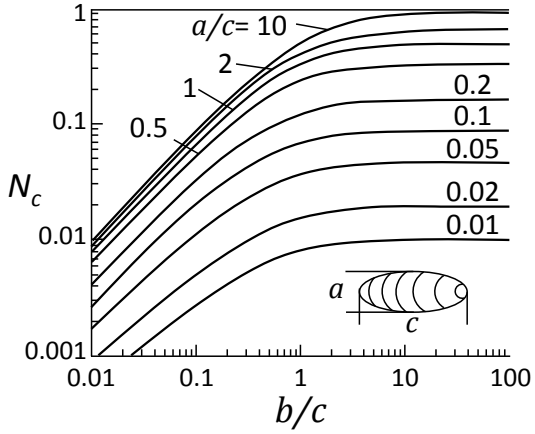


Figure 1.5 Demagnetizing factor $N_c$ of a prolated ellipsoid as a function of shape [134].

The critical size for forming single domain also depends on the shape of the object. A general rule is that the size of the thermodynamically stable single-domain particle is larger if they are elongated. Figure 1.5 shows the calculated demagnetizing

coefficient [134] along the long axis of ellipsoidal objects. For very long objects ($a/c < 0.01$), the demagnetizing factor is close to 0. The demagnetization (magnetostatic) energy is also close to 0 if the magnetization is along the long axis, *i.e.,* $\theta = 0°$ in equation (1.27). Once again, the energy cost for forming the domain walls would eventually overweigh the (demagnetization) energy saved from it, at which point the single domain state will be preferred. It is worth mentioning that the anisotropy constants are also strongly affected by the size and the shape of the specimen [135].

In the case of whiskers, we shall assume the magnetocrystalline easy axis (the combined result of magnetocrystalline anisotropy and shape anisotropy) to be either perpendicular or parallel to the whisker axis. This reduces the possible domain configurations to only three (Figure 1.6), based on Kittel's [136] models. For the sake of simplicity, the magnetostriction effects are neglected. The cross section of the whiskers is further assumed to be square shape with width *W*.

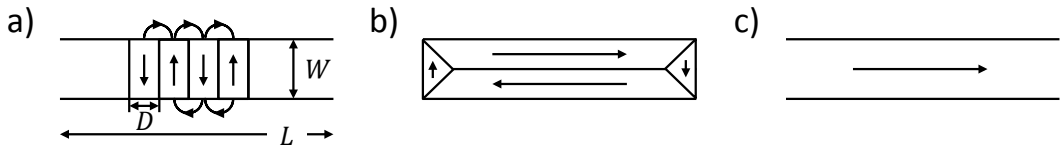


Figure 1.6 Possible domain configurations in a whisker.

Figure 1.6-a shows the case where the magnetocrystalline easy axis is perpendicular to the whisker axis and when the magnetocrystalline anisotropy predominates over the shape anisotropy. In this case, a multi-domain structure with domain thickness *D* is formed. According to equation (1.32), the magnetostatic energy per unit area is

$$e_{ms} = 2{\times}0.85{M_s}^2 D = 1.7{M_s}^2 D. \tag{1.37}$$

The factor of 2 arises from the fact that the whisker has two surfaces. The domain wall energy per unit area is

$$e_w = \frac{\sigma_w W}{D}. \tag{1.38}$$

The total energy per unit area is minimal when

$$D = \sqrt{\frac{\sigma_w W}{1.7{M_s}^2}}. \tag{1.39}$$

At which point the (minimum) energy per unit surface area becomes

$$e_{min} = 2\sqrt{1.7\sigma_w W} \cdot M_s. \tag{1.40}$$

The corresponding minimum energy per volume is

$$e_{min} = \frac{2\sqrt{1.7\sigma_w W} \cdot M_s \times 2LW}{LW^2} = 4\sqrt{\frac{1.7\sigma_w}{W}} \cdot M_s. \quad (1.41)$$

For the configuration shown in Figure 1.6-b, the whisker is composed of two elongated domains with the flux circuit being closed internally by triangular caps. The magnetostatic energy in this case is zero. Only the domain wall energy needs to be taken into account. Considering only the larger contribution from the domain walls parallel to the whisker axis, the domain wall energy per volume is

$$e_w = \frac{\sigma_w WL}{V} = \frac{\sigma_w}{W}. \quad (1.42)$$

Finally, for the configuration shown in Figure 1.6-c, the whisker consists of only one domain magnetized along the whisker axis. Only the magnetostatic energy needs to be considered. Its volume density is

$$e_{ms} = \frac{1}{2} N_d M^2. \quad (1.43)$$

The value of the demagnetizing factor can be equal to that previously obtained for a prolate spheroid with the same aspect ratio (Figure 1.5).

Observations and analysis on the magnetic domain structures of micro- and nano-sized objects have been carried on for decades. In the 1950s, De Blois observed the multi-domain structures in micro-sized Fe whiskers [137,138] and Ni platelets [139] obtained with traditional Bitter method. The domains were magnetized along the direction of the magnetocrystalline easy axes. The coercive force was found be to close to the theoretic value. The coercivity increases with decreasing whisker diameter. The whiskers even exhibit a single domain structure when the diameter is small enough. Khan and coworkers [140] prepared single crystal Ni nanowires (with <100> and <111> as the axial directions) via electrochemical deposition. They reported a strong anisotropy in these nanowires along the whisker axis regardless of the crystallographic orientation. The Co and Fe nanowire arrays that they prepared showed the same behavior, indicating that the shape anisotropy of the nanowires and the dipolar interactions between them predominates over the magnetic contributions (*e.g.* magnetocrystalline anisotropy). Mohaddes [141] obtained similar results on single crystal α-Fe nanowire arrays (diameter 20 nm and length 200 nm) via decomposition. Their nanowires showed a strong magnetic anisotropy with the easy axis aligned with the axial direction of the nanowires. Bizirere [142] studied the magnetic structure of Ni nanowires with electron holography techniques. They observed a size dependence of the magnetic domain wall structure on the nanowire diameter. Novel magnetic nanostructures were also studied. Akhtari-Zavareh [122] prepared multilayer nanowires containing alternating and periodic ferro-

magnetic CoFeB and nonmagnetic Cu parts by template-assisted electro-deposition. Their electron holography investigations revealed that the magnetic properties of the multilayer nanowires depend on the thickness of the layers. The magnetization direction in the nanowires was predominantly parallel to the longer dimension of the magnetic parts, but shifted towards the direction of the external field (perpendicular to the wire axis) when the thickness of the magnetic layers is smaller than their diameter.

Size effects have long been observed on magnetic thin films. Kittel [136] suggested that in-plane magnetization is more energetically favored when the thickness of the thin film is much smaller than its transverse dimensions. Hillebrands [143] attributed their observed influence of film thickness on the magnetocrystalline anisotropy to the lattice distortion in the epitaxial FCC Co film. Ohtake [144] synthesized HCP and FCC thin films of single crystal Co on different substrate surfaces. They reported to have observed easy magnetization axes only in the thin film plane and along the HCP <0001> or the FCC <111> directions respectively for the two types of samples. The easy axes they observed were the same as those dictated by magnetocrystalline anisotropy in the corresponding bulk materials.

In the case of (thin) oblate samples, a critical thickness exists below which the formation of single domain state is favored over that of the vortex state. The critical thickness has been theoretically predicted by Hoffman [131] and experimentally observed by Cowburn [145] on samples of the same diameter but different thicknesses. With electron holography, Tonomura [146] studied the vortex structure in a 55 nm thick submicron triangular FCC Co platelet. The magnetic field was closed inside the particle while the magnetization was found to be circular in the central part of the particle. Another type of samples that has been intensively studied is the submicron ferromagnetic discs (nano-magnets) prepared by electron beam lithography. The review by Cowburn [147] shows that the size, shape and symmetry all play a crucial role on determining the magnetization state (or stabilizing the single domain state) of the nano-magnets. Miyata [148] demonstrated that circular, triangular, square and pentagonal nano-magnets all exhibit a single vortex structure. The chirality of the vortex structure can be further manipulated by an in-plane magnetic field. The resonant frequency of the vortex core was larger in the triangular sample than in the circular one as the result of a larger magnetostatic energy originated from the demagnetizing field of the side edges.

### 1.4.4 Others

There exist other size dependent properties in addition to those mentioned above. For instance, it has been reported that the electrical resistivity of Ag and Cu nanowires increases with decreasing wire diameter (from 200 to 15 nm), as a result of an increase

in the surface scattering of conduction electrons [149]. The thermal conductivity of Al nanowires, Pt nano-ribbons and Cu thin films were also found to decrease for smaller cross-sectional area, due to increased scattering of phonons at surfaces and by grain boundaries [150].

# 2 Experimental Methods

This chapter deals with the experimental methods employed in this work, which includes the synthesis of the whiskers (Paragraph 2.1.1) and the various electron microscopy methods (Paragraph 2.2-2.4) for their characterization. A detailed account for the preparation of all the samples concerned in this manuscript is given in Paragraph 2.1.2.

## 2.1 PVD and Whisker Growth

### 2.1.1 Experimental Setup

The thin film growth process can be roughly divided into three steps: (i) the production of the "building blocks" in the form of atoms, molecules or ions, (ii) the transportation of the "building blocks" onto a certain substrate and (iii) the condensation of these "building blocks" at the substrate surface. Depending on the mechanism, the growth process can be classified as either Physical Vapor Deposition (PVD) or Chemical Vapor Deposition (CVD), the main criteria being whether or not chemical reactions take place during step (i) and (iii). Moreover, a CVD process uses mostly reactive gaseous precursors while a PVD process relies on solid or molten sources.

The primary methods to generate source atoms in a PVD process are evaporation and sputtering [151]. The former transfers atoms by heating up the source to achieve effective evaporation or sublimation (*e.g.* Molecular Beam Epitaxy or MBE), while the latter removes atoms from the source target by means of ion bombardment and collisional momentum transfer (*e.g.* Magnetron Sputtering).

All the whisker specimens in this work were prepared by PVD. In some cases, a mediating layer (C or TiC) was deposited on the substrate surface (by sputtering) prior to the whisker growth. The whisker growth process was carried out in an Ultra High Vacuum (UHV)-MBE system (base pressure ~ $10^{-10}$ mbar). Its schematic is shown in Figure 2.1. The evaporation sources (effusion cells and electron beam evaporators) are located at the bottom of the UHV chamber. In an effusion cell, materials, in their ultrapure form, are subjected to radiant heating until they slowly begin to evaporate. The vapor of the (source) material is then redirected to the (target) substrate via a small opening at one end of the evaporator. The deposition rate (as a function of the source temperature or heater power) is pre-calibrated with a quartz balance. For some materials, a much higher temperature may be required to obtain a reasonable deposition rate. This is achieved with the electron beam evaporators. An electron gun generates a beam of high kinetic energy electrons (several keV), which is then deflected towards the source material by a

set of electromagnets. A MBE system is usually equipped with real-time structural and chemical characterization capabilities. In our case, the surface quality (surface reconstruction) and thin film growth (intensity oscillations) can be monitored using reflection high-energy electron diffraction (RHEED).

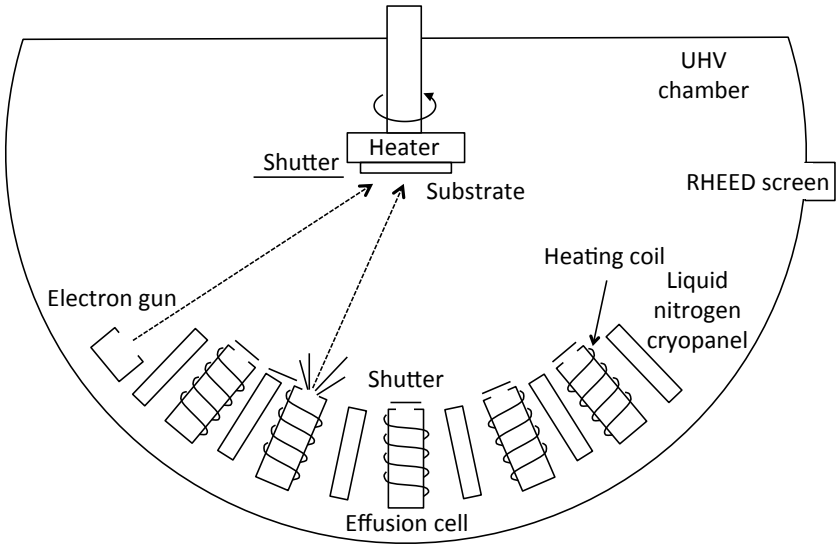


Figure 2.1 Schematics of the UHV-MBE system.

## 2.1.2 Sample Preparations

The process to be described below was first developed in the thin film laboratory of Max-Planck-Institute of Intelligent Systems (formerly MPI for Metals Research) in 2006 [68] and has since been used for the successful synthesis of metallic whiskers for almost a decade. One of the main interests of this approach is the simple sample preparation. The substrates were first cleaned in ultrasonic bath of acetone and then isopropanol before being transferred into a high vacuum PVD system. For certain specimens (*e.g.* Si, SiN), a plasma cleaning process was applied (5 min, 100 W) to remove the impurities and the native oxide layer at the substrate surface. A thin layer (~ 50 nm) of C (100 W DC) or TiC (150 W RF) was then deposited onto the specimen surface via magnetron sputtering at room temperature to assist with the whisker growth. The synthesis of the metal whiskers was carried out in the UHV-MBE chamber. An elevated substrate temperature is required to activate the surface diffusion, which is crucial for the nucleation and subsequent growth of the whiskers. In general, the growth temperature is about 60% of the melting temperature. Depending on the material, whisker growth was obtained only on certain substrates with or without the mediating layers. The exact growth parameters are listed in Table 2.1. The deposition rate was 0.05 nm/s. Constant rotation of the specimen plate around its surface normal was applied during the entire process to ensure the homogeneity of the deposition. The nominal film thickness was measured with a quartz balance. In some cases, whisker growth was directly

obtained on Mo and W wires (0.45 μm diameter) without any pretreatment. It was believed that in these cases the whisker growth was aided by the surface defects and contaminations.

Table 2.1 Parameters for the whiskers growth.

| Material | Crystal structure | Substrate | Mediating layer | Temperature (°C) |
|---|---|---|---|---|
| Cu | FCC | Au grid, SiN, Mo wire, W wire | C | 600 - 700 |
| Cu-Si | HCP | Si | C | 630 - 700 |
| Ag | FCC | Si | C | 600 - 650 |
| Ni | FCC | Mo wire, W wire | - | 760 |
| Co | FCC-HCP | Mo wire, W wire | - | 760 |
| Fe | BCC | Mo wire, W wire, STO | TiC on STO | 780, 850 |
| Fe-Si | Tetragonal | Si | C | 800 - 950 |
| Cu-Fe | FCC-BCC | Au grid, Mo wire | C | 650 |
| Cu-Fe-Si | HCP – Orthorhombic | Si | C | 630 - 700 |
| Cu-Ni | FCC-FCC | SiN, Au grid | C | 650 |
| Cu-Ni-Si | - | Si | C | 650 |
| Au-Ni | FCC-FCC | W wire | - | 760 |

The majority of the characterization in this work was carried out with Transmission Electron Microscopy (TEM). TEM measurements normally require the specimen to be no thicker than 100 nm. No additional preparation was performed in this work since the whiskers, with their diameters ranging from 50 to 200 nm, were already thin enough. For the observations, the whiskers were collected and transferred to a TEM grid with the standard scratch method where they remained steadily on the lacey carbon support

film during the whole investigation process. For more comprehensive studies, cross-sectional lamellae of the whiskers were cut out using Focused Ion Beam (FIB).

From our previous work, we have concluded that for some materials, (*e.g.* Cu, Ag) the whisker growth was mediated by the deposited C layer [152]. Therefore, it is in principle possible to growth whiskers directly on a TEM grid with carbon film. By doing so, the TEM investigations can be performed under the pristine condition, that is, without introducing extra mechanical force or damages into the structures.

## 2.2 Scanning Electron Microscopy

The first microscopic analysis method applied in this work is the Scanning Electron Microscopy (SEM). SEM provides information on mostly the topography and the chemical composition of the sample surface. A tungsten filament or a field emission gun (FEG) is used to generate the electron beam with a typical energy between 1 and 30 keV. A set of condenser lenses is then used to focus the beam to a spot about 1 to 5 nm in diameter. The scanning at the sample surface is achieved by the deflection of the electron beam with pairs of scanning coils. The teardrop shaped region into which the electrons penetrate is known as the interaction volume, and is illustrated in Figure 2.2. This volume depends on the electron energy and on the sample properties (atomic number, density, *etc.*), but in general does not extend further than 5 μm beneath the surface. The technique is thus considered highly surface sensitive. Each particular interaction between the sample and the incident electrons produces a different type of contrast, which can be used in imaging. Each resulted image then contains different information with regard to the sample surface.

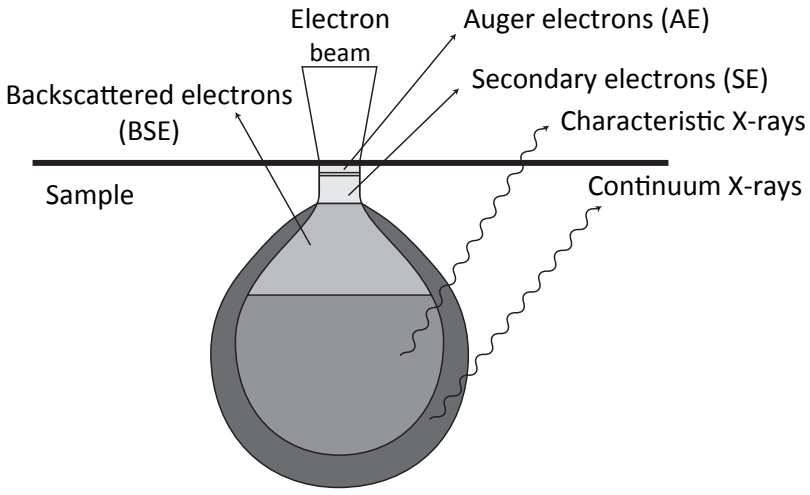


Figure 2.2 Schematic representation of the interaction volume and the generation of secondary electrons, backscattered electrons and characteristic X-rays.

The most common source of imaging contrast is the Secondary Electrons (SE). These are the low energy electrons (< 50 eV) ejected by inelastic scattering. Their short escape distance (few nm) makes them ideal for high-resolution topography imaging of the surface morphology. The electrons produced by elastic scattering can also be used. These are the electrons being reflected or backscattered (hence the name backscattered electrons or BSE) of the incident beam. Because of their high-energy, the BSEs can escape from a deeper (~ 1 μm) and larger volume beneath the surface, resulting in a relatively worse lateral resolution compared to secondary electron images. However, since heavier elements backscatter electrons more strongly (*i.e*. brighter contrast) than lighter ones, the BSEs can be used to detect compositional changes across the surface areas (so-called Z contrast). Moreover, the BSE intensity is sensitive to the magnetic domain structure [153] and to the crystallographic orientation of the sample. The technique that exploits the latter is called Electron Back Scatter Diffraction (EBSD). Finally, characteristic X-rays and Auger electrons are emitted when an inner shell electron is removed from sample during the interaction with the incident electron beam. The techniques associated with the detection of (imaging with) these emissions are Energy-Dispersive X-ray spectroscopy (EDX) and Auger Electron Spectroscopy (AES), respectively. Both techniques are capable of performing quantitative chemical analysis of the sample surface.

## 2.3 Transmission Electron Microscopy

The second microscopic analysis method applied in this work is the Transmission Electron Microscopy (TEM). TEM is a powerful tool for material analysis capable of imaging at a much higher resolution than the SEM. For an optical microscope the Rayleigh criterion writes

$$\delta = \frac{1.22\lambda}{2n\sin\theta}. \tag{2.1}$$

Here, $\delta$ is the image resolution given by the smallest distance that can be resolved, $\lambda$ is the wavelength, $n$ is the refractive index of the viewing medium, and $\theta$ is the half angle of light entering the magnifying lens. The best resolution in TEM can be estimated with

$$\delta = \frac{1.22\lambda}{\theta} \tag{2.2}$$

Obviously, the resolving power can be improved by simply decreasing the wavelength $\lambda$. This can be achieved by increasing the energy of the electron beam (High Voltage TEM) as

$$\lambda = \frac{1.22}{\sqrt{E}} \tag{2.3}$$

$E$ is the energy (in eV) and $\lambda$ is the wavelength (in nm) of the electrons. The High Voltage TEM (JOEL ARM 1250) used in this work, one of the three 1.2 MV models constructed in the 1990s, features the best resolution at the time of about 1.2 Å. The main obstacles that prevent the theoretical resolution of a TEM to be realized are the aberrations introduced by the electro-magnetic lenses. Recent progress in spherical and chromatic aberration corrections has allowed ultra-high-resolution to be achieved at lower voltage. For instance, the latest FEI Titan™ is capable of producing images with an astonishing resolution of below 50 pm at 300 kV! Compared to other microscopic characterization methods (Transmission X-ray Microscope, Scanning Tunneling Microscope, Atomic Force Microscope, *etc.*), the application of TEM is limited by its laborious sample preparation and its requirement on the sample thickness. As a matter of fact, due to the low penetration power (strong interactions) of the electron beam, the thickness of an electron transparent sample is often less than 100 nm.

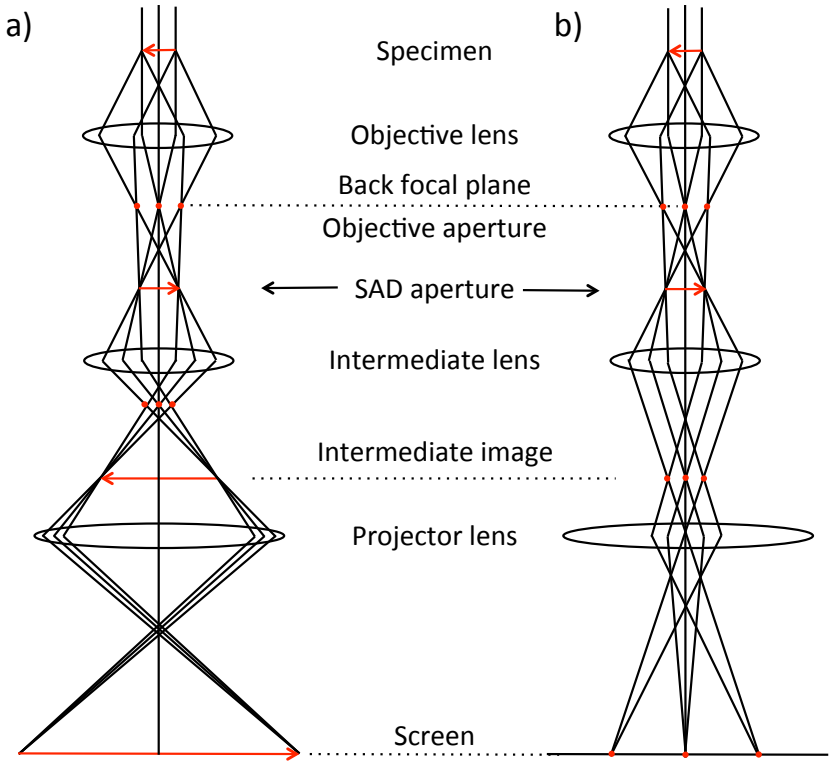


Figure 2.3 Schematic illustration of the (a) image mode and (b) diffraction mode [154].

A TEM is essentially a number of consecutive electron optics carefully positioned in between the electron gun (on the top) and the viewing screen (on the bottom of the TEM column). A typical system consisting of four magnetic lens and two apertures is shown in Figure 2.3. The sample is illuminated by a parallel beam of electrons (ideally a plane wave). A set of condenser lenses (not shown here) is placed before the sample

to achieve the parallelism and to control the spot size of the incident beam. The objective lens produces a diffraction pattern in its back focal plane and an absorption image of the sample in its image plane.

The switching between the two operation modes (image mode and diffraction mode) is realized by changing the focusing power of the intermediate lens. With weaker focusing power (larger focal distance), the intermediate lens produces a magnified image of the diffraction pattern at its image plane. With stronger focusing power (shorter focal distance), the intermediate lens produces at the same position a magnified absorption image of the sample. Finally, a projector lens is used to generate, on the viewing screen, the final image (of diffraction pattern or absorption image) from the intermediate image plane. Additionally, one can select part of the diffracted beam to form the final image by adjusting the objective aperture located at the back focal plane of the objective lens. One can also select part of the sample for the diffraction analysis by inserting and adjusting the selected area diffraction (SAD) aperture located at the image plane of the objective lens. The diffraction pattern obtained is called selected area diffraction pattern (SADP). Alternatively, by illuminating the sample with a convergent (rather than parallel) beam, it is possible to perform pure diffraction experiment with simultaneously multiple incident angles. The technique is known as Convergent Beam Electron Diffraction (CBED) and has the benefit of revealing the 3D symmetry of the crystalline sample.

## 2.3.1 Bright Field and Dark Field Imaging

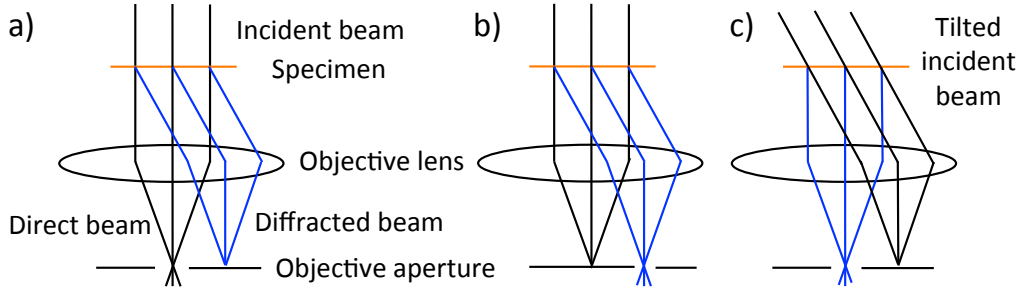


Figure 2.4 Ray diagram of different image modes: (a) BF; (b) displaced-aperture DF and (c) centered DF [154].

There are different operation modes under the image mode. The final diffraction pattern comprises of a bright central spot (direct beam) surrounded by a number of weaker spots (diffracted beam by different crystal planes). As mentioned earlier, it is possible to use only part of the diffracted beam to form the final image by blocking the rest with the objective aperture. When it is the direct beam (*i.e.* zero order diffraction) that is let through (Figure 2.4-a), the contrast is generated entirely by the occlusion and absorption of the incident beam. Regions with larger sample thickness or with higher Z materials appear darker on the image whereas regions with thinner sample or without the sample

appear brighter. The mode is known as “bright field (BF) imaging”. When it is the diffracted electrons fulfilling one specific Bragg condition that are let through (Figure 2.4-b), what is observed is the diffraction contrast of the sample. Regions of the sample not diffracting in the selected direction appear darker on the image. The mode is thus known as “dark field (DF) imaging”. Note that despite what is implied in their names, the bright and dark field imaging are not exactly complementary. For instance, a part of the sample may appear dark on both the bright and the dark field images if it strongly absorbs the incident electrons yet does not scatter them along the Bragg angle selected by the dark field objective aperture.

It is worth mentioning that the dark field imaging itself can be realized in two different methods. The first is to displace the objective aperture to the diffraction spot (displaced aperture DF, Figure 2.4-b). This method is straightforward and easier to manipulate but suffers from poor image quality due to additional spherical aberrations and astigmatism. The second is to deflect the incident beam (electron gun) to fit the diffracted beam through the centered aperture (centered DF, Figure 2.4-c). Centered DF should always be used whenever it is necessary to acquire high quality dark field images.

### 2.3.2 High-Resolution TEM

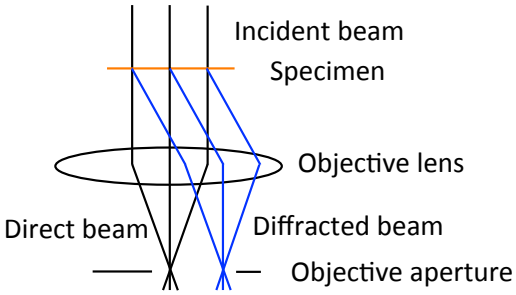


Figure 2.5 Ray diagram of the HRTEM mode.

The High-Resolution Transmission Electron Microscopy (HRTEM) mode or phase contrast mode is achieved when two beams, the direct beam and one of the diffracted beams, are accepted by the objective aperture (Figure 2.5). The result is a set of parallel fringes with alternating bright (maximum intensity) and dark (minimum intensity) lines. The spacing between adjacent bright (or dark) lines is equal to the interplanar distance of the crystal planes selected by the diffracted beam condition, but the positions of the fringes (bright or dark) do not represent at all the actual position of the said crystal planes. Moreover, since the momentum transfer of the diffracted beam is almost at right angles to the incident beam, the diffracting crystal planes can only be those orientated near perpendicular to the sample surface (so called “edge on”). If more than one diffracted spot is permitted in the objective aperture, multiple families of crystal planes can be probed at the same time. Once again, the fringes only infer the interplanar distance

and the in-(surface)-plane projection of the diffracting crystal planes, not their actual positions. HRTEM has been used extensively for the analysis of crystal structures and lattice imperfections in various kinds of materials with a sub-atomic resolution. More specifically, it can be applied in the characterization of point defects, stacking faults, dislocations, precipitates grain boundaries and surface structures. For more accurate interpretation of the HRTEM images (*e.g.* atom positions), computer simulation is required which takes into account both the propagation of the incident beam through the sample and the phase contrast induced by the TEM optics (sample thickness and defocus).

## 2.3.3 STEM and HAADF

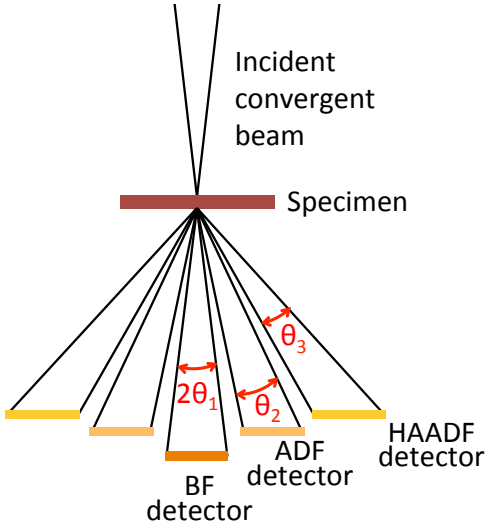


Figure 2.6 Schematic of detector setup in a STEM. The BF detector collects electrons with a scattering angle of $\theta_1 < 10$ mrads, the ADF detector and HAADF detector collect electrons with a scattering angle of $10 < \theta_2 < 50$ and $\theta_3 > 50$ mrads, respectively.

Generally speaking, a Scanning Transmission Electron Microscope (STEM) is a TEM equipped with scanning coils and additional detectors. Instead of a parallel incident beam, a convergent electron beam is used to scan the sample surface in a raster pattern (like in SEM). Conceptually, there is no lens after the sample. This has the advantage of avoiding the aberrations introduced by the post-sample optics. (Figure 2.6) Several detectors are placed at the image plane of the projector lens, where a diffraction pattern of the sample is produced. Their finite angular acceptance makes it that each detector only detects electrons from a certain range of scattering angles. The direct transmitted beam (or zero order diffraction beam) is collected by the BF detector, which is positioned at the center of the diffraction pattern. Some of the scattered electrons are collected by the annular DF (ADF) detectors positioned at moderate scattering angles (10-50 mrad) and by the high-angle ADF (HAADF) detectors at high scattering angles (> 50

mrad). At such high angles, the HAADF image is formed with incoherently scattered electrons (as opposed to Bragg scattered ones) which are sensitive to the atomic number of the materials (*Z*-contrast).

One important advantage of the STEM mode is that it allows different signals (secondary electrons, scattered electrons, characteristic X-rays, and electron energy loss) to be spatially correlated in one analysis, which is not possible for conventional TEM operations.

### 2.3.4 X-ray Energy-Dispersive Spectroscopy

The convergent electron beam used in STEM is also very useful for localized composition (chemical) analysis. The characteristic X-rays (Figure 2.2) generated due to the ground state excitation of the sample is element specific, as each element has a unique set of peaks on its electromagnetic emission spectrum. One of the techniques that exploit these photon emissions is the X-ray energy-dispersive spectroscopy (XEDS, EDX, EDS). An elemental mapping can be easily generated by the rastering of the focused electron beam at the sample surface.

### 2.3.5 Electron Energy Loss Spectroscopy

An incident electron may be inelastically scattered when it interacts with the atomic electrons in the sample. The energy loss during this interaction is indicative of the nature and bonding state of the scattering atom. The technique that measures the amount of energy loss is called electron energy loss spectrometry (EELS). EELS is, to a certain extent, complementary to the EDX technique. While the latter is particularly sensitive to heavier elements (large *Z* number), the former excels at identifying light elements where the excitation edges tend to be sharp and well defined. For single element materials, EELS can easily tell the difference between different allotropes (such as diamond, graphite or amorphous carbon). For compound materials, EELS is capable of distinguishing the different oxidation state of elements of up to 3d transition metals.

The EELS detector is often found in the back focal plane of the projector lens. A typical EELS spectrum consists of essentially three parts. The intense peak found at 0 eV (called the zero loss peak) represents all the non-scattered and elastically scattered electrons. The low energy loss (or valance) region till about 50 eV is the result of electron interactions with the weakly bonded outer electrons of the sample atoms. This region contains information on the band structure (in particular the dielectric properties, *e.g.* plasmons) of a material. The last region is called the high-energy loss region (> 50 eV) and is representative of the electron interactions with strongly bonded inner electrons of the sample atoms. The spectrum in this region shows some element-specific

features (called the ionization edges) which are useful for qualitative chemical analysis of the sample. It is worth mentioning that the spatial resolution of EELS (0.1 nm) is in principle better than the corresponding EDX measurement as the latter is affected by beam broadening effects in all but the thinnest samples. The energy resolution of EELS is also (more than 10 times) better than that of EDX.

## 2.4 Electron Holography

The conventional TEM imaging modes (BF, DF) focus mainly on the structural characterization of the materials. Only (the squared modulus of) the amplitude of the electron wave exiting the sample is recorded on the detector; any information related to the phase is lost in the process. The phase of the exit wave is sensitive to the electrical and magnetic field of the electrons passing through the sample, which is fundamental to the studies of semiconductor and ferromagnetic materials. Electron holography offers an elegant solution. By superimposing the image wave with a coherent reference wave, an interferogram or hologram is recorded, from which the amplitude image and the phase image of the sample object can then be separately reconstructed. The phase image contains information on the in-plane component of the magnetic induction and the electrostatic potential in the sample, thus allowing for quantitative determination of the electrical and magnetic properties of the materials with a spatial resolution of just a few nanometers [155,156].

Although the term holography (Latin for "whole message") and the technique itself was initially conceived by Dennis Gabor [157,158] in 1947 as a way to improve the image quality (correct the spherical aberrations) in early generation TEMs, the development of electron holography was lagging significantly behind its optical (*e.g.* laser) counterparts due to the lack of a coherent source. Modern-day TEMs use field emission guns (FEG) to generate highly coherent electron sources. There are more than 20 possible configurations for electron holography [159], of which the most popular one being the off-axis scheme (Figure 2.7-a) invented by Möllenstedt and Düker [160]. It employs an electron biprism, which is basically an ultrafine conductive fiber positioned in the imaging lens, to split the field of view into two parts. A thin TEM sample is inserted in the path of one part of the incident beam. When a positive voltage is applied to the fiber, the reference and the scattered electron waves on either side of the fiber are bent towards each other, forming an interference fringe pattern (hologram) in the overlap area. This hologram is then numerically processed to produce separate amplitude and phase images. Optionally, a Lorentz lens (a small einzel-lens positioned below the sample) may be used to keep the sample in a magnetic-field-free environment. The use of the Lorentz lens (objective lens switched off) comes at the cost of a limited magnification ratio (up to 80000:1).

A standard hologram recording and reconstruction process is shown in Figure 2.7. An off-axis hologram of the sample is first recorded (Figure 2.7-b). The sample concerned here is a cross-sectional lamella of a Ni whisker prepared in this work. The interference fringes are clearly visible in the zoomed-in image in Figure 2.7-c. A Fourier transform of the hologram is then performed. The result is a complex 2D frequency map composed of an autocorrelation center band and two mutually conjugated sidebands. The center band is in essence the conventional image. It does not contain the image phase and is thus not of interest here. The two sidebands are equivalent and redundant in that one of them contains already Fourier-spectrum of the complete image wave. The separation between the two sideband spots in Figure 2.7-d is due to the relative tilt between the object and the reference waves, which depends on the voltage applied to the biprism. The intensity variations around the spots reflect the local phase shifts of the electron wave function caused by the sample.

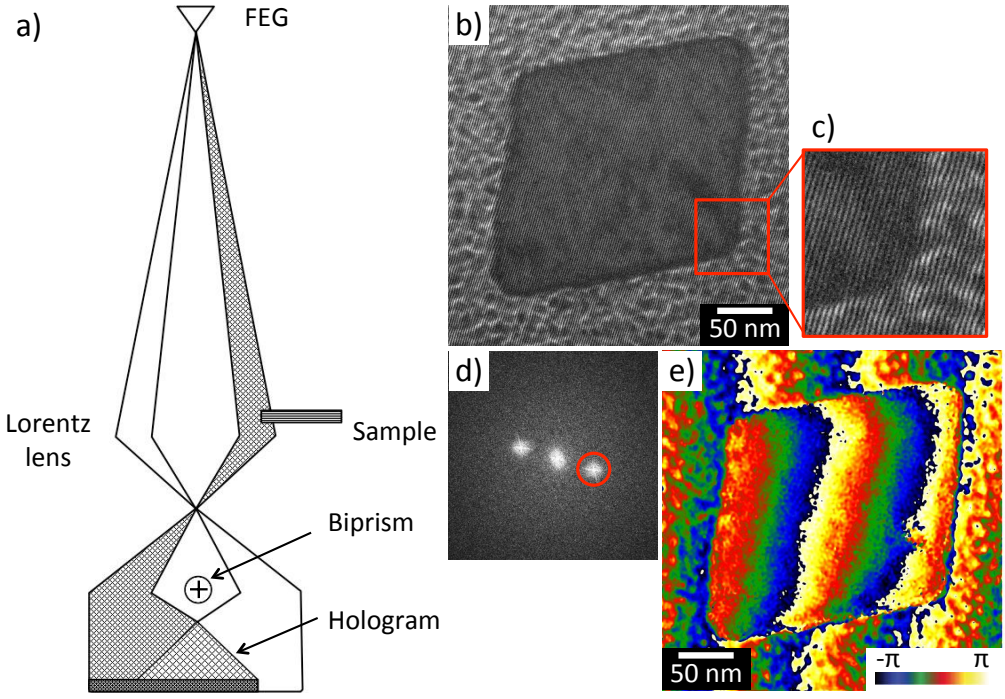


Figure 2.7 (a) Schematic illustration of the off-axis electron holography mode (adopted from [155]); (b) off-axis electron hologram of a Ni whisker cross-sectional lamella; (c) enlargement showing interference fringes; (d) Fourier transform of the electron hologram b; (e) phase image obtained after inverse Fourier transformation of the sideband marked with red circle in (d). The observed phase discontinuities (modulo $2\pi$) can be unwrapped by applying phase unwrapping algorithms.

Only one of the two sidebands is needed for the reconstruction process. This sideband is re-positioned to the center of the complex image with its twin sideband and the center band masked to zero. An inverse Fourier transform is then applied. The final phase and amplitude images are obtained separately from the resulting complex image with

$$\phi = \arctan(i/r), \tag{2.4}$$

$$A = \sqrt{r^2 + i^2}. \tag{2.5}$$

$r$ and $i$ are the real and imaginary parts of the wavefunction, respectively. The reconstructed phase image is shown in Figure 2.7-e. The phase discontinuities observed is a mere artifact (*i.e.* not sample related) arising from the modulo operation. Nevertheless, a phase-unwrapping algorithm is recommended for unwrapping the phase and for ensuring a reliable interpretation of the reconstructed images [161]. Very often, a reference hologram is recorded with the sample removed from the incident beam. The reconstructed reference wave is used to correct artificial phase structures (geometric distortions, charging effects, *etc.*) and mistilt of the reconstructed wave (improper centering of the sideband). Dividing the sample wave function by the reference wave function can in addition serve to normalize the amplitude $A$.

The phase shift of the electron wave as it passes through the sample is mainly induced by two factors, the mean inner potential (MIP) of the sample and the in-plane component of the magnetic field (MAG). Neglecting dynamical scattering, the total phase difference between the electron wave after the sample and the reference wave in vacuum is the integration of the phase changes along the incident beam direction, with

$$\phi(x) = C_E \int V(x,z)dz - \left(\frac{e}{\hbar}\right) \iint B_\perp(x,z)dxdz, \tag{2.6}$$

where

$$C_E = \left(\frac{2\pi}{\lambda}\right)\left(\frac{E + E_0}{E(E + 2E_0)}\right). \tag{2.7}$$

$z$ is along the incident beam direction, $x$ is an arbitrary direction in the sample plane, $V$ is the mean inner potential, $B_\perp$ is the in-plane component of the magnetic induction perpendicular to $x$. $E$ and $E_0$ are respectively the kinetic and rest mass energies of the incident electron.

Of the two factors, MIP is the principal contributor to the phase shift measured in magnetic nanostructures. Although the amplitude image alone is in theory sufficient for the estimation of the phase shift caused by the MIP, to do so requires an accurate knowledge of the mean free path of inelastic scattering for each material in the sample. Consequently, the phase shifts from the MIP and the MAG are calculated from the phase image. A schematic of their respective contributions is shown in -a for a whisker with homogeneous composition magnetized along its axial direction. If, in addition, a second hologram is recorded with the sample inverted (180°), then the sum of two phase images shall yield (twice) the MIP contribution while their difference shall yield (twice) the MAG contribution [162].

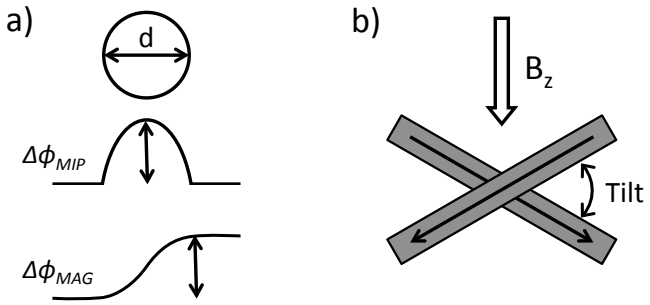


Figure 2.8 (a) Contributions of the MIP and the MAG to the phase shift in a whisker. (b) Schematic illustration of using the specimen tilt to provide the in-plane component of the external field for *in situ* magnetization reversal experiments.

Alternatively, the second hologram can be acquired with the same sample orientation but under a different accelerating voltage. Since the MAG contribution is independent of the accelerating voltage, subtracting the second phase image from the first one would directly yield the MIP contribution. In the event that neither of the above methods can be performed (*i.e.* inverting the sample or changing the accelerating voltage), the Lorentz lens is used instead. The reversal of the magnetization is achieved by tilting the specimen holder in the known magnetic field of the objective lens (-b). The calculation of the two contributors to the total phase shift follows the same as what was described in the sample inverting scheme. Finally, more advanced techniques based on holography principles have been developed which allow for the precise determinations of sample thickness (to atomic dimensions), magnetic lines of force (in magnetic samples) and equipotential lines (in electrostatic samples) [163].

# 3 Morphology and Crystal Structure

This chapter deals with the morphology and the crystal structure of the metallic whiskers synthesized over the course of this work. The main characterizations methods were SEM and TEM. Successful synthesis of Au, Ag, Ni, Co, Fe and their alloy whiskers has been achieved on various substrates (Paragraph 2.1.2). In general, the growth conditions of these whiskers were similar, but the substrate morphology and the whisker crystal structure (crystallographic orientations, defects) were specific to each material.

## 3.1 Whiskers of IB Metals and Alloy

Research interests in IB transition metals are mostly stimulated by their excellent electrical, thermal conductivity and their outstanding mechanical properties. Besides, Au and Ag are resistant to corrosion, which makes them the suitable candidate for making precision instruments. The materials in this group all have FCC crystal structure as the stable phase under both growth and ambient condition. The whiskers synthesized in this work were composed of mostly defect free single crystals, which were perfect for the analysis of the material properties as well as for the understanding of the origin and the evolution of crystal defects under mechanical deformation. More importantly, metals in the group are also the ideal system for studying the growth mechanism of the whiskers thanks to their relatively simple crystallographic structure and their stable growth process.

### 3.1.1 Cu

Cu whiskers were successfully synthesized on different substrates (Table 2.1). On Si, SiN, $Al_2O_3$ and MgO, the whiskers were observed only when the surface was covered by a deposited carbon layer. TEM grids with a lacey carbon film can also be used as the substrate for Cu whisker growth. The microstructures grown on a TEM grid (Figure 3.1-a) showed no difference compared to those grown on a SiN substrate with a carbon layer (Figure 3.1-b). The use of the carbon layer, however, is not always necessary. Cu whiskers were also obtained on W and Mo wires without any carbon depositions. It is believed that in these cases the impurities and the defects on the surface facilitated the whisker growth similar to what the carbon layer achieved on the other substrates. The detailed whisker growth conditions and growth mechanisms will be further discussed in Chapter 5.

In additional to whiskers, blades, platelets, and islands were also observed on the sample surface. The different microstructures were marked accordingly in Figure 3.1-a. The microstructure of interest in this work is the whisker. The whiskers synthesized in this work usually have a "diameter" (defined as the longest distance between two opposing sidewalls) of in between 20 and 300 nm, and a length of 2 to 100 µm. The main feature of the whiskers is their very high aspect ratio, which can reach up to 1000:1. Both the term blade and platelet refer to flat microstructures of less than 300 nm thick. The former has a rectangular base of often more than 5 µm long and 500 nm to 2 µm wide, while the latter has a triangular or orthorhombic base of the size of several micrometers. The thickness of the blades and the platelets are comparable with the diameter of the whiskers, about 20-300 nm. The whiskers, blades and platelets are all single crystal structures with well-defined facets. The other microstructures that can be found at the surface are small polycrystalline islands of random shapes.

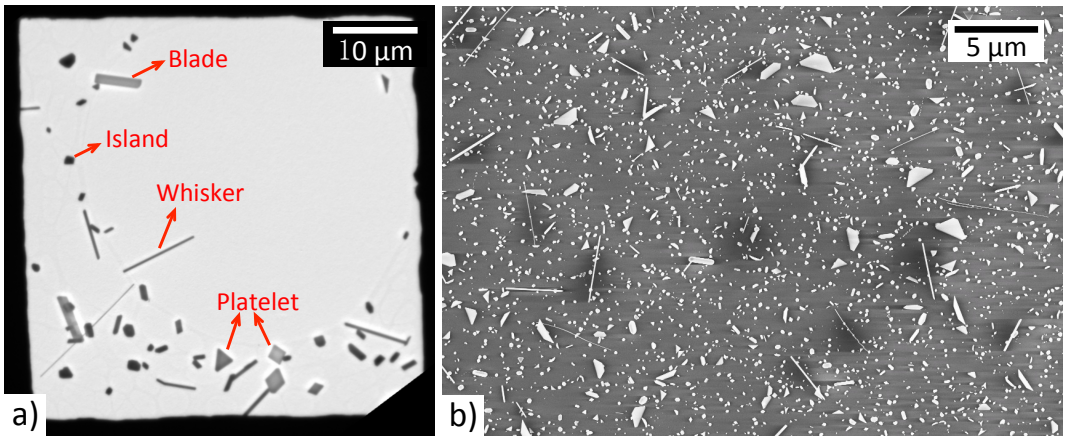


Figure 3.1 (a) TEM micrograph of a Au TEM grid with a lacey carbon film and (b) SEM micrograph of a SiN substrate with a 50 nm carbon layer after 180 nm (nominal value) of Cu deposition at 700 °C, from which Cu whiskers, platelets and islands are observed.

Like thin film growth, whisker growth is also a competitive process between adsorption and desorption (see section 1.3). The morphology of the microstructures after growth is hence strongly affected by diffusion, which is in turn influenced by the growth temperature. This is hardly surprising given that whisker growth (finite diameter) can be considered as a special case of thin film growth (infinite diameter). The temperature window for growing Cu whiskers was established as ~ 600 - 700 °C from our experiments. The morphologies of the microstructures grown at different temperatures were slightly different. This is shown in Figure 3.2, for the growth on Cu TEM grids at 600 °C, 650 °C and 700 °C, respectively. It can be concluded from these figures that while the density of the microstructures (whiskers, blades, platelets and islands) decreases, their size increases significantly for increasing growth temperature, with 700 °C being the most favorable temperature for whisker growth. The result can be understood as follows. At lower temperatures, the nucleation density is high due to the low adatom mobility on

the substrate surface. The growth is thus limited by the fierce competition for material among the numerous nuclei. At relatively high temperatures, the same amount of material is shared between less nuclei, resulting in longer (whiskers, blades) and larger (islands, platelets) objects. For even higher temperatures, the desorption rate surpasses the adsorption rate. The growth process is hindered by a lack of material, leading to a clean surface without the presence of any objects.

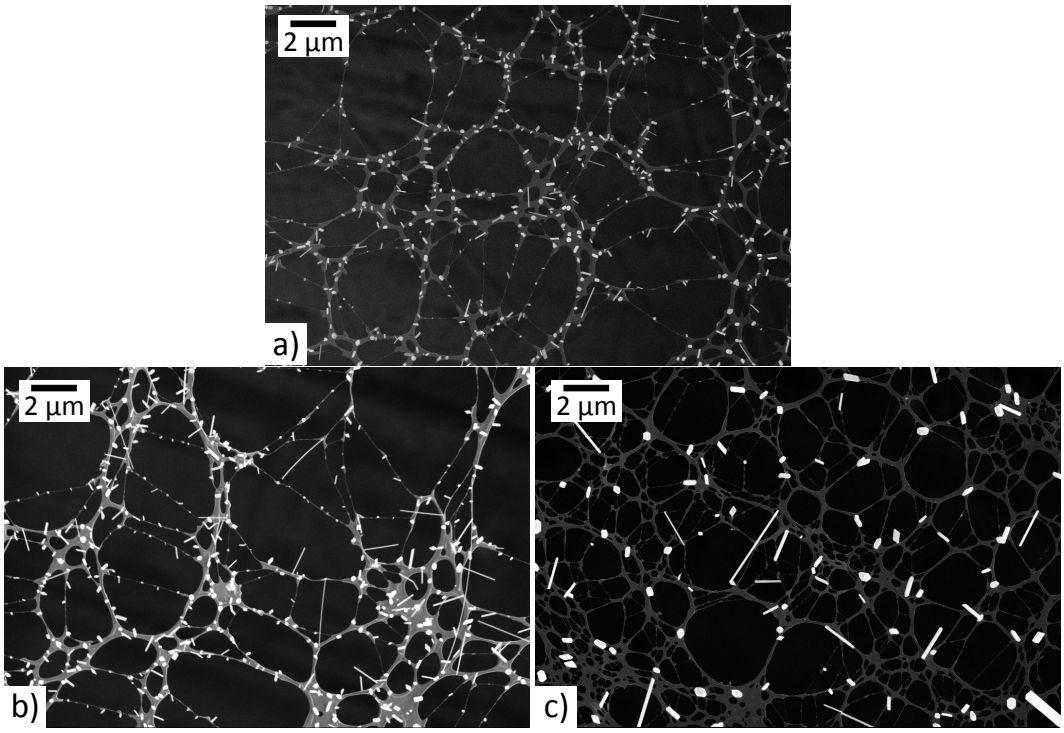


Figure 3.2 SEM micrographs of the result of Cu whiskers growth on Au TEM grids with lacey carbon film at (a) 600 °C, (b) 650 °C and (c) 700 °C after 30 nm (nominal value) of Cu deposition. The images were taken under the same magnification.

The crystal structure of the Cu whiskers has previously been investigated by our group, which revealed the growth direction to be along the <110> crystallographic direction [68]. The same is shown in Figure 3.3-a for a Cu whisker synthesized in this work. The cross-sectional shape of the whiskers is a quasi-hexagon confined by 2 {100} and 4 {111} planes as depicted by the extended Wulff-construction in Figure 3.3-b. Figure 3.3-c shows the TEM micrograph and electron diffraction pattern of a Cu platelet. The flat surface of the platelet is perpendicular to the incident beam, indicating that its largest surface plane is in fact the {111} crystal plane. Figure 3.3-d shows the zoomed-in image of the part of the very same platelet in contact with the carbon film on the TEM grid. The thickness fringes near the edges indicate that the edges are not perfect {112} planes. Moreover, a round edge was observed at the corners where two surface planes met, implying the occurrence of a roughening transition process. Finally, measurements at different sample tilt angles seemed to suggest that the entire platelet was supported (suspended) on the TEM grid simply by its short edge (blue arrows). This

further implies that the active incorporation site between the platelet and the substrate was in fact a small area (the short edge) of merely 50 nm long and a few nm wide.

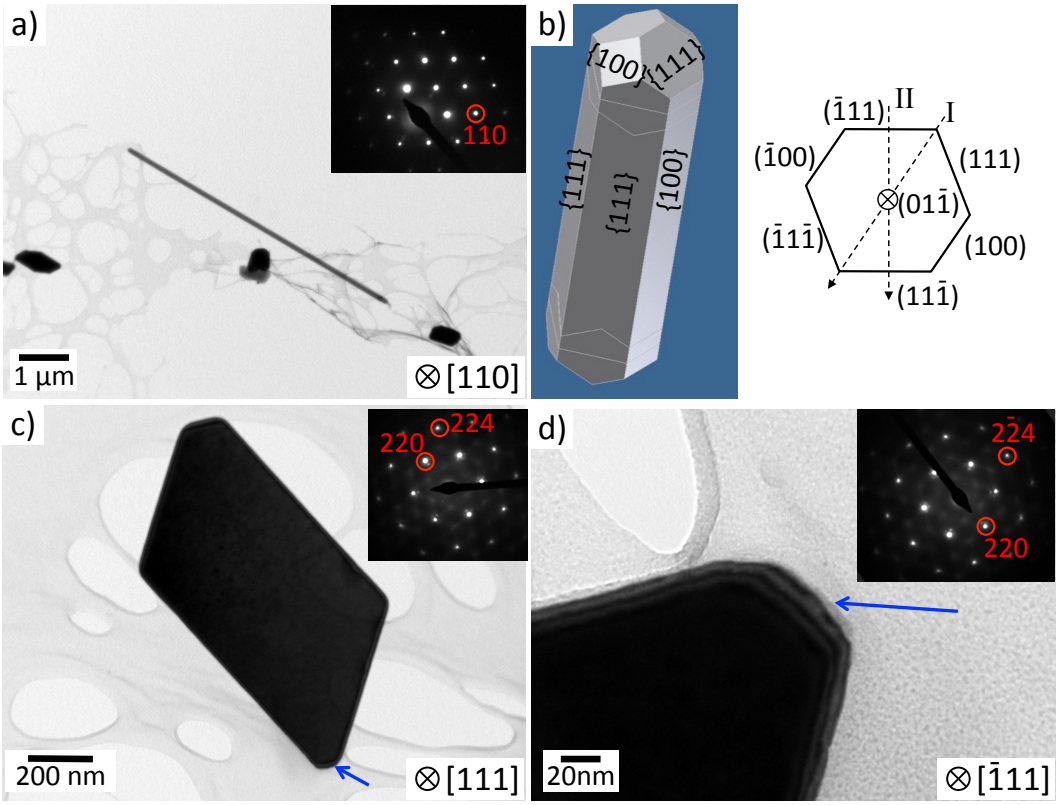


Figure 3.3 (a) TEM micrograph and (inset) corresponding electron diffraction pattern of a Cu whisker indicating that the Cu whisker grows along the <110> crystallographic direction. (b) The extended Wulff-construction of the Cu whisker. Its quasi-hexagonal cross section is confined by the {111} and {100} crystal planes. (c) TEM micrograph and (inset) corresponding electron diffraction pattern of a Cu platelet. The surface plane of the platelet is the {111} crystal plane. All the edges of the platelets are perpendicular to the <112> direction. (d) Zoomed-in image of the platelet in (c) showing the part that is in contact with the C film on the TEM grid. All the images were taken after 180 nm (nominal value) of Cu deposition at 700 °C.

Our previous results also showed that the mechanical strength of the Cu whiskers is close to the theoretical value for bulk single crystal Cu thanks to its perfect crystal structure (free of structural defects) [68].

### 3.1.2 Cu-Si

Copper silicide whiskers can also be synthesized on Si substrates if aided by a thin C layer. When depositing Cu on Si wafers, inter-diffusion takes place between the deposited Cu, the Si substrate and the silicide objects (*e.g.* whiskers or platelets) formed at the surface. An XRD diffractogram of the Si substrate after 180 nm (nominal value) of Cu deposition at 630 °C is shown in Figure 3.4-a. The result indicates the presence of $Cu_3Si$,

with a HCP lattice structure. HCP $Cu_3Si$ was also observed on the electron diffraction pattern (Figure 3.4-b) of a copper silicide whisker. The whisker axis in this case was parallel to the [0001] crystallographic direction as pointed out by the same diffraction pattern. Figure 3.4-c shows a HRTEM image of another whisker, in which three different structures can be readily identified: an amorphous oxide layer at the surface, a $Cu_3Si$ core and in-between another crystallized layer. The corresponding FFT pattern (inset) shows otherwise a crystallographic structure that is consistent with the one shown in Figure 3.4-b.

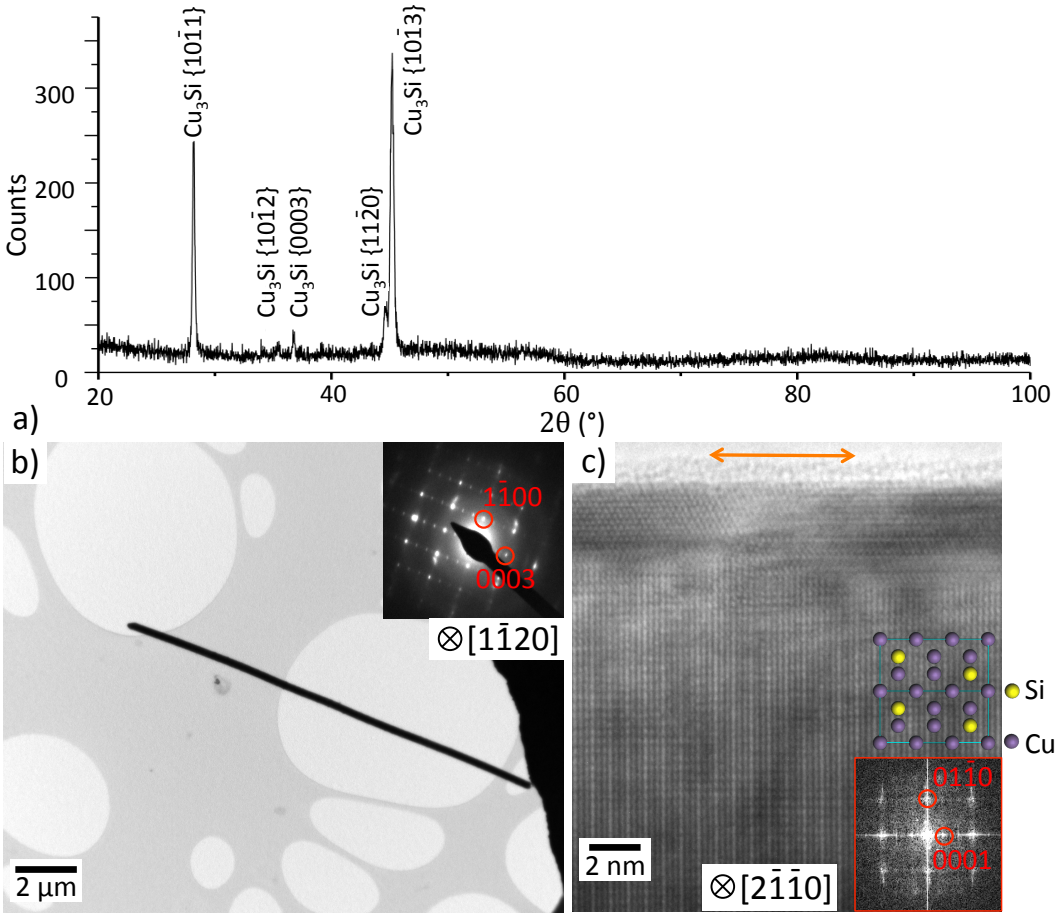


Figure 3.4 (a) XRD spectrum, (b) TEM BF micrograph and (inset) the corresponding electron diffraction pattern indicating the presence of HCP $Cu_3Si$ in the silicide whisker; (c) HRTEM image and (inset) the corresponding FFT of another whisker. A schematic atomic structure of the HCP $Cu_3Si$ is also shown. Both whiskers in (b) and (c) were grown after depositing 180 nm (nominal value) of Cu at 630°C. The axial direction of the whiskers is parallel to the [0001] crystallographic direction.

Unlike in the defect free single crystal Cu whiskers, a large amount of stacking faults were found in the $Cu_3Si$ whiskers. Typical BF and DF images of a $Cu_3Si$ whisker are shown in Figure 3.5. Here, the stacking faults manifest themselves as curved lines running across the whisker. In the BF image they showed up as dark lines while in the

DF image they showed up as bright lines as a result of the inversed contrast under different beam conditions. The DF image was taken from the diffraction spot marked by the red circle, which is not part of the HCP $Cu_3Si$ diffraction pattern. Instead, the diffraction spot is likely to be linked to the thin crystallized layer at the surface of the whisker sidewall, as it (sidewall surface) appeared brighter on the DF image.

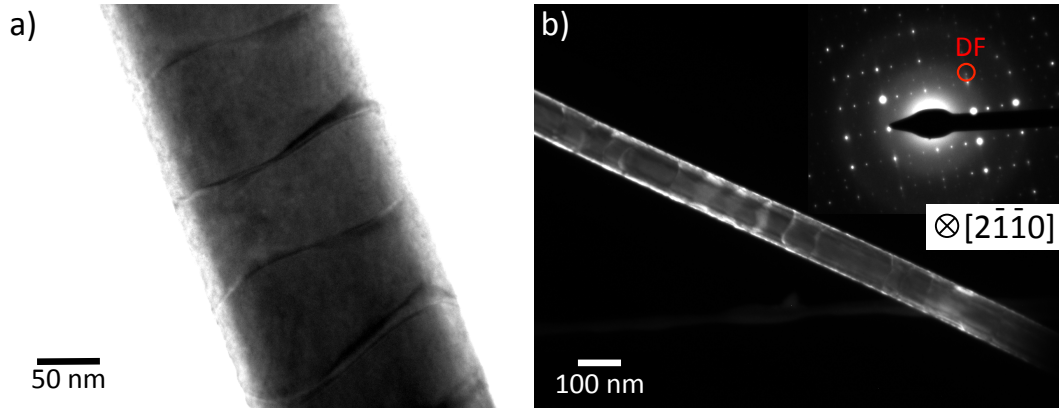


Figure 3.5 (a) BF and (b) DF TEM micrographs showing multiple stacking faults inside the $Cu_3Si$ whisker. The contrast of the image has been adjusted to enhance the visibility of the stacking faults. The whisker was grown after 180 nm (nominal value) of Cu deposition at 630 °C.

### 3.1.3 Ag

Ag is a noble metal that does not interact with any of the substrates used in our system. It forms neither silicides with the Si substrate nor carbides with the deposited carbon layer. It is also resistant to oxidation under ambient condition. As a result, Ag is considered the best candidate for investigating the growth mechanism of metallic whiskers.

Our previous experiments with Ag whiskers showed that their growth was aided by the amorphous C layer deposited with PVD. In this work, two other forms of carbon, Highly Ordered Pyrolytic Graphite (HOPG) and graphite multilayers, were used to assist the whisker growth. The latter (graphite multilayers) was prepared with the "Scotch Tape Method" commonly used in graphene fabrication: flakes of graphite layers were first peeled off from HOPG before being transferred onto a Si substrate. The flakes peeled with this method normally contain multiple layers of graphite.

The result of Ag deposition on both substrates (HOPG and graphite multilayers) is presented in Figure 3.6. The sample surface shown in Figure 3.6-a contains a cleaved area, where a piece of HOPG was broken into smaller terraces. Ag material tends to aggregate at the edges of these terraces, leaving the rest of surface relatively clean. the situation is fairly similar in the case of a graphite multilayer. Ag particles were only observed near the edges of the flakes and near the fracture lines on the flake surface. In

both cases, growth on HOPG and on graphite multilayers, only a few Ag whiskers were observed. The surface microstructures were otherwise dominated by small Ag islands. A possible explanation is that the edges contain high density of defects, which are the preferred nucleation sites for the microstructures. The high density of nuclei then resulted in a strong competition for atoms during growth, which in turn limited the chance for larger objects (whiskers, platelets and blades) to develop. The high density of nuclei can also be explained by Ehrlich-Schwoebel effect [164,165], that adatoms have to overcome additional barrier when diffusing across a step from one terrace to another.

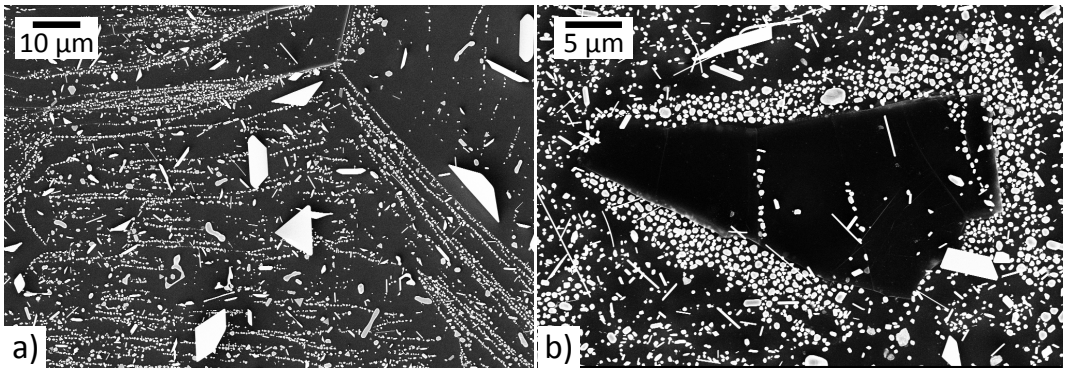


Figure 3.6 SEM micrographs of the surface of (a) HOPG and (b) a peeled graphite flake after 180 nm (nominal value) of Ag deposition at 600 °C.

Surface modification was also applied to study the growth condition for Ag whiskers. One approach was to assemble Au nano-particles (NPs) on the substrate surface. The Au NPs were prepared by Block Copolymer Micelle Lithography (BCML) [166] during which the substrates were dip-coated with Au micelle solution. The polymers were subsequently ashed and removed by $H_2$ and Ar plasma. During the dip-coating process, the central area of the substrate was covered by a thin layer of micelle solution, which contains approximately one monolayer of micelle. However, a drop of solution was left attached to the bottom edge when the substrate was pulled out of the micelle solution. This resulted in the deposition of multilayer micelles in that area.

Figure 3.7-a shows the central area of a Si substrate after deposition of Au NPs. The Au NPs automatically arranged themselves into a quasi-hexagonal pattern. The diameter of the particle was about 10 nm. The inter-particle distance was about 100 nm. After Ag deposition, the substrate surface was covered with dense Ag particles (Figure 3.7-c). There was only one whisker observed in the field of view, indicating that the Au NPs did not promote the whisker growth. For comparison, Figure 3.7-b and Figure 3.7-d were taken from an area near the bottom edge where multilayer micelle was deposited. There, a lot of Ag whiskers and platelets were observed, similar to the case where the substrate was covered by a deposited carbon layer. The size of the Ag particles in this area was much smaller compared to those found near the center of the substrate. A plausible explanation is that the residuals of the micelle polymers were burnt into car-

bon during the ashing process, which in turn facilitated the whisker growth in the same way as did the carbon layer.

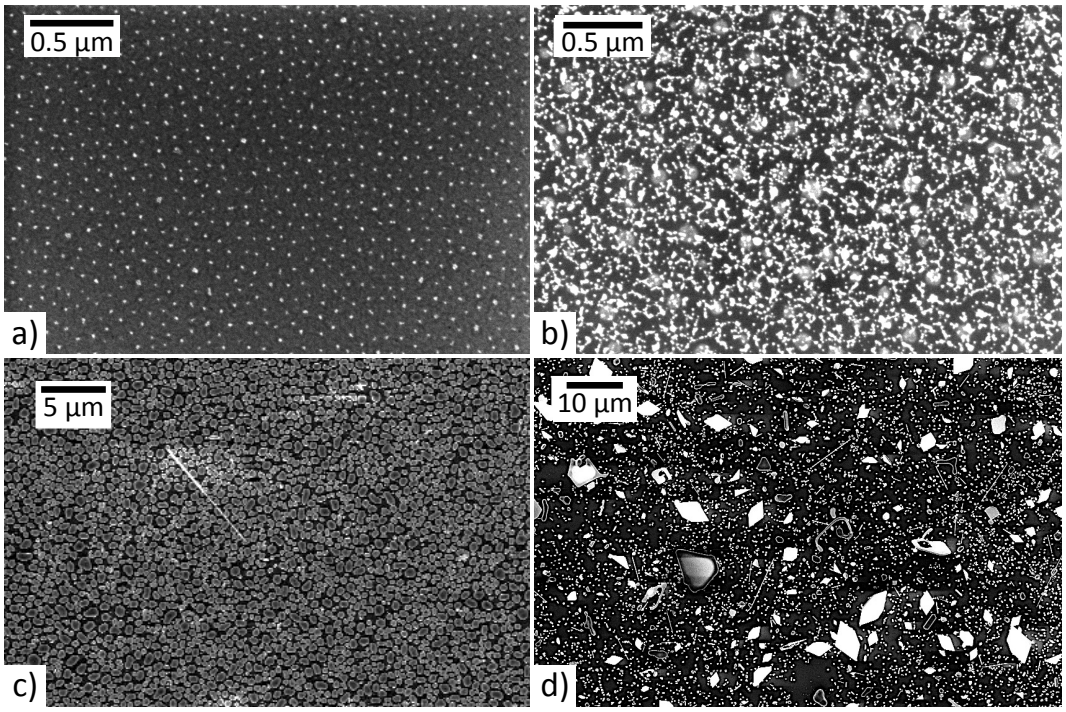


Figure 3.7 SEM micrographs showing the surface after Block Copolymer Micelle Lithography (BCML) near (a) the central area and (b) the bottom edge of the substrate. (c) and (d) are the corresponding micrographs after 180 nm (nominal value) of Ag deposition at 640 °C.

Another approach for surface modification is to etch pits into the substrates. Previous work from our group showed that the pits at the surface etched by FIB could serve as preferred nucleation sites for the whisker growth [70]. The smallest obtainable diameter of the pits in that case was about 30 nm. However, FIB preparation brings significant beam effects to the substrates, complicating the analysis of the growth mechanism in the process. Consequently, in this work Helium Ion Microscopy (HIM) was used instead. Compared to FIB, HIM can help to obtain smaller pit size and causes less beam damage.

As depicted in Figure 3.8-a and b, eight patterned arrays were created on the Si substrate covered by a 50 nm thick amorphous carbon layer. Array #1 - #4 each contains 10 × 10 rings of a given diameter. Array #5 - #8 are the same (as #4 - #1) except that the motive is a circle. The diameter $\varnothing$ of the pits and their spacing $d$ are listed in Table 3.1. From Figure 3.8-c, it is evident that the density of the microstructures is higher on the patterned area than on the rest of the surface. However, not all pits (rings or circles) had whiskers growing inside of them. Only six Ag nano-objects were observed in the high magnification image in Figure 3.8-d, including 1 whisker, 1 rhombic platelet and 4 islands, on an array of 100 pits. Since the pits in the same array are identical, the nucleation of the whiskers can only be described as a probabilistic event, *i.e.,* only a few pits

would get the chance to gather enough Ag material to form a stable nucleus which would later seed the growth of an object. However, it was not yet understood as to why some of the nuclei grew into whiskers while the others into platelets and islands. Ag also diffused into the substrate as is evident by the material contrast (small round spots in the vicinity of the Ag objects) seen in Figure 3.8. Ag diffusion into the Si substrates was also observed in another work from our group [167].

Table 3.1 Diameter (Ø) and spacing (*d*) of the pits (rings/circles).

| **Array#** | **1** | **2** | **3** | **4** | **5** | **6** | **7** | **8** |
|---|---|---|---|---|---|---|---|---|
| ***Ø* / nm** | 10 | 10 | 10 | 10 | 10 | 10 | 10 | 10 |
| ***d* / nm** | 500 | 200 | 100 | 50 | 50 | 100 | 200 | 500 |

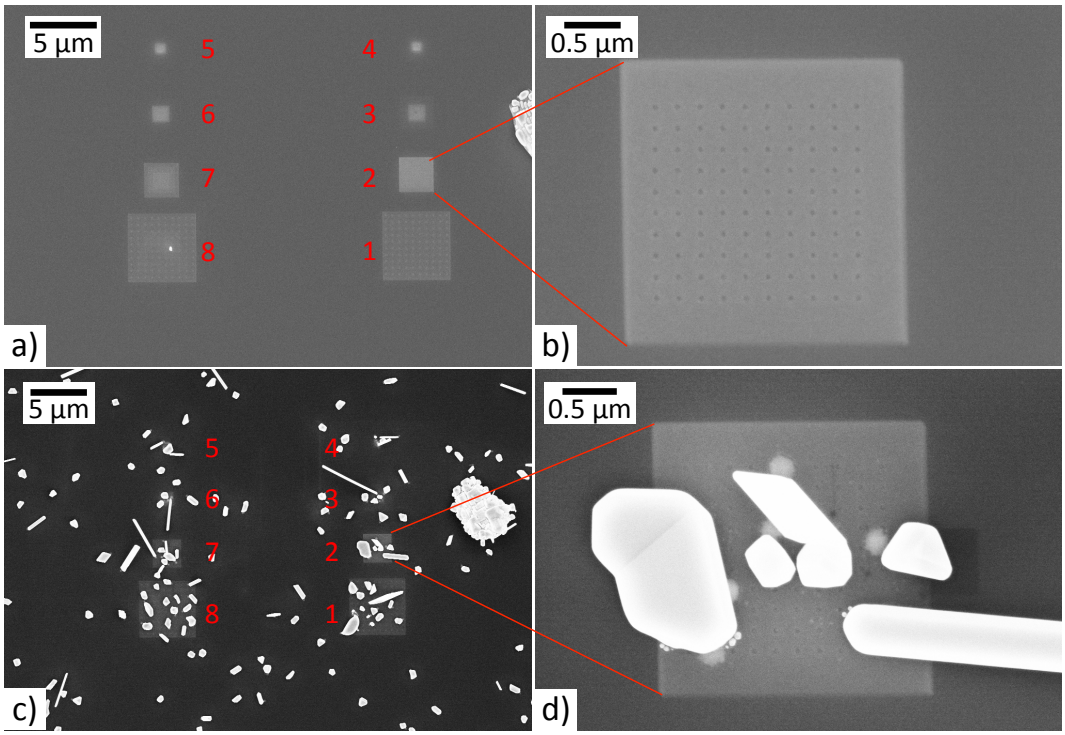


Figure 3.8 SEM micrographs of the patterned arrays etched with HIM before (a, b) and after (c, d) 180 nm (nominal value) Ag deposition at 600 °C.

TEM analysis of the crystal structure of the Ag whiskers was also performed. The Ag whiskers were single crystals with FCC structure, as expected. (Figure 3.9) The growth axis of the Ag whiskers was identified as the <110> crystallographic direction. The "clean" diffraction pattern (without additional spots from other structures) indicates that the Ag whiskers can be considered as perfect FCC single crystals.

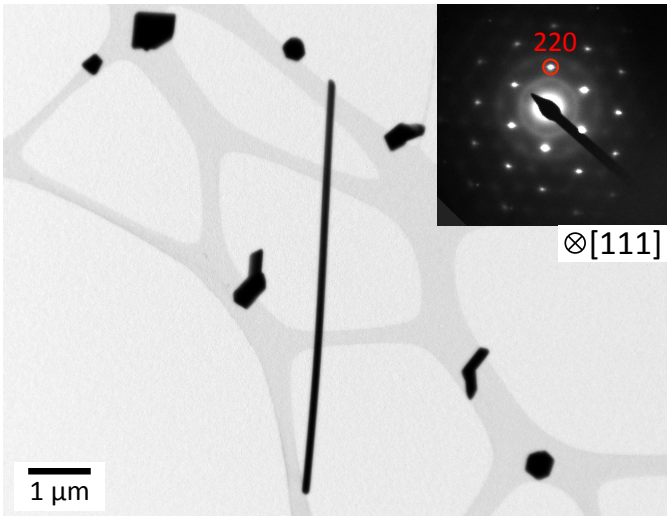


Figure 3.9 TEM micrograph and (inset) the corresponding diffraction pattern of an Ag whisker. The Ag whisker axis is along the [110] crystallographic direction.

## 3.2 Whiskers of VIII Metals and Alloy

VIII metals have been studied intensively in the literature for their excellent ferromagnetic properties due to partially filled 3d orbitals [168]. However, the phase diagram dictates that metals from this group may undergo phase transformation upon heating. In addition, they may lose their permanent magnetic properties when heated above the Curie temperature. Consequently, more complex crystal structures are to be expected inside the whiskers of these materials as a result of the inevitable cooling process (to room temperature) following their synthesis at high temperatures.

### 3.2.1 Ni

Ni whiskers were synthesized by depositing Ni onto Mo or W wires with MBE at about 760 °C. The morphology of the objects was different on the two types of substrates despite a similar growth process: a Mo (or W) wire was loaded into the MBE chamber without any preparations. The growth of the whiskers has been expected to be aided by impurities and defects on the surface.

After growth (Figure 3.10), the entire surface of the Mo wire was covered with Ni objects (whiskers, blades and platelets) whereas on the W wire surface only a few long whiskers were observed. The result is explained by the different surface conditions of the two wires, including the density of defects and impurities, the wettability of Ni as well as the mobility of Ni atoms on Mo and W surfaces. This is further supported by the fact that Ni tends to follow Frank–van der Merwe growth mode on W surfaces [169] and Stranski–Krastanov mode on Mo surfaces [170]. Despite all that, TEM observations

revealed a similar microstructure between of the whiskers grown on the two substrates. A Ni whisker scratched from the Mo wire is shown in Figure 3.11-a. The incident electron beam was parallel to the [110] crystallographic direction. The diffraction pattern agreed well with FCC Ni with a lattice parameter of 0.35 nm. With the help of the diffraction pattern, the whisker axis in the BF image was further identified as parallel to the $[\bar{1}10]$ direction. These, together with the theoretical surface energy of each crystal plane, allowed the Wulff shape of the whiskers to be constructed.

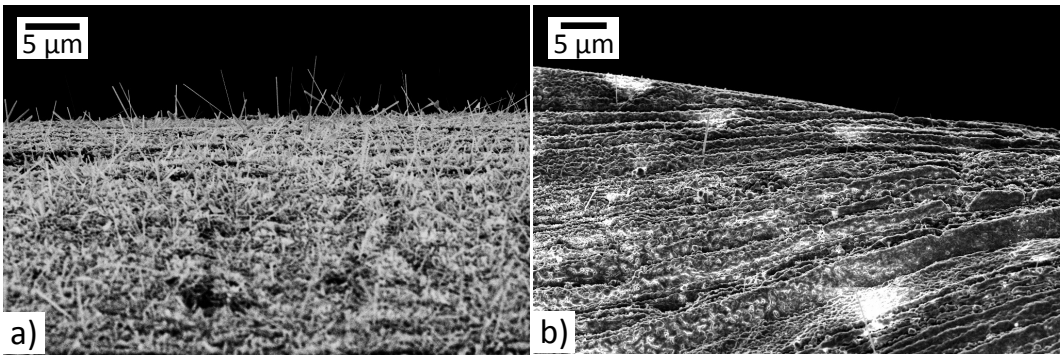


Figure 3.10 SEM micrographs of the surface of (a) a Mo and (b) a W wire after 180 nm (nominal value) of Ni deposition at 760 °C. Various microstructures (whiskers, blades and platelets) were found on the Mo wire whereas on the W wire only a few long whiskers were observed.

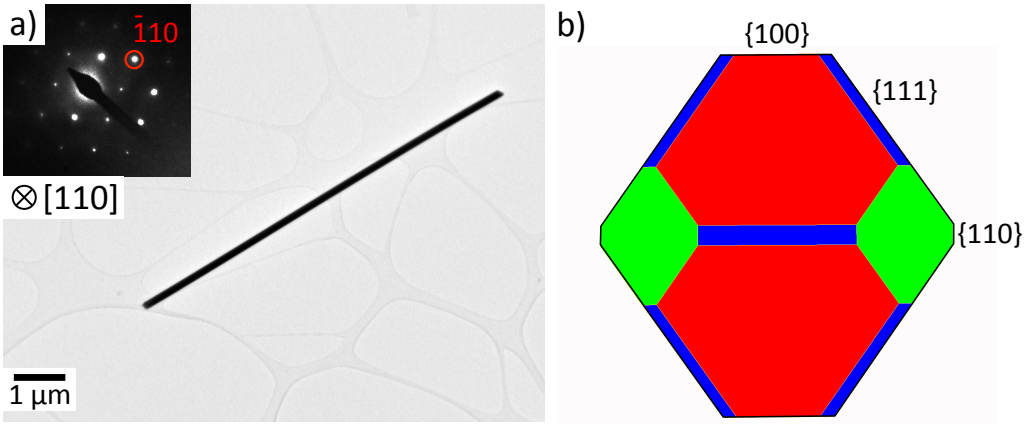


Figure 3.11 (a) TEM micrograph and (inset) corresponding diffraction pattern of a Ni whisker scratched from a Mo wire. The whisker axis is along the [110] direction. (b) Top-view of the Wulff construction of a Ni whisker. The surface planes are the {111} (red), {100} (green) and {110} (blue) crystal planes, respectively. The sidewalls of the Ni whisker are composed of 4 {111} planes and 2 {100} and 2 {110} planes.

Figure 3.11-b shows the top-view of the Wulff construction. The three families appearing as surface facets are low index crystal planes {111} (red), {100} (green) and {110} (blue) with their respective surface energies of $\gamma_{111} = 2.011$ J/m$^2$, $\gamma_{100} = 2.426$ J/m$^2$, $\gamma_{110} = 2.368$ J/m$^2$, as calculated by first principle calculation [171]. The octangu-

lar shape corresponds to the ideal cross-sectional area of the whisker (the top projection of the Wulff shape), which is confined by 4 {111}, 2 {100} and 2 {110} planes. The cross-sectional shape of the Ni whiskers (octangular) is different from that of the Cu whiskers (hexagonal). The {110} planes were absent in the latter case due to its relatively high surface energy compared to other crystal planes ({100}, {111}).

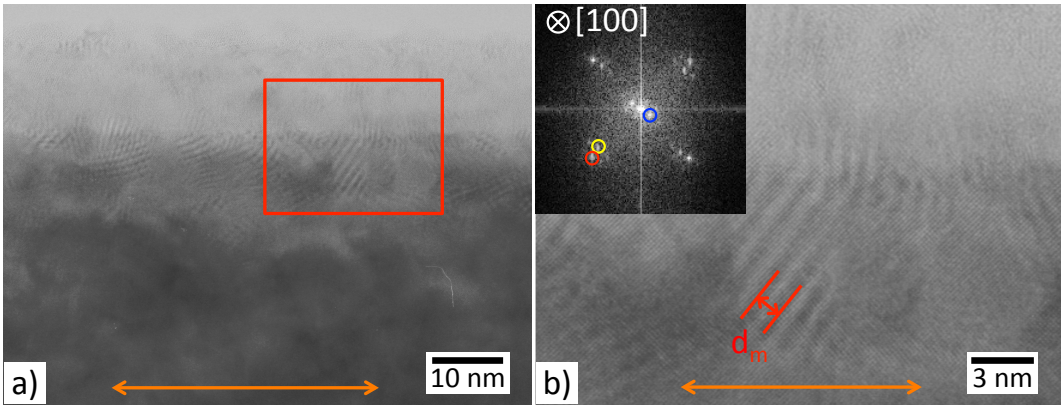


Figure 3.12 (a) HRTEM micrograph of a Ni whisker. The zoomed-in image of the area marked by the red rectangle is shown in (b). Moiré pattern was observed on both images. The orange lines denote [110], the axial direction of the whiskers.

An amorphous layer was observed sitting on top of a single crystal structure in the high-resolution TEM images shown in Figure 3.12. The single crystal structure is the core of the Ni whisker while the amorphous layer is the oxide, which was inevitably formed when the specimen was exposed to air. Some crystallized particles were found embedded in the amorphous matrix. The appearance of the moiré pattern also confirmed the existence of crystalized oxide on the whisker surface. The spacing of the moiré fringes, the interplanar distance of the Ni whisker core and of the crystallized oxide can be measured directly on the HR image or indirectly from the FFT (Figure 3.12-b inset). Three pattern sets were identified. The two spots (blue circle) close to the center (transmitted beam position) of the image were attributed to the moiré with the largest spacing. The other spots further away from the center are the FFT patterns of Ni (red circle) and of its oxide (yellow circle), respectively. The spacings measured on the HR image are consistent with those deduced from the FFT pattern. The spacing of the moiré fringes is $d_M = 1.125$ nm. The spacing of Ni whisker core is $d_B = 0.175$ nm (the subscript $_B$ denotes the base layer). The spacing of the oxide is $d_R = 0.208$ nm (the subscript $_R$ denotes the revealing layer). The spacing found for the moiré fringes agrees well with the value predicted by the well-known formula $d_M = d_B d_R/(d_R - d_B)$. The oxide layer on the Ni whiskers was identified as NiO with rock salt structure and a lattice constant of 0.415 nm. Its epitaxial relation with the single crystal Ni whisker core was further determined as $(001)_{NiO} // (001)_{Ni}$, $[100]_{NiO} // [100]_{Ni}$.

TEM investigations also revealed multiple occurrences of twin structures in the Ni whiskers. The most commonly found twin is Σ3 $(1\bar{1}1)[110]$, which is the lowest energy twin and is often found in FCC metals. A good example is shown in Figure 3.13 for the cross section of a Ni whisker prepared by FIB. The orientation of the diffraction pattern (Figure 3.13-b) has been readjusted so that it depicts the same sample orientation as the BF image (Figure 3.13-a). Two sets of diffraction pattern were identified and were marked with different colors. The DF image taken from the first set of diffraction spots (red frame) and that from the second set (green frame) are shown in Figure 3.13-c and -d, respectively. A grain was observed in each of the DF image. The two grains have mirrored but otherwise very similar shape. The twin boundary was found almost in the middle of the cross-sectional area, and was indexed as parallel to the {111} crystal plane. The above findings are clear indications of a Σ3 $(1\bar{1}1)[110]$ bicrystal.

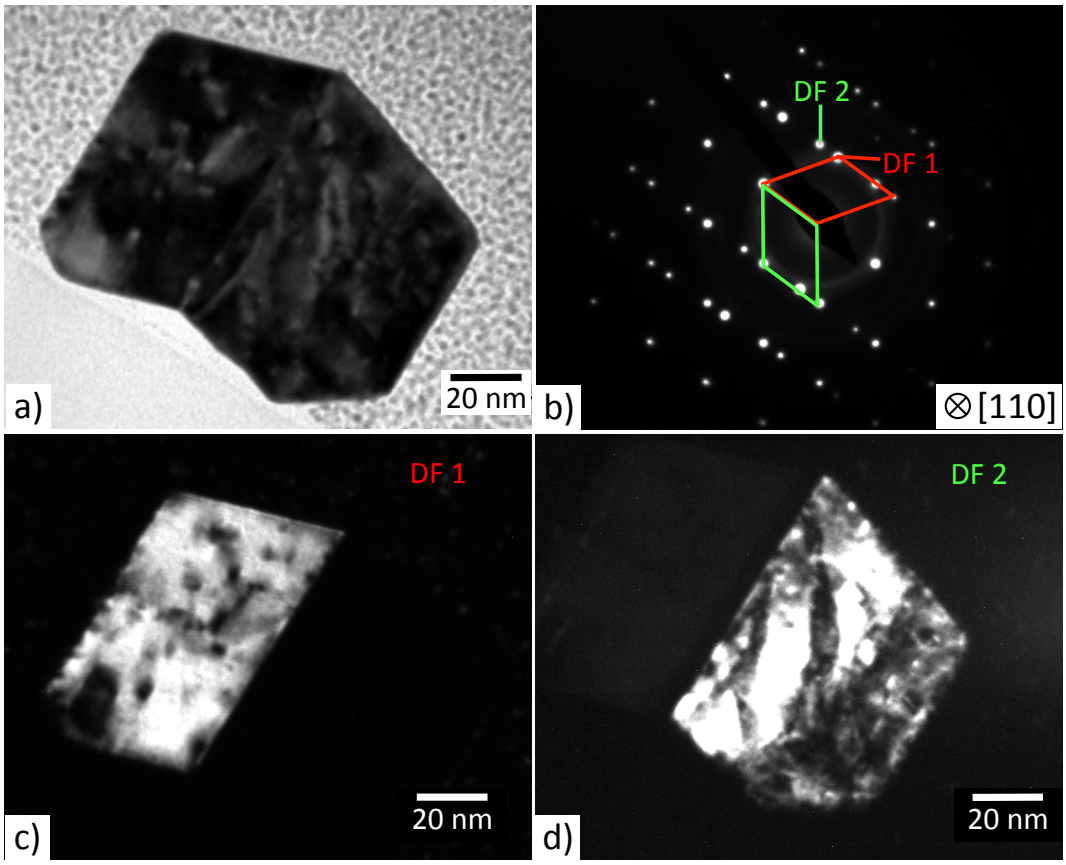


Figure 3.13 (a) TEM BF image and (b) the corresponding diffraction pattern of the cross section of a Ni whisker. A Σ3 $(1\bar{1}1)[110]$ twin structure was clearly observed in the dark field images (c, d) taken from different sets of diffraction spots in (b).

Single crystal Ni whiskers with no twin structure were also observed. Figure 3.14 -a and -b show the diffraction pattern and HR image of the cross section of such a whisker. The observed shape of the cross section is slightly different from the theoretical one (Wulff-shape, red frame). The shrunk {110} facets exhibited in addition a roughening

transition. The {100} facets were also much smaller than expected. These are due to an aberration of the actual surface energy ratios from the theoretical calculations, caused by the non-equilibrium growth condition. The same conclusion can be drawn for the whisker with the twin structure. (Figure 3.14-c) The {110} facets were also shrunk, although the {100} facets were slightly larger. The two grains depart from their theoretical shape in a similar way albeit in opposite directions (blue arrows), which is understood as the result of the inhomogeneous deposition on the tilted whisker. High-resolution TEM revealed defects near the edges and corners of both the single crystal (Figure 3.14-b) and the bi-crystal samples (Figure 3.14-d). The defects were recognized as a mixture of stacking faults and partial dislocations. Moreover, it appears that the twin boundary in the bi-crystal is not made of a perfect crystal plane, but one with steps. Stacking faults and partial dislocations were also observed in the vicinity of the twin boundary. Finally, it is worth pointing out that the defects may also originate from the (FIB) beam effect during sample preparation.

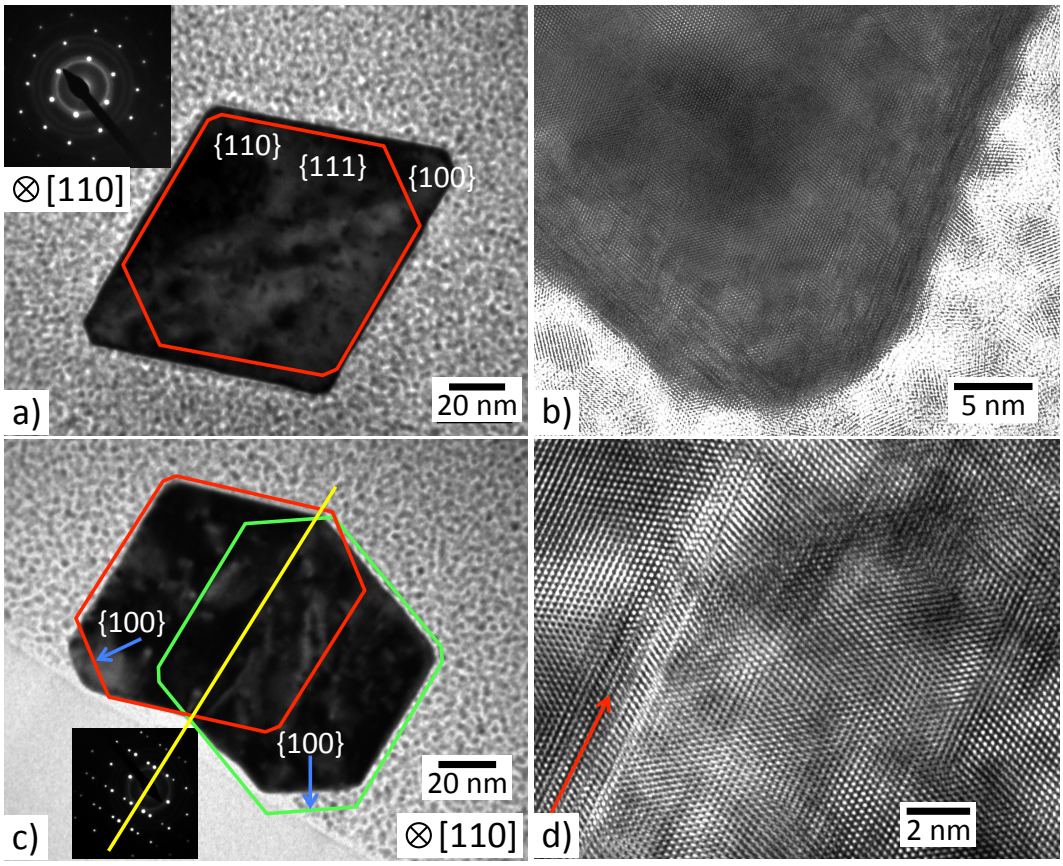


Figure 3.14 TEM micrographs and corresponding HRTEM images of Ni whisker cross sections cut by FIB. (a) and (b) are the same lamella from a single crystal whisker while (c) and (d) are the same lamella from a bicrystal whisker with a Σ3 $(1\bar{1}1)[110]$ boundary. The red and green frames are the equilibrium shape according to the Wulff construction. The yellow line marks the approximate location of the twin boundary.

## 3.2.2 Co

As mentioned earlier, phase transformation (from FCC to HCP, ~ 430 °C) is expected when cooling down the Co whiskers from their growth temperature (~ 760 °C) to RT for *ex situ* investigations. Depending on the temperature and the pressure, various cobalt oxides may be formed at different stages of the process [172,173], making the study of the transition process with Co whiskers even more difficult. Just like Ni whiskers, Co whiskers can be grown on Mo and W wires without any substrate preparations. The surface morphology after growth is also similar (Figure 3.15). On Mo wires, the surface was covered with a high density of Co objects (whiskers, blades, platelets and islands) whereas on W wires, only a few thin, long whiskers were observed. The structures of the Co whiskers grown on the two substrates were otherwise the same.

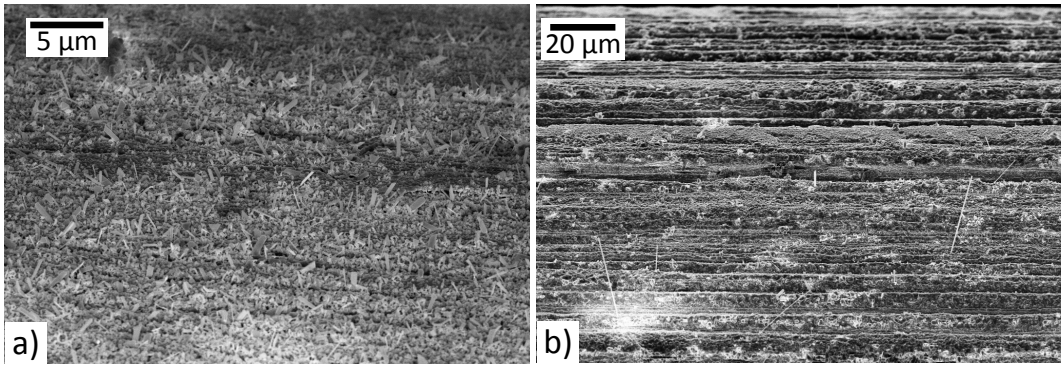


Figure 3.15 SEM micrographs of the surface of (a) a Mo and (b) a W wire after 180 nm (nominal value) of Co deposition at 760 °C. Various objects (whiskers, blades and platelets) were found on the Mo wire whereas on the W wire only a few long whiskers were observed.

Both HCP and FCC crystal structures were identified in the Co whiskers by electron diffraction. A Co whisker with FCC structure is shown in Figure 3.16-a. The whisker axis is along the <110> direction as deduced from the electron diffraction pattern (inset). Figure 3.16-b shows an HCP Co whisker from the [0001] zone axis. The axial direction of the whisker in this case is parallel to the <1210> direction. Twin structures were occasionally observed in both types of whiskers. High-resolution images indicate that the twin structures in FCC and in HCP whiskers are significantly different. In the case of a FCC whisker (Figure 3.16-c), it appears that the boundary of the two grains is parallel to the whisker axis. This, together with the diffraction patterns (inset) obtained on both sides of the grain boundary, evidenced the presence of a Σ3 $(1\bar{1}1)[110]$ twin relationship. Multiple stripes of contrast variations were detected near the twin boundary. These variations were reflective of the changes in crystal orientations due to microtwins. A possible explanation is that the orientation transition between the twin grains in the FCC Co whisker was originally achieved on a sharp crystal plane. The abrupt grain boundary then served as the preferential starting point for phase transformation (from

FCC to HCP) during sample cool-down. The incomplete transformation resulted in the formation of tiny HCP structures, which later became part of the observed microtwins. Stacking faults and partial dislocations (dark contrast in the image) were observed inside both twin grains and in the transition area. Their existence supported the theory of phase transformation taking place during the cool down procedure. Indeed, the Co phase transformation is a martensitic transformation that involves the formation of partial dislocations, and the stacking faults can be simply treated as the new HCP phase (Paragraph 1.4.2). In contrast, the twin grains described above were never observed in HCP whiskers. (Figure 3.16-d) Instead, microtwins were seen distributed homogeneously throughout the whisker with their twin planes parallel to the whisker axis. The phase transformation processes in the Co whiskers will be further discussed in details in chapter 4.1.

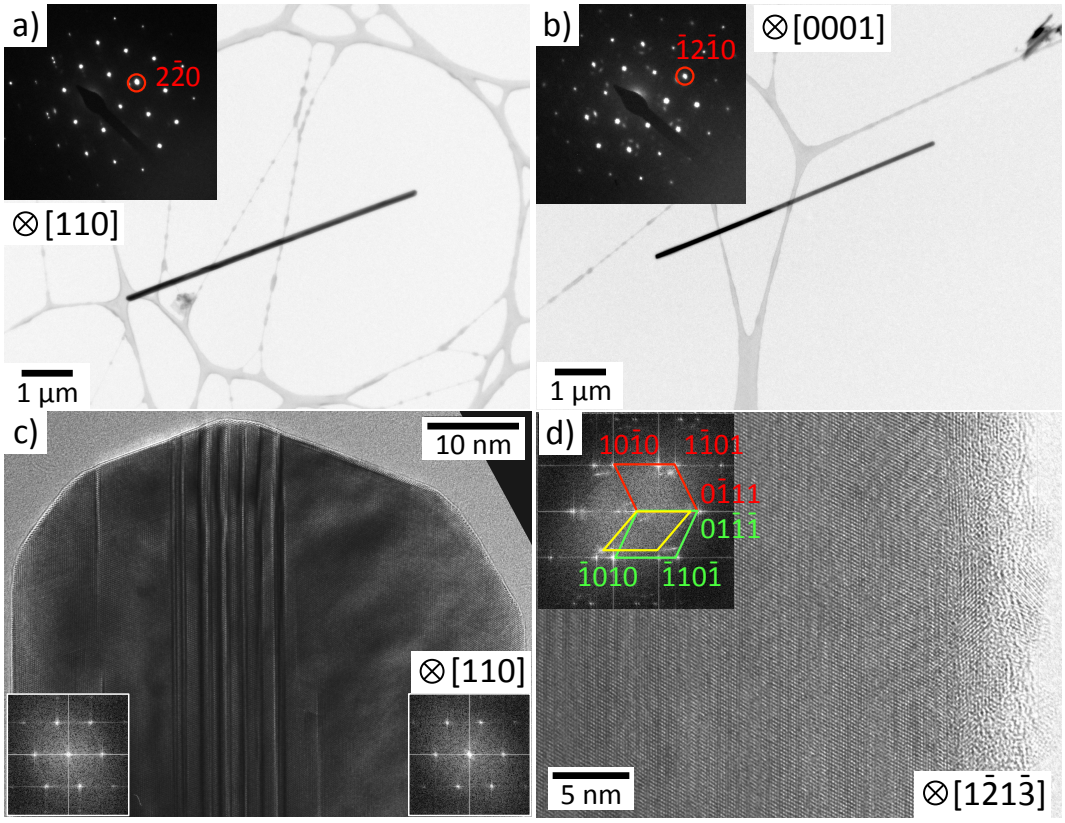


Figure 3.16 TEM micrograph and (inset) corresponding diffraction pattern of Co whiskers with a (a) FCC and a (b) HCP structure. (c) HRTEM micrograph of the tip of a FCC Co whisker with a Σ3 (1$\bar{1}$1)[110] bicrystal at 500 °C. The diffraction pattern on the left (right) is taken from the grain to the left (right) of the grain boundary. (d) HRTEM micrograph of a HCP Co whisker at RT and (inset) the corresponding FFT pattern.

From the high-resolution image in Figure 3.17, it appears that the surface of the Co whiskers was covered with an oxide layer. The oxide layer is mostly amorphous. Its crystallized part shows an epitaxial relation with the whisker core, which is evident

from the presence of the moiré fringes. Two sets of spots were observed on the calculated FFT pattern, those from the Co core (red circle) and those from the oxide (yellow circle), in addition to those belonging to the moiré (blue circle). The spacing of the moiré fringes was measured as $d_M = 1$ nm. The spacing of the red circle set was measured as $d_{red} = 0.175$ nm, which fits the interplanar distance of the FCC Co {200} crystal planes. The spacing of the yellow circle set was measured as $d_{yellow} = 0.212$ nm. The spacing found for the moiré fringes agrees well with the value predicted by $d_M = d_B d_R/(d_R - d_B)$. Here, $d_B = d_{red}$ is the interplanar distance of the base layer (whisker core) while $d_R = d_{yellow}$ is the interplanar distance of the revealing layer (surface oxide).

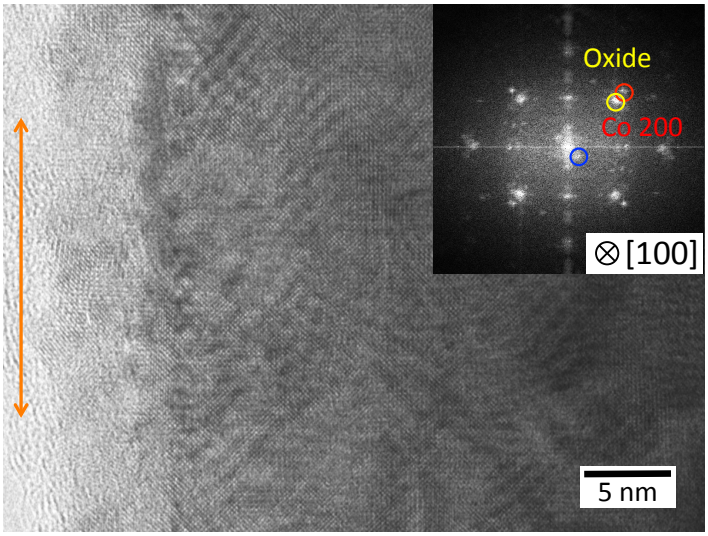


Figure 3.17 HRTEM image and (inset) the corresponding FFT pattern of a Co whisker from [100] zone axis. Three sets of patterns were observed on the FFT. The red circle is that of the FCC Co core. The yellow circle is that of the oxide layer covering the surface of the whisker. The blue circle is from the moiré. The orange line marks the axial direction of the whisker.

With the help of the diffraction pattern and the spacing $d_{yellow}$, it is possible to narrow down the composition of the layer to two of the cobalt oxides, CoO and $Co_3O_4$, both with cubic crystal structure. Both oxides have been reported on the Co whiskers [110,174]. CoO is stable at high temperatures. It has rock salt structure with a lattice constant of 0.422 nm. The interplanar distance of its {200} planes is hence 0.211 nm. $Co_3O_4$ is often found at room temperature. It has spinel structure with a lattice parameter of 0.812 nm. Its {400} planes thus have a spacing of 0.203 nm. Although the interplanar distance of CoO is closer to the measured spacing, the value for $Co_3O_4$ is still within the margin of error. Besides, the epitaxial oxide may be strained due to the lattice mismatch with the Co core, which could explain the deviation of the measured value from the theoretical one. On the other hand, even though $Co_3O_4$ is the more stable phase under ambient condition, the existence of CoO at RT cannot be ruled out due to

the geometrical peculiarity of the whiskers (high aspect ratio, high specific surface area). As a matter of fact, oxidation was reported to be different for Co thin films and Co nanoparticles than for bulk Co [172,175,176]. Therefore, the current data does not allow for the determination of the exact composition of the oxide surrounding the Co whiskers. It is nevertheless possible to derive from the FFT pattern the epitaxial relation between the oxide and the FCC Co core as $(001)_{oxide} // (001)_{Co}$ and $[100]_{oxide} // [100]_{Co}$.

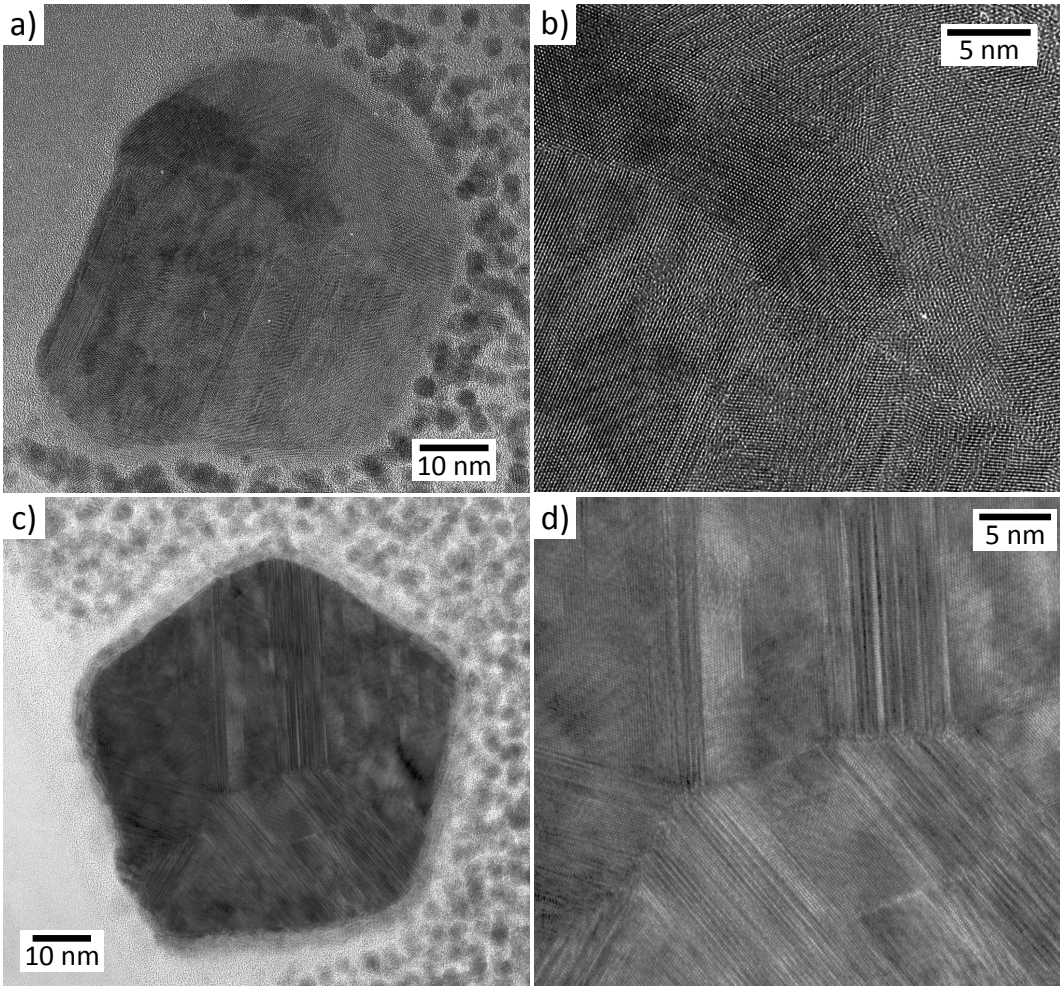


Figure 3.18 (a) TEM micrograph and (b) HR image of the cross section of a FCC Co whisker cut by FIB. (c) and (d) are from the cross section of another FCC Co whisker. There are multiple grains with in total 5 orientations in each of the cross section (c and d). Microtwins were found in all the transitional area where two grains of different orientations met, and inside some of the larger single crystal grains.

Figure 3.18 shows the HR images of two cross-sectional lamellae, taken from two different FCC Co whiskers. The cross-sectional view of the whisker structure is more complicated than expected. From the side-view (for instance the one in Figure 3.16-c), one would expect the cross section to be comprised of two twin grains, and in between them a transitional area of microtwins. However, both lamellae were shown to contain more than two grains. Although the shape of the two cross sections was different, the

microstructures found within them were comparable, each consisting of a number of twins and microtwins. With the presence of the microtwins, it is difficult to determine the exact number of grains in the lamellae. However, it would appear that there are in total 5 different grain orientations possible in the cross-sectional plane (that is, the one perpendicular to the whisker axis). Microtwins were found in all the transitional areas where two grains of different orientations formed a $\Sigma 3$ $(1\bar{1}1)[110]$ bicrystal, which is consistent with our previous speculations of grain boundaries being the preferred starting sites for phase transformation. Microtwins were also found in some of the larger grains without causing any changes in crystal orientations in their vicinity.

From the HR images, it seemed that the grain boundaries between two sets of microtwins were incoherent, as fluctuations of atomic positions were observed on both sides of the boundary. However, this does not indicate that coherent boundaries were not formed. Since HR images are 2D projection of the specimen over a finite thickness, it is possible that the observed incoherent grain boundaries were in fact coherent ones under a tilted perspective. Another intriguing point was that the cross-sectional area of the second sample (Figure 3.18-c) was a near perfect pentagon with an angle between adjacent sidewalls of about 70.5°. This is consistent with what was observed on some electro-deposition prepared FCC nanowires with a five-fold twin structure [177,178]. The pentagonal shape of the cross section is constructed mostly by the {100} planes with a small proportion by the {111} planes. This will be shown in more detailed analysis presented in section 4.1.

### 3.2.3 Fe

Fe whiskers were successfully synthesized on Mo foils at 800 °C by our group in 2012. One of those whiskers (referred to as 2012 samples) is shown in Figure 3.19. The whisker has a diameter of 60 nm and was covered by a 5 nm thick oxide layer, as is obvious from the material contrast observed in the TEM plane view image (Figure 3.19-a). The oxide layer was formed upon exposure to air when the specimen was removed from the UHV chamber. Much to our surprise, no further oxidation was observed even after prolonged exposure, especially since Fe is known to be extremely prone to oxidation under ambient conditions.

Figure 3.19-b shows a high-resolution image and corresponding FFT patterns of the same whisker. The whisker axis was along the [001] crystallographic direction. The nearest neighbor distance in inset-i was measured as 0.2 nm, which indicates that the whisker core was composed of BCC α-Fe. The FFT (inset-ii) of the heterojunction (transitional area) consists of patterns from two different crystal structures, one that comes from the BCC α-Fe core, and the other which can only be attributed to the crys-

tallized oxide layer. Further analysis linked the second pattern to a FCC structure with a lattice parameter of ~ 0.83 nm, which in turn suggested the oxide to be either $Fe_3O_4$ or $\gamma$-$Fe_2O_3$. Unfortunately, the two oxides are indistinguishable from microscopic analysis as they have very similar structure and lattice parameters.

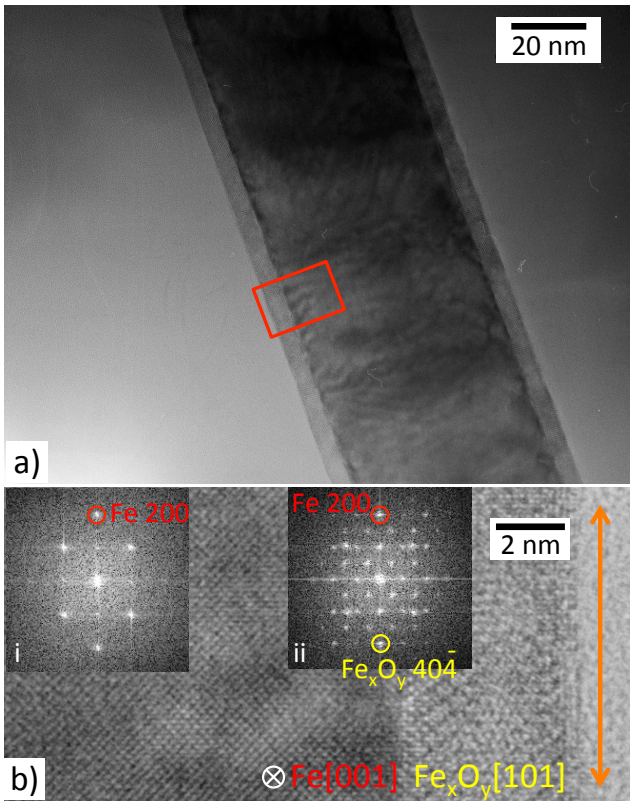


Figure 3.19 (a) TEM micrograph of a 60 nm thick Fe whisker with a 5 nm thick oxide layer from the 2012 samples. The HR micrograph of the region marked by the red rectangle is shown in (b). Inset-(i) and -(ii) are FFT pattern of the whisker core and of the Fe-oxide transitional area. The orange line marks the axial direction of the whisker.

Forbidden reflections were observed on both FTT patterns and were attributed to dynamic electron scattering by the layered structure (oxide – α-Fe – oxide). The existence of a layered structure is further supported by the presence of the moiré pattern at the whisker surface (Figure 3.19-a). The spacing of the moiré pattern was measured as 3.3 nm. This, together with the interplanar distance of the Fe whisker core $d_B = d_{Fe} =$ 0.143 nm, yielded an interplanar distance of the oxide of $d_R = d_{oxide} = 0.149$ nm. This result once again indicates the oxide layer to be either $Fe_3O_4$ or $\gamma$-$Fe_2O_3$. Finally, it is worth mentioning that the whiskers were free of defects and contaminations as was inferred from the high-resolution TEM micrograph in Figure 3.19-b.

Recently, Fe whiskers were also obtained on Mo and W wires as well as on STO ($SrTiO_3$) substrates with a mediating TiC layer. The growth temperature was about 760 °C for the Fe whiskers grown on Mo or W wires and about 810 °C for those grown

on STO substrates. The morphology of the objects after growth also depends on the type of the substrate. As shown in Figure 3.20, the Fe whiskers grown on the Mo wire resemble the Ni (Figure 3.10) and the Co (Figure 3.15) whiskers grown on the same substrate. The crystal orientation of the whiskers was fixed but their growth direction was completely random. This is in contrast to what was obtained on STO substrates where whiskers with two preferential growth directions were observed. Careful analysis revealed that the two growth directions were in fact perpendicular to one another. This can be understood as due to the 4-fold symmetry of the (001) (surface normal) STO substrate. Indeed, since the mediating TiC layer was mostly amorphous, the growth direction of the Fe whiskers can only be inherited from the underlying STO substrate. This implies that the mediating layer in this case merely provided the preferred nucleation sites (defects, possibly as vacancies or holes) for the whisker growth, and that an epitaxial relationship was possibly established between the Fe whiskers and the STO substrate.

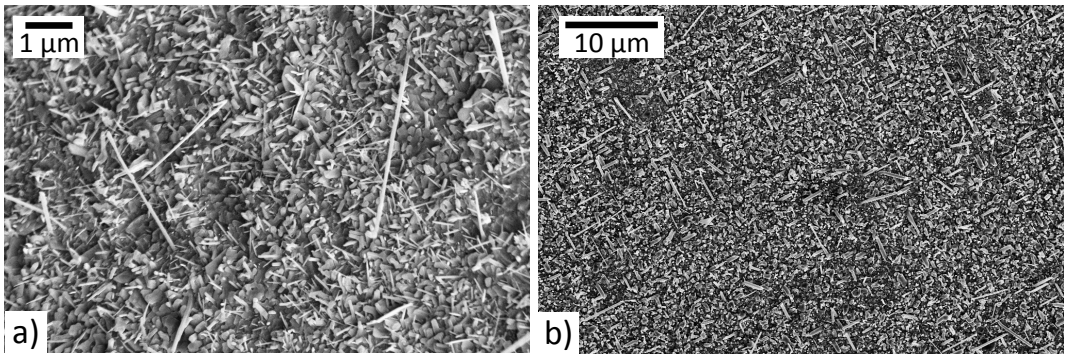


Figure 3.20 SEM micrographs of Fe whiskers grown on (a) Mo wire at 760 °C and on (b) STO substrate at 810 °C after 180 nm (nominal value) of Fe deposition. A TiC mediating layer was deposited on the surface of the STO substrates prior to the Fe deposition.

Microscopic analysis revealed that the Fe whiskers grown on Mo wires, on W wires and on STO substrates all shared the same crystallographic orientation as those previously grown on Mo foils (Figure 3.19). Figure 3.21 shows the HRTEM images of a Fe whisker obtained on a STO substrate. A 5 nm thick oxide layer was found covering the surface of the whisker, similar to what was observed on the 2012 samples. The oxide layer was mostly amorphous. The existence of some crystallized oxide can be inferred from the presence of the moiré fringes on the whisker surface. Three sets of spots can be recognized on the corresponding FFT pattern. The two spots close to the center (transmitted beam position) of the image were attributed to the moiré with the largest spacing. The other spots further away from the center are the FFT patterns of BCC Fe (whisker core) and its oxide, respectively. The spot distribution and the interplanar distance deduced from the FFT pattern indicate that the oxide was $Fe_3O_4$ or $\gamma$-$Fe_2O_3$ with a FCC structure. The FFT pattern also helped identify the whisker axis as parallel to the [100]

crystallographic direction. All these were consistent with the previous observations on the 2012 samples. In addition, sharp contrast variations were observed on the HRTEM image (marked by the red arrows), and were attributed to changes in the projected thickness of the cross section of the whiskers.

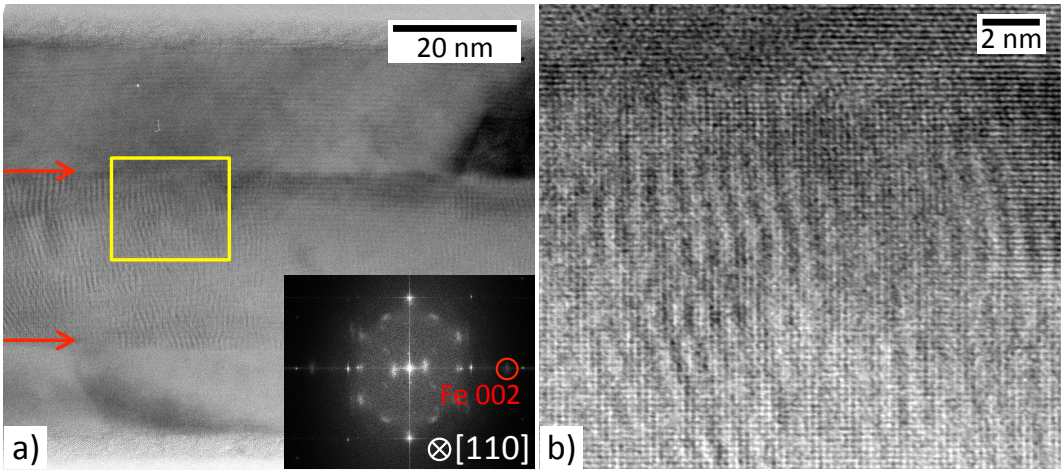


Figure 3.21 (a) High-resolution image of a Fe whisker grown on a STO substrate with a mediating TiC layer after 180 nm (nominal value) of deposition at 810 °C. Its corresponding FFT pattern is shown in the inset. The area marked by the yellow rectangle is shown in higher magnification in (b). The red arrows mark where sharp contrast was observed due to a variation in the projected thickness.

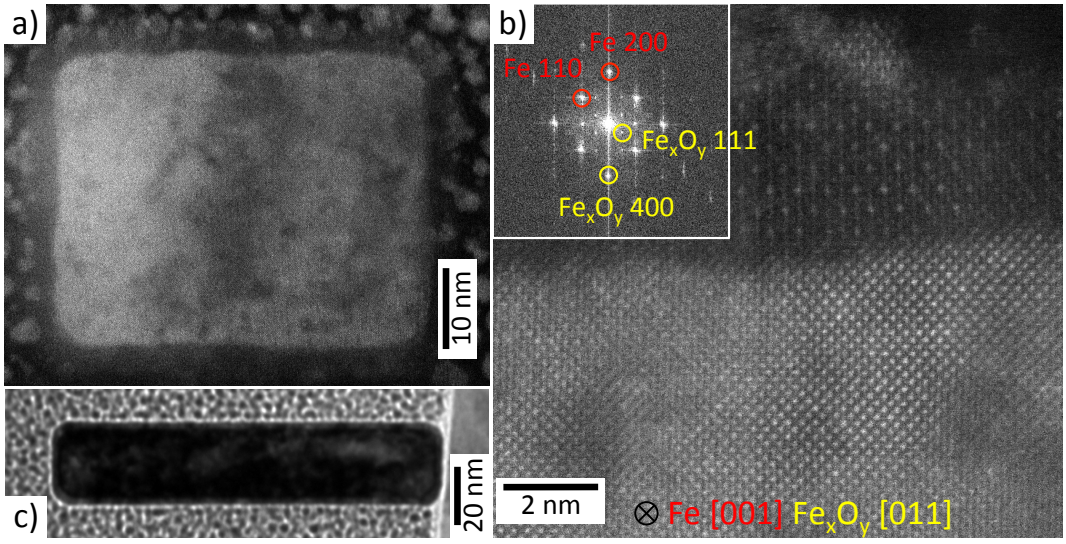


Figure 3.22 (a) STEM image on the cross section of a Fe whisker grown on a W wire, after 180 nm (nominal value) of Fe deposition at 760 °C. (b) HAADF image on the same cross section together with (inset) the corresponding FFT pattern. (c) TEM BF image on the cross section of another Fe whisker grown on the same substrate.

Further microscopic analysis on the cross-sectional lamellae (Figure 3.22-a and -c) indicated that the cross sections of the Fe whiskers were all rectangular shaped albeit

with different aspect ratios. The cross-sectional planes, cut with FIB, were perpendicular to the axial direction of the whiskers or the [100] crystallographic direction. A HAADF image on one of the lamella is shown in Figure 3.22-b. The Fe lattice and that of the oxide were clearly recognizable on the atomic resolved image. Two sets of spots were found in the corresponding FFT pattern (inset), one (red circles) corresponds to the (001) plane of BCC Fe and the other (yellow circles) corresponds to the (011) plane of FCC $Fe_3O_4$ or $\gamma$-$Fe_2O_3$. It can also be inferred from the FFT pattern that the sidewalls of the Fe whiskers were composed of 4 crystal planes of the {100} family. These are the planes with the lowest surface energy.

Finally, it is possible to derive the epitaxial relationship between the BCC Fe whisker and the FCC oxide layer by combining all the above data. The result, $(010)_{oxide} // (100)_{Fe}$ and $<011>_{oxide} // <100>_{Fe}$, is consistent with what was reported by Wagner [179] and Stockbridge [180] on large single crystals Fe at various temperatures, and by Luborsky [110] on sub-micron Fe whiskers.

## 3.2.4 Fe-Si

Similar to the growth of Cu-Si whiskers, interdiffusion takes place when depositing Fe onto a Si substrate. TiC was used in this case as the mediating layer. Silicide microstructures (whiskers, platelets and blades) were observed at the sample surface after Fe deposition at about 900 °C. As shown in Figure 3.23, the cross-sectional shape of the whiskers was close to a square, while that of the blades was an elongated rectangle (aspect ratio often higher than 5:1).

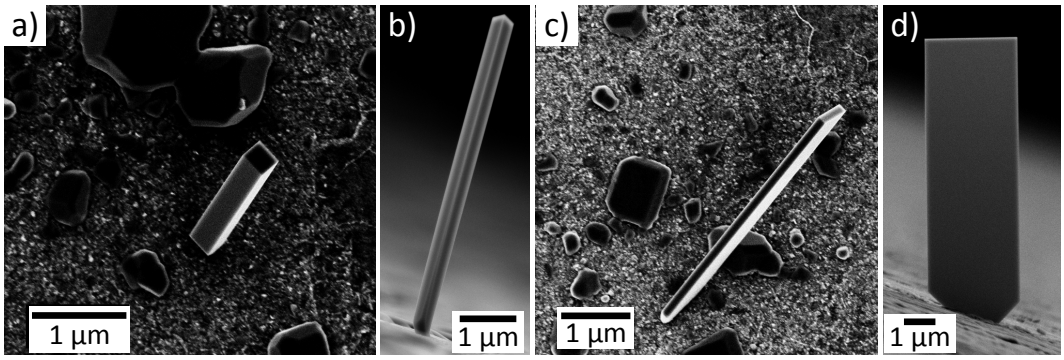


Figure 3.23 SEM micrographs of (a, b) 2 $FeSi_2$ whiskers and (c, d) 2 $FeSi_2$ blades after the deposition of 180 nm (nominal value) of Fe at 900 °C.

The Fe-Si binary alloy is a complex system consisting of numerous silicide phases (Figure 3.24). In order to determine the exact composition of the iron silicide whiskers, chemical analysis was carried out (Figure 3.25). EDX line scan seems to indicate an atomic ratio of Fe:Si = 1:3 inside the silicide whisker (Table 3.2-left), while atom probe

tomography (APT) contradicts the result with a measured ionic ratio of Fe:Si = 1:2 (Table 3.2-right). The discrepancy can be explained by an inhomogeneous chemical distribution related to oxidation as substantiated below, which may in turn cause a difference between the values measured near the surface (EDX) and in the whisker core (APT). Despite all that, the two chemical analyses suggested two possible silicide phases on the phase diagram: $FeSi_2$-l also known as α-$FeSi_2$ with $x_{Si} = 66.7\%$ and $FeSi_2$-h also known as β-$FeSi_2$ with $x_{Si} = 70\%$. The former is a metal with tetragonal structure while the latter is a semiconductor with orthorhombic structure [181].

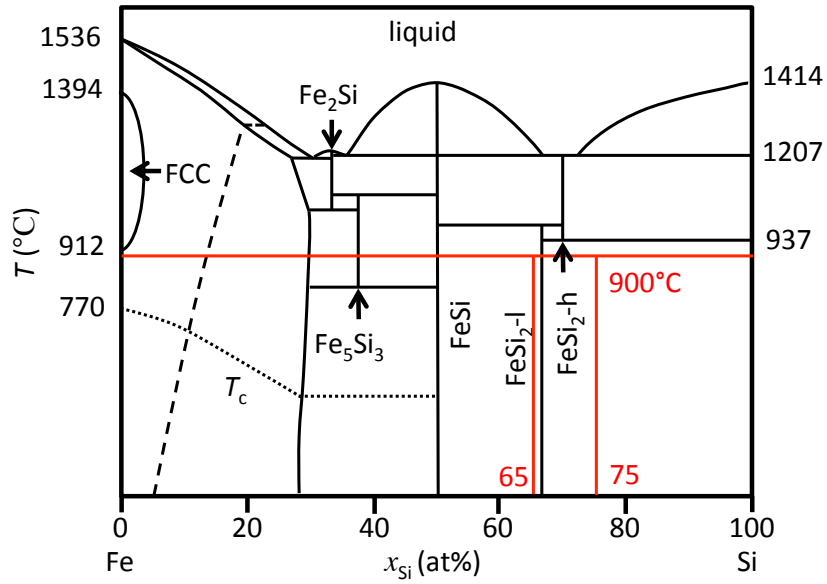


Figure 3.24 Calculated phase diagram for the Fe-Si binary system [181].

The composition and structure of the $FeSi_2$ alloy were further studied with electron diffraction. Figure 3.26-a and -b show the BF images of an iron silicide whisker. The corresponding diffraction patterns in the insets match that of α-$FeSi_2$ with tetragonal structure and lattice parameters of a = 0.269 nm, c = 0.513 nm. The contrast was homogeneous throughout the entire whisker for the BF image taken from zone axis [100]. For the BF image taken from zone axis [110], contrast fringes were observed in the direction parallel to the whisker axis. The fringes were symmetrical with respect to the central axis of the whisker. The above can be understood by taking into account the (almost) square shaped cross section of the whiskers observed in Figure 3.23-a. No contrast variation shall be observed when the incident beam is perpendicular to two of the four sides (Figure 3.26-c). On the other hand, if the incident beam was aligned with one of the diagonals (Figure 3.26-d), contrast variations would appear due to changes in the projected thickness of the whisker. This further implies that the sidewalls of the whiskers were composed of 4 planes of the {100} family.

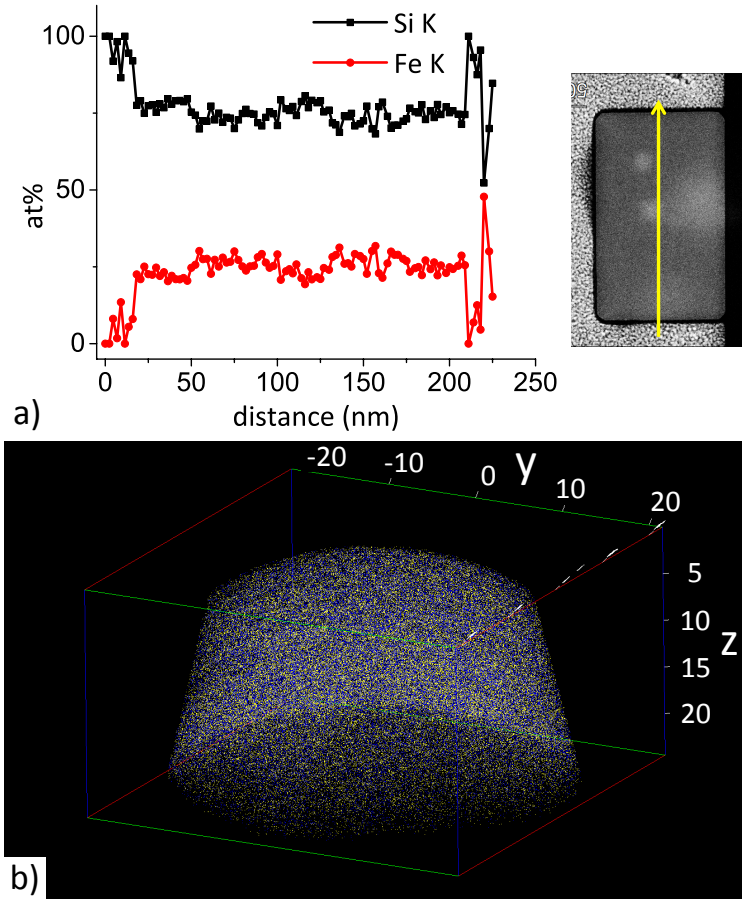


Figure 3.25 (a) Result of an EDX line scan running through the cross section of a $FeSi_2$ whisker. The scanning path is marked by the yellow arrow. (b) APT result on part of a $FeSi_2$ whisker.

Table 3.2 Results of EDX line scan (left) and APT (right) on $FeSi_2$ whiskers.

| EDX | avg. at% | STDEV | APT | counts | avg. at% |
|---|---|---|---|---|---|
| **Si** | 74.90 | 2.91 | **Si** | 308724 | 65.88% |
| **Fe** | 25.10 | 2.91 | **Fe** | 159150 | 33.96% |
| | | | **Ga** | 754 | 0.16% |

Extra facets (red lines) were sometimes observed near the root of the $FeSi_2$ whiskers (Figure 3.26-e). These facets only appeared at the junction between two adjacent {100} sidewalls, and were hence attributed to low index {110} planes for both thermodynamic and geometric considerations (Figure 3.26-d). Statistically, the extra facets were mostly observed on thicker and shorter whiskers. However, it is entirely possible that these small facets were also present on the whisker shown in Figure 3.26-a and -b, despite not being visible due to the peculiarity of the transmission technique. The appearance of the {110} planes at the root part of the whiskers, or to rephrase in a more correct way, the

disappearance of the {110} planes other than at the root part of the whiskers, is understood as of both thermodynamic and kinetic origins. The details of the growth process will be discussed in Chapter 5, but it is a well-known fact that the growth of the whiskers occurs in both the axial (along the whisker axis) and the radial (perpendicular to the whisker axis) directions, albeit one (axial) much faster than the other (radial). The radial growth of the whiskers was accomplished by the condensation and diffusion of Fe adatoms on the whisker sidewalls while the axial growth of the whisker was mostly attributed to the aggregation of Fe adatoms at the whisker-substrate interface, fueled by the atoms diffused from the substrate surface and from the whisker sidewalls. This is called the root growth mode of the whiskers. If proven true (to be debated in chapter 5), this could indicate that the axial growth of the whiskers, driven by the fast kinetic process, originally left behind a truncated square shaped cross section with large {100} and small {110} facets. The radial growth, a much slower thermodynamics process, then proceeded preferably along the <100> directions, which in turn resulted in the disappearance of the {110} facets except on the fresh grown part (root) of the whiskers.

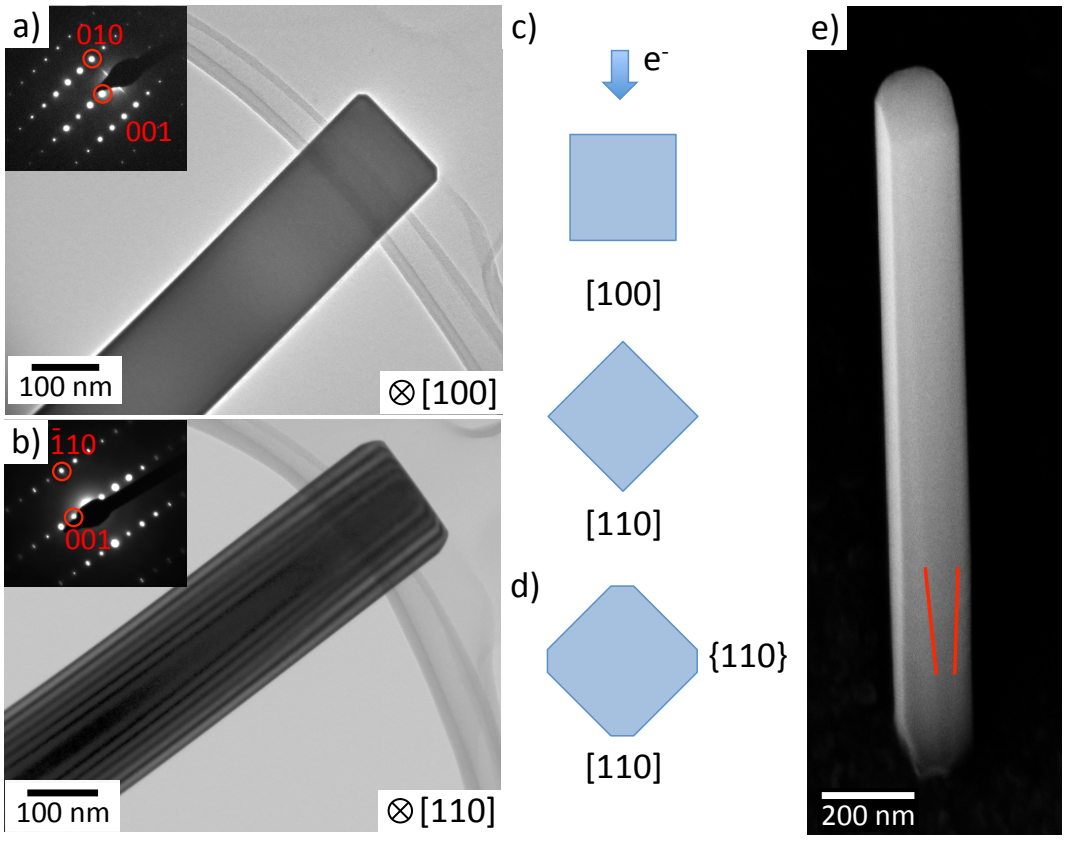


Figure 3.26 TEM BF micrographs of a $FeSi_2$ whisker from zone axes (a) [100] and (b) [110]. The insets are the corresponding diffraction patterns. (c) Schematic representation of the transmission geometry to obtain these two micrographs. (d) Schematic representation of the cross section of a $FeSi_2$ whisker with truncated facets. (e) SEM micrograph of a $FeSi_2$ whisker showing the transition of its cross-sectional area from octagon at the root to square at the tip.

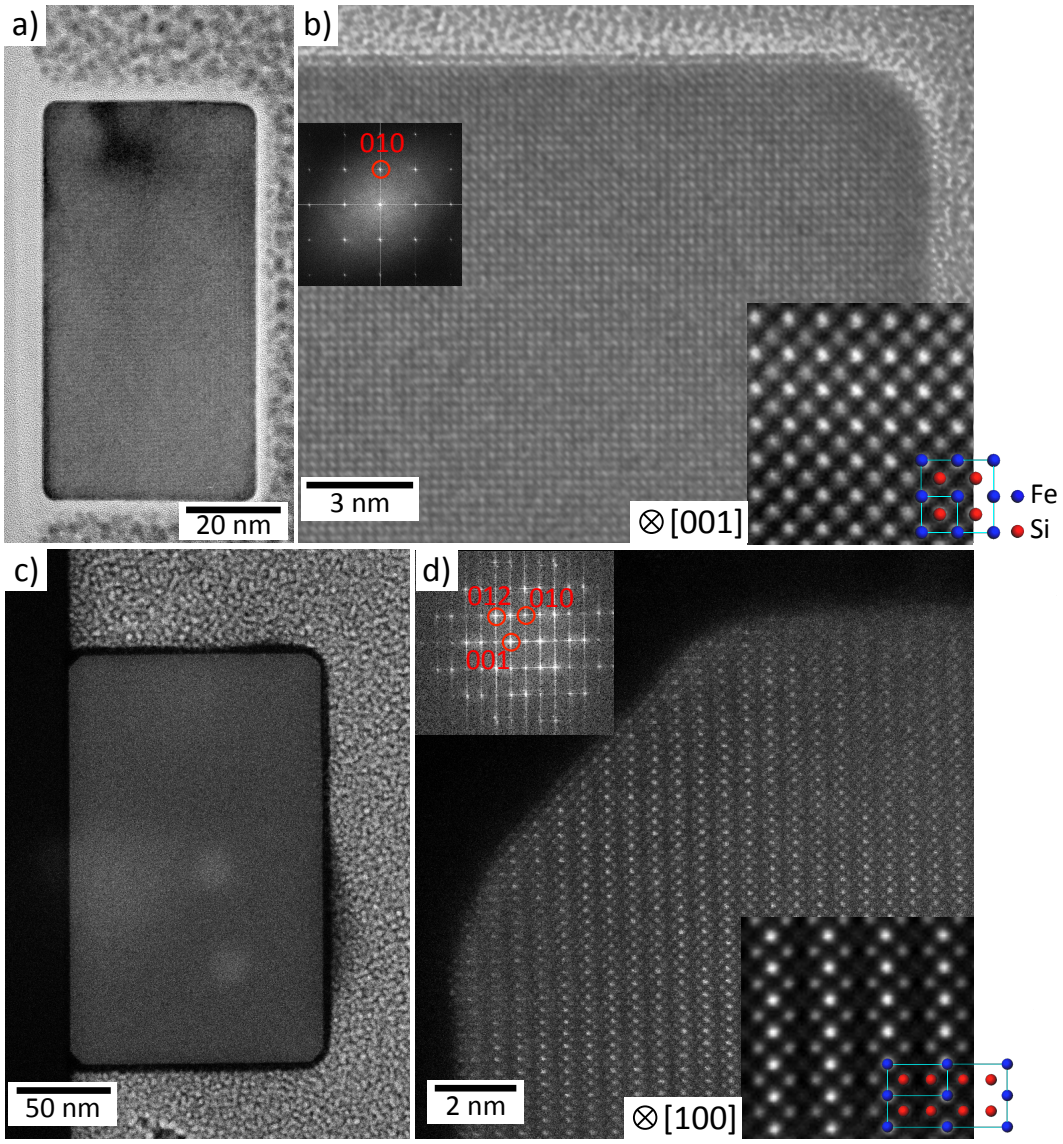


Figure 3.27 (a) TEM micrograph, (b) HR, HAADF image and (inset) the corresponding FFT pattern of the cross section of a $FeSi_2$ whisker grown along the [001] direction. (c) TEM micrograph, (d) HAADF images and (inset) the corresponding FFT pattern of the cross section of another $FeSi_2$ whisker grown along the [100] direction. A schematic of the α-$FeSi_2$ lattice is shown in the bottom-right corner of the HAADF images. The blue spheres are Fe atoms and the red ones are Si atoms.

Figure 3.27 shows the BF, HR and HAADF images of two cross-sectional lamellae cut from two different $FeSi_2$ whiskers. The two cross sections differ very much in size (50 × 90 $nm^2$ for the one shown in Figure 3.27-a and 140 × 220 $nm^2$ for the one in Figure 3.27-c), despite having a similar aspect ratio (1.8:1 and 1.6:1, respectively). Their crystallographic orientation was also very different. The FFT pattern of the first sample (Figure 3.27-b) indicates that the axial direction of the whisker (*i.e.,* the normal of the cross-sectional plane) was along the [001] direction and that its four sidewalls were all constructed with {100} planes. This is consistent with what we have previously ob-

served on the other sample (Figure 3.26). The FFT pattern of the second sample (Figure 3.27-b), however, was surprisingly different. The pattern fits well with what was expected from the [100] zone axis of tetragonal α-$FeSi_2$. The growth direction of the whisker in this case was the [100] direction with its sidewalls consisting of 2 {100} and 2 {001} planes.

The different atom arrangement in the two samples can also be observed on the HAADF images. A filter was applied to help better visualize the chemical contrast. The brighter spots are the heavier element which in this case are the Fe atoms. The two HAADF images agree well with the schematic atomic structure of α-$FeSi_2$ viewed from zone axis [001] and [100] respectively. Finally, the two whiskers also showed a difference on how adjacent sidewall facets were joined. A round edge was observed on the smaller cross section where two {100} facets met (Figure 3.27-b) whereas on the larger cross section (Figure 3.27-d) a small crystal plane, indexed as the {012} plane, was observed at the junction between the {100} and the {001} facet.

For comparison, a BF image of a $FeSi_2$ blade is shown in Figure 3.28. Its width is about 950 nm, much larger than the diameter of the whiskers. From the electron diffraction pattern (inset), the axial direction of the blade was identified as parallel to the [100] crystallographic direction. Its two largest surfaces are from the {001} family.

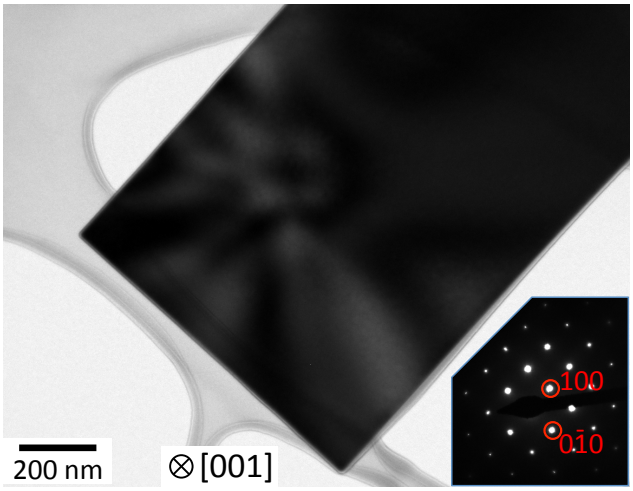


Figure 3.28 BF image and (inset) corresponding diffraction pattern of a $FeSi_2$ blade.

The chemical composition of the $FeSi_2$ whiskers was examined with EELS. The sample was the same as the one shown in Figure 3.27-c. The pathway of the EELS linescan on the cross section was marked by the yellow line in Figure 3.29-a. The background subtracted EELS spectra were summed separately for those measured on the crystallized core (red rectangle) and those on the amorphous shell (green rectangle). The result is shown in Figure 3.29-b and -c for the data near the Si edge and near the O/Fe edge, respectively. The fine structure details of Si-$L_{2,3}$ edges from core and shell appear dif-

ferent. The core has a single Si peak ($L_{2,3}$ edge) at 100.8 eV, while the shell has its Si-$L_{2,3}$ edge shifted to 105.5 eV followed by three other peaks at 107.8, 114.4 and 130 eV. The peak values and the fine structures of the two curves (core and shell) are in good agreement with what are expected from crystalline Si (99 eV) and from $SiO_2$ (106.3 eV), respectively [182,183]. The absence of the Fe peaks on the shell (green) curve indicates that the oxide layer at the surface of the $FeSi_2$ whiskers was mainly composed of $SiO_2$ with almost no oxides of iron. Indeed, the oxidation process of silicides usually proceeds by diffusion of the Si atoms towards the surface while the metal atoms remain in the bulk [184,185]. The formation of stable $SiO_2$ at the surface can easily prevent further oxidation of the whisker and the formation of oxides of iron. The different chemical composition observed in the shell and in the core region may be used to explain the discrepancy between the results obtained from EDX and APT. The APT probes mainly the core of the $FeSi_2$ whiskers and was able to obtain the correct ratio Fe:Si = 1:2. The EDX, on the other hand, is surface sensitive. It detects the $SiO_2$ layer, in addition to the $FeSi_2$ core, which increases the measured Si concentration up to Fe:Si = 1:3.

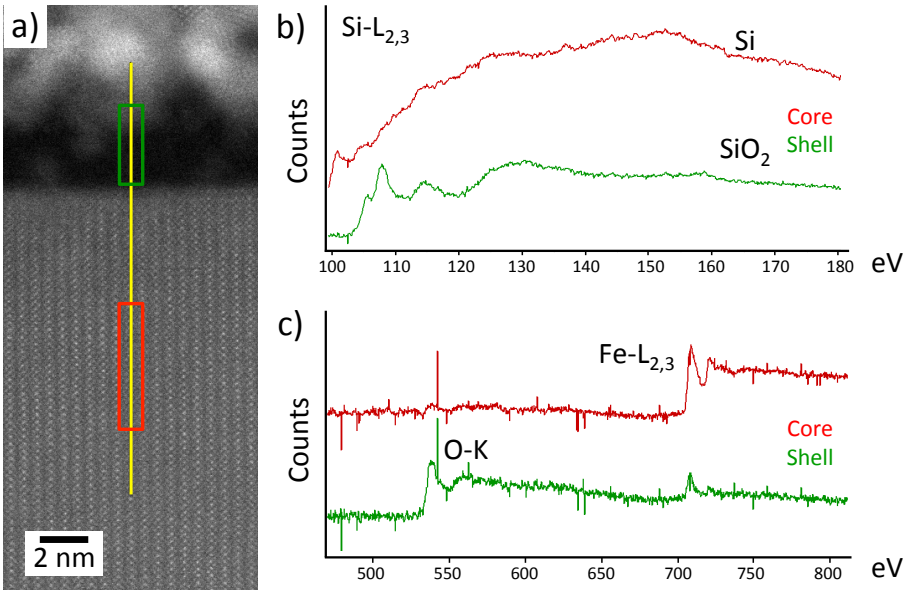


Figure 3.29 (a) EELS survey image. Background subtracted EELS spectra near (b) the Si edge and (c) near the O and Fe edges. The green (red) curve is the result summed on the area marked by the green (red) rectangle, for the shell (core) part of the structure.

## 3.3 Whisker Heterostructures

There are two fundamentally different microstructures that may evolve when growing whiskers with two different materials deposited in sequence. If the two materials are miscible, interdiffusion takes place which results in the formation of alloy whiskers. If, however the two materials are immiscible, whisker heterostructures are formed instead.

Both the alloy whiskers and the whisker heterostructures are appealing to the research community as they may bring forward new properties that are not native to either of the two components.

The experimental process of growing a whisker heterostructure is shown in Figure 3.30, taking Cu and Fe as an example. A certain amount of Cu was first deposited on the substrate. The substrate temperature was adjusted to fit in the growth window of the Cu whiskers. Subsequently, Fe was deposited. Atomic Fe can be condensed on both the substrate surface and the whisker sidewalls. There are three different sites for the Fe adatoms to then incorporate themselves into the Cu whiskers: the tip, the root and the sidewalls. The incorporation on the whisker sidewalls results in the expansion of the whisker diameter (radial growth) while that at the tip and/or at the root result in the elongation of the whisker (axial growth). For the past few decades, there has been a long debate over which is the major incorporation site for the axial growth of single-metal whiskers. In this section, we address this problem by studying the position of the second material in the whisker heterostructures.

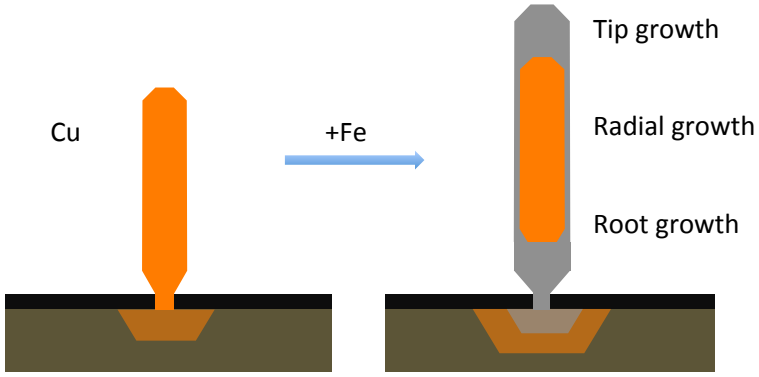


Figure 3.30 Schematic of the growth of a Cu-Fe whisker heterostructure.

## 3.3.1 Cu-Fe

The Cu-Fe system is considered a good starting point for the preparations of whisker heterostructures as the two metals are almost immiscible at 650 °C (Figure 3.31), which is the optimal growth temperature for Cu whiskers. The growth process was depicted in Figure 3.30, the Cu whisker was grown prior to the Fe deposition. The nominal film thickness was 90 nm for the deposition of both materials and the substrate temperature was fixed at 650 °C during the entire process. The morphology at the sample surface after growth varied, due to different wettability of the Cu and Fe atoms on the substrate. The best whisker heterostructures were obtained on an Au TEM grid with a C mediating layer. One of these whiskers is shown in Figure 3.32. A clear contrast was observed on the TEM BF image where the tip of the whisker appears to be much brighter than the bottom part.

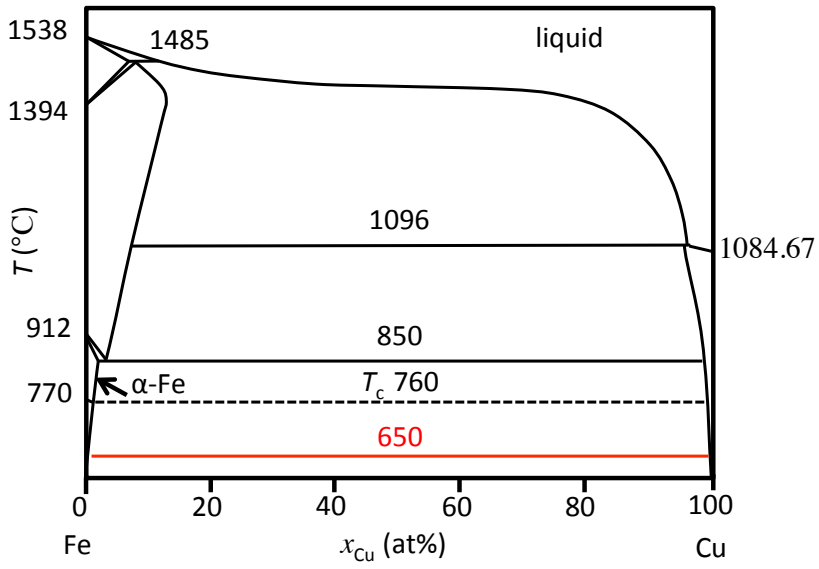


Figure 3.31 Calculated phase diagram for the Cu-Fe binary system [186].

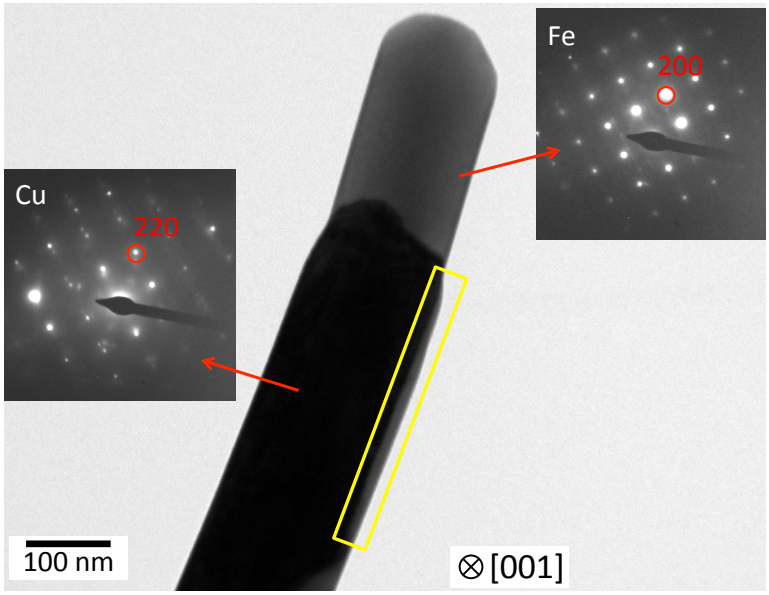


Figure 3.32 TEM micrograph of a Cu-Fe whisker heterostructure and (insets) diffraction patterns taken from different parts of the whisker.

Electron diffraction on the darker (bottom) part and on the brighter (tip) part of the whisker showed a similar pattern with different spacing. The former corresponds to a spacing of 0.129 nm, which coincides with the interplanar distance of the {220} planes of FCC Cu (0.128 nm). The latter corresponds to a spacing of 0.148 nm, which matches the interplanar distance of the {200} planes of BCC Fe (0.143 nm). The zone axis in both cases was along the [001] crystallographic direction. The whisker axis was further identified as parallel to the [200] direction for the Fe (tip, bright) part and parallel to the [110] direction for the Cu (bottom, dark) part. Moreover, a shell layer was observed on the surface of the Cu part of the whisker. The shell layer manifests itself as brighter

contrast (yellow rectangle) on the TEM BF image and as satellite spots on the diffraction pattern. This shell layer is most likely to be composed of Fe, which fits both the measured spacing (0.150 nm) and the speculation of radial growth taking place alongside the axial growth of the whiskers. The slight deviation from the theoretical value (0.143 nm, {200} planes, BCC Fe) may be strain related, due to the mismatch between the Fe and the Cu lattice. Indeed, the Fe thin film with a smaller lattice parameter is expected to be under tensile strain (*i.e.* with a larger measured spacing) when grown epitaxially on Cu whiskers.

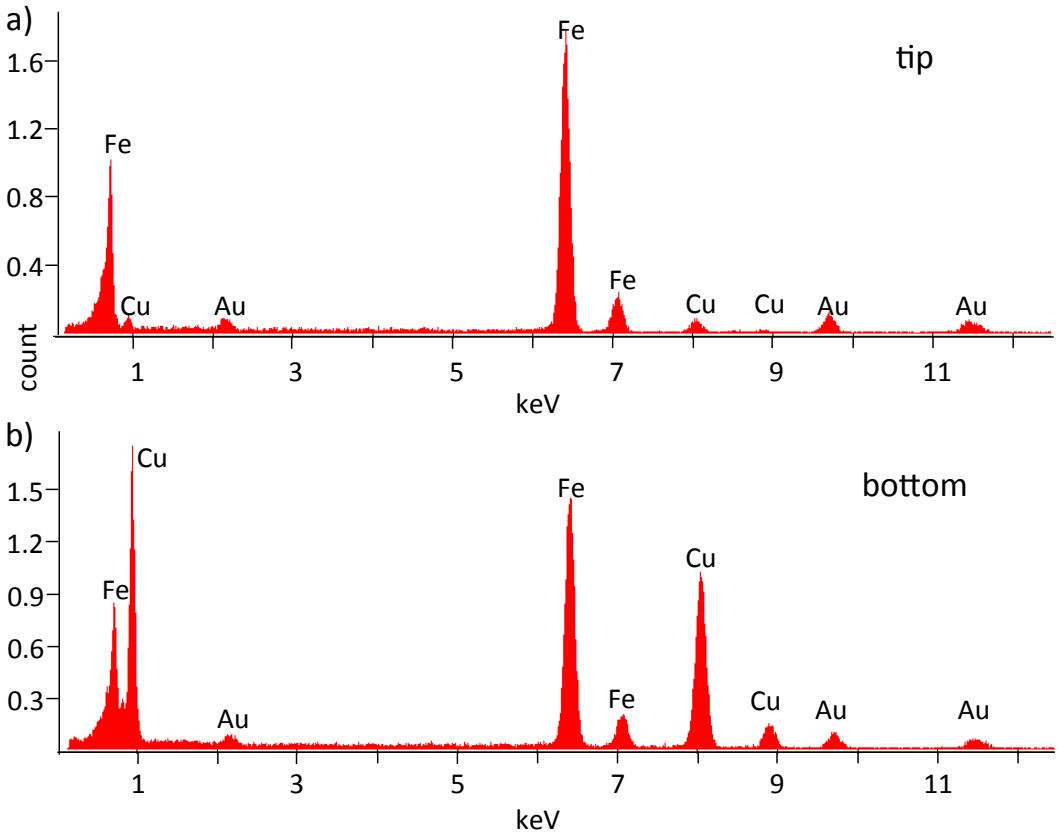


Figure 3.33 EDX spectra of the tip (a) and the bottom (b) part of the whisker heterostructure.

EDX spectra (Figure 3.33) collected from the tip and the bottom part of the whisker confirmed the existence of both the Cu-Fe radial (core-shell) and axial (bamboo) heterostructure. The observed Au peaks came from the TEM grid on which the whiskers were grown. The counts for the Au peaks are comparable on both spectra, indicating that the information obtained here can be considered reliable for semi-quantitative analysis. By comparing the two spectra, it is obvious that the Fe signal is slightly stronger on the tip than on the bottom, whereas the Cu peaks are much more pronounced on the bottom than on the tip. The stronger Fe signal from the tip is the direct measurement on the Fe part of the whisker heterostructure (due to axial growth) while the weaker one from the bottom is likely to be originated from the Fe shell layer (due to radial growth). This is consistent with the speculations based earlier on the diffraction

pattern. The tip of the whisker heterostructure consists of mostly Fe while the bottom part is the original Cu core surrounded by a thin Fe layer. It is worth mentioning that the weak Cu peaks in the first spectrum might not be reflective of actual Cu atoms detected in the tip. Instead, they may have come from the bottom part of the whisker convoluted by the limited resolution of the technique.

Regarding the growth of the second part (Fe part) of the whisker heterostructure, no root growth was observed on this sample. As a matter of fact, axial elongation during Fe deposition proceeded only at the tip of the Cu whisker. This seems to imply a tip-only growth mode in this case, which can be understood as due to the "blocking effect" of the C mediating layer. Indeed, while Cu whiskers can be synthesized when aided by a C layer, no Fe whiskers were ever obtained on a C mediated substrate. It would appear that the C layer is "blocking" the Fe segregation at the whisker-C interface (*i.e.* the root of the whisker heterostructure). The exact mechanism of the "blocking effect" is yet to be understood, but it is clear that the current observation cannot be explained by a mere reduction of the mobility of the Fe adatoms on C surfaces. Since the axial growth at the tip is most certainly fueled by the Fe adatoms deposited on the sidewalls of the heterostructure, one would expect the same growth to occur at the root even without the adatoms diffusing at the C surface.

### 3.3.2 Cu-Fe-Si

The Cu-Fe-Si whisker heterostructures were obtained by depositing sequentially 180 nm of Cu and 30 nm of Fe (nominal value) onto a Si substrate. The substrate temperature was kept at 700 °C during the entire process. Two segments with material contrast can be clearly observed on the SEM image (Figure 3.34-a), which confirms the presence of a heterostructure inside the whiskers. The tip (brighter) part appears much longer than the root (darker) part, and since the amount of Cu deposited greatly exceeds that of Fe, it is reasonable to assume that the root part of the whisker heterostructure was composed of mainly Fe, and that their growth proceeded via a root-growth mode (*i.e.,* later arrived materials are being incorporated at the root of the whiskers, at the whisker-substrate interface).

The mass-thickness contrast in the TEM images (Figure 3.34-b) also confirmed the existence of two different structures in the whiskers. Moreover, it would seem that (Figure 3.34-c) not only an axial (bamboo) but also a radial (core-shell) heterostructure was formed. Kinking was frequently observed at the axial heterojunction. The sidewall of the whisker heterostructure was covered additionally by a ~5 nm thick oxide layer. Finally, it is worth mentioning that heterostructures were also observed in the islands, as evidenced by the SEM images.

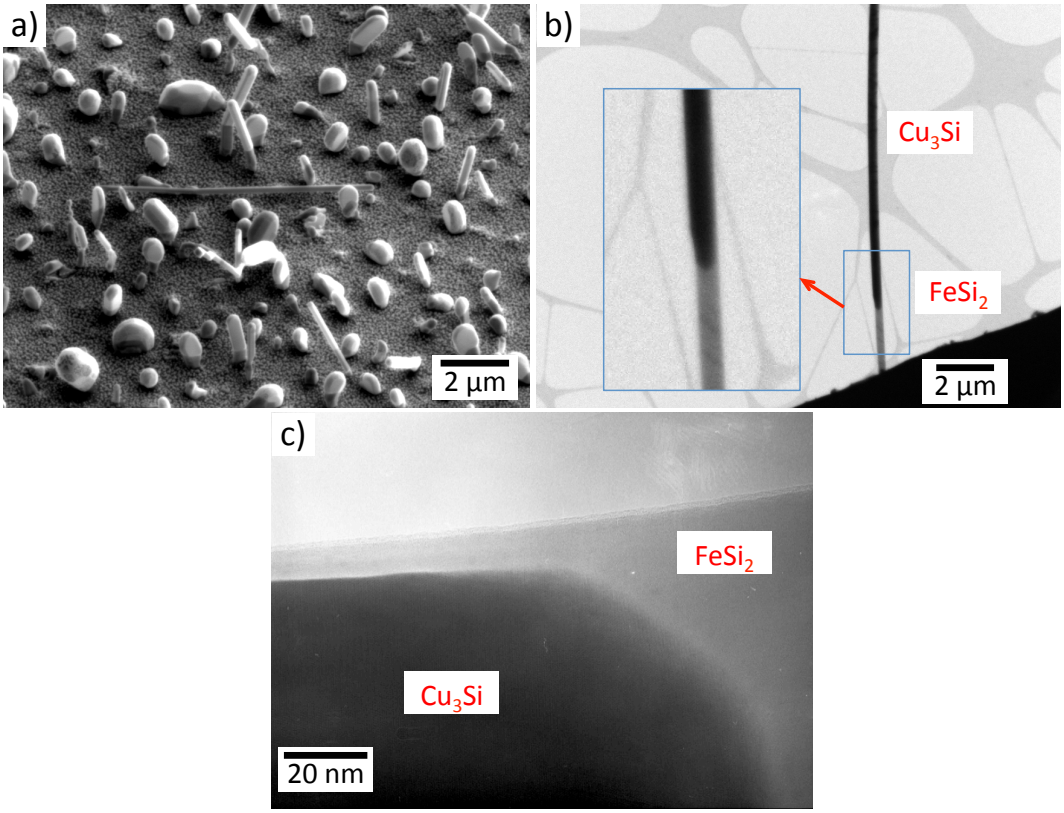


Figure 3.34 (a) SEM image showing the presence of two different segments within the Cu-Fe-Si whisker heterostructures with material contrast. (b) TEM BF image of a Cu-Fe-Si whisker heterostructure. (c) TEM image at the heterojunction showing that the Fe silicide forms not only an axial (bamboo) but also a radial (core-shell) heterostructure with the Cu silicide whisker.

It can be speculated from our previous experiments that Cu and Fe should form their respective silicide $Cu_3Si$ (Paragraph 3.1.2) and α-$FeSi_2$ (Paragraph 3.2.4) with the Si from the substrate. To verify this, cross section lamellae were taken with FIB from both the tip part and the root part of the whisker heterostructure. The result is shown in Figure 3.35. The diffraction pattern from the tip part agrees well with what was expected for HCP $Cu_3Si$. However, that from the root part does not match the diffraction pattern of tetragonal α-$FeSi_2$ at all. Instead, the arrangement of the diffraction spots as well as the measured spacing all suggested that the structure was in fact orthorhombic β-$FeSi_2$. The formation of a different iron silicide phase (β-, 700 °C) in the Cu-Fe-Si whisker heterostructures compared to that (α-, 900 °C) in the Fe-Si whiskers was attributed to the lower growth temperature. Indeed, the β phase is usually found at a lower temperature than the α phase as can be inferred from the phase diagram (Figure 3.24).

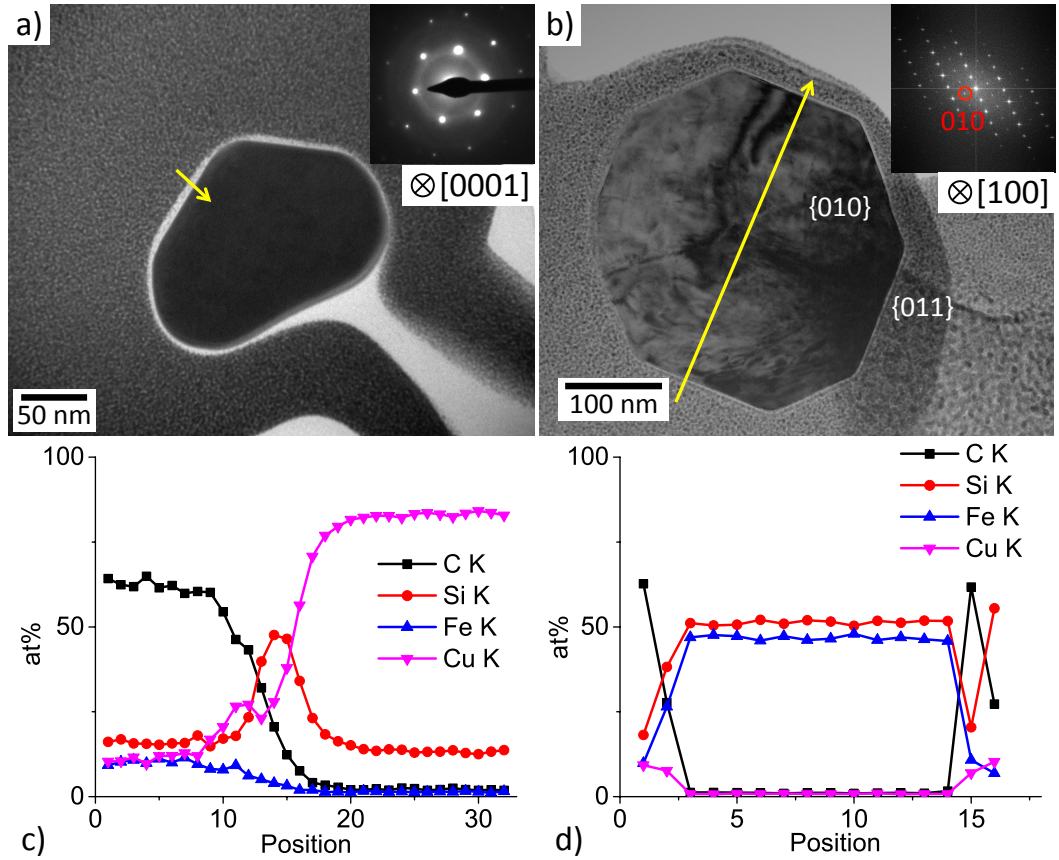


Figure 3.35 (a) Cross-sectional view and (inset) diffraction pattern of the tip part of a Cu-Fe-Si whisker heterostructure. (b) Cross-sectional view and (inset) diffraction pattern of the bottom part of another Cu-Fe-Si whisker heterostructure. (c) Result of an EDX line-scan, the scanning path is indicated by the yellow arrow in (a). (d) Result of another EDX line-scan, the scanning path is indicated by the yellow arrow in (b).

While the cross-sectional shape of the tip ($Cu_3Si$) part did not exhibit a high level of symmetry, that of the root (β-$FeSi_2$) part revealed itself to be a nice octagon. The corresponding diffraction patterns indicate that the whisker axis was along the [0001] direction for the $Cu_3Si$ part. This is consistent with what was found in pure $Cu_3Si$ whiskers. As for the $FeSi_2$ part, the whisker axis was found to be parallel to the [100] direction. Figure 3.35-c and -d show the results of EDX on the two lamellae. The tip part of the whisker heterostructure was composed of mainly Cu (82.9 at%), plus 13.5 at% Si and 1.4 at% Fe, while the root part consists of approximately 51.3 at% Fe, 46.7 at% Si with less than 1 at% Cu. Although EDX was unable to detect the existence of a Fe silicide shell surrounding the Cu silicide core due to its low resolution, the acquired information was more than sufficient for us to establish the growth process of the Cu-Fe-Si whisker heterostructure. The growth process followed the root growth mechanism, *i.e.* subsequently deposited materials diffused on the substrate surface before being incorporated at the root of the whiskers, at the whisker-substrate interface. This process gradually "pushed up" the existing structure, resulting in the elongation or axial growth of the

whisker heterostructure. Radial (lateral) growth also took place but was less prominent. Whether the radial growth was fueled entirely by the atoms deposited directly on the sidewalls or was there a part that comes from the adatoms diffused from the substrate surface remains to be studied. The O concentration was constant throughout the whisker, indicating the presence of a rather uniform surface oxide layer. There may be multiple origins of the detected C signal, such as sample contaminations, the TEM chamber and the detector.

### 3.3.3 Cu-Ni

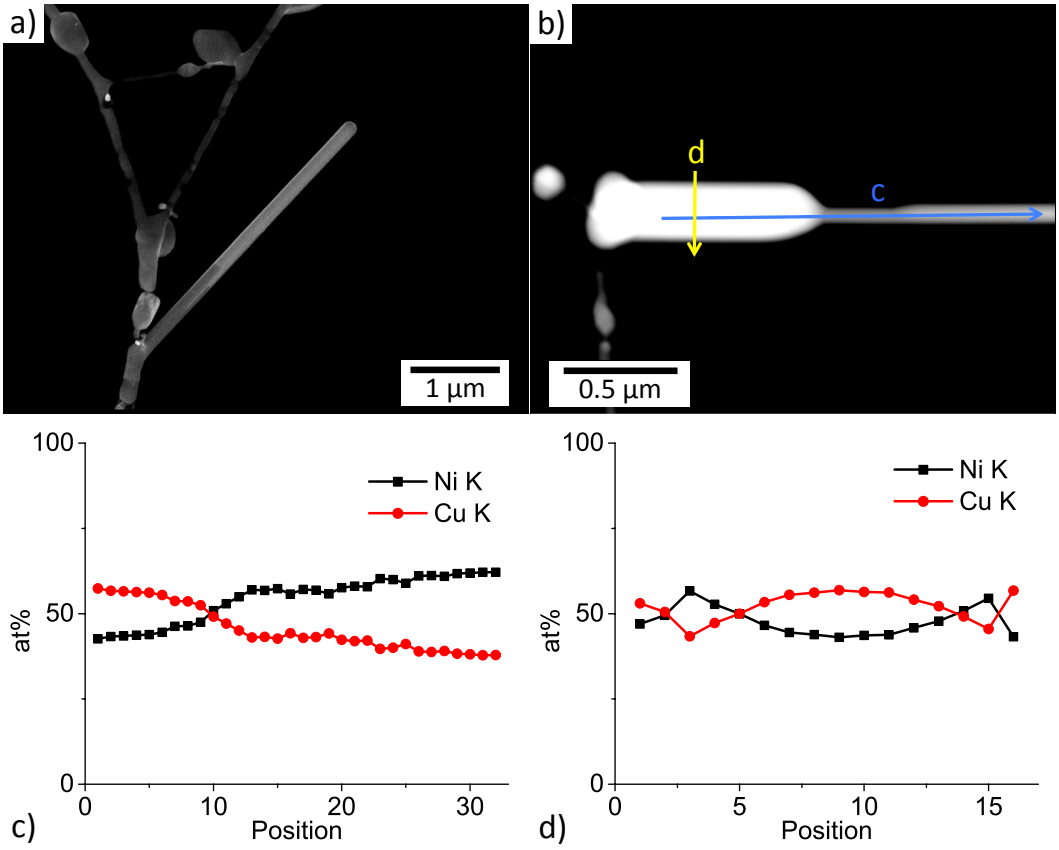


Figure 3.36 (a) SEM image and (b) HAADF image of two Cu-Ni whisker heterostructures. The material contrast between the root and the tip part was observed. (c) and (d) are the EDX line scan results. Their respective scanning path is marked by the blue and the yellow arrow in (b).

Miscibility gaps can also be found in the Cu-Ni binary system. Therefore, it is theoretically possible to prepare whisker heterostructures with these two materials. The growth temperature was chosen as 650 °C. It is the temperature where Cu and Ni do not mix while still within the overlapped region of the temperature window for the whisker growth of each material. Figure 3.36-a shows a Cu-Ni whisker heterostructure obtained on a Au TEM grid after the deposition of 90 nm Cu and 90 nm Ni (nominal value, in sequence). The whisker is straight with a constant diameter. Its tip part appeared

brighter on the image than its root part. Figure 3.36-b shows another Cu-Ni whisker heterostructure from the same Au grid with a root part this time much thicker than the tip part. It can be inferred from the EDX line scan results that while both Cu and Ni were constantly detected in the entire whisker heterostructure, (Figure 3.36-c) the root was richer in Cu than the tip. This implies that the growth followed a tip-growth mechanism (*i.e.,* Ni were mainly incorporated at the tip of the whisker, resulting in a higher Cu concentration near the root). However, the above interpretation should be treated with caution, since the higher Cu concentration can also be due to radial-only growth of Ni on a Cu whisker with initially a thicker root. Finally, a core-shell structure was identified in the linescan running across the root part of the whisker heterostructure (Figure 3.36-d). It would seem that the outer layer of the root contained a slightly larger amount of Ni than the center.

## 3.3.4 Cu-Ni-Si

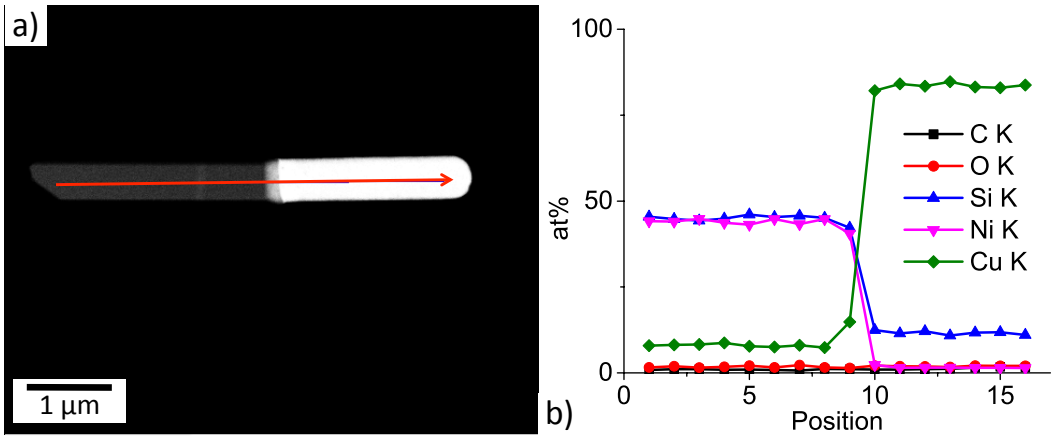


Figure 3.37 (a) HAADF image of a Cu-Ni-Si whisker heterostructure. (b) Result of the EDX line-scan. The red arrow in (a) indicates the scanning path.

A sharper material contrast was observed when growing Cu-Ni whisker heterostructures on Si substrates. The substrate temperature was fixed at 650 °C for the entire process. The nominal thickness was 90 nm for both the initial Cu and the subsequent Ni deposition. A darker root part (brighter tip part) was observed on the HAADF image shown in Figure 3.37-a. EDX line-scan along the whisker axis revealed the existence of a rather abrupt heterojunction (Figure 3.37-b). The root part was composed of about 8.0 at% Cu, 45.2 at% Si and 44.1 at% Ni. The chemical ratios Ni:Si ~ 1 and Ni:Cu > 1 are similar to what were found in the root part ($FeSi_2$ part) of the Cu-Fe-Si whisker heterostructures with Fe:Si ~ 1 and Fe:Cu >> 1. The tip part was made of 83.5% Cu, 11.6% Si and 2% Ni, which is also consistent with the composition of the tip part ($Cu_3Si$ part) of the Cu-Fe-Si whisker heterostructures. This implies that the growth of Cu-Ni-Si whisker heterostructures on Si substrates follows the same route as the growth of Cu-Fe-Si whisker

heterostructures. The major incorporation site was the root (root growth mechanism), and the two materials Cu and Ni each formed their respective silicide with Si from the substrate. The oxygen concentration and the carbon concentration were more or less constant throughout the whisker. The former suggests the presence of a rather uniform surface oxide layer. Like before, there may be multiple origins of the detected C signal. It could come from sample contaminations, the TEM chamber and/or the detector.

### 3.3.5 Au-Ni

Au-Ni whisker heterostructures have been successfully synthesized on W wires after a deposition (nominal value) of 90 nm Au and 90 nm Ni (in sequence) at 760 °C. One of them is shown in Figure 3.38. Three zones with different material contrast were identified on the TEM BF image. Electron diffraction on each zone shows the same FCC structure (viewed from the [110] zone axis) albeit with different lattice parameters. The ones from zone A and C correspond to the Ni structure with $a_{Ni} = 0.352$ nm while the one from zone B matches the Au structure with $a_{Au} = 0.408$ nm. The orientations of the three diffraction patterns were otherwise the same, indicating that the whisker axis was along the <110> crystallographic direction for both the Au (darker, zone B) and the Ni (brighter, zone A and C) part.

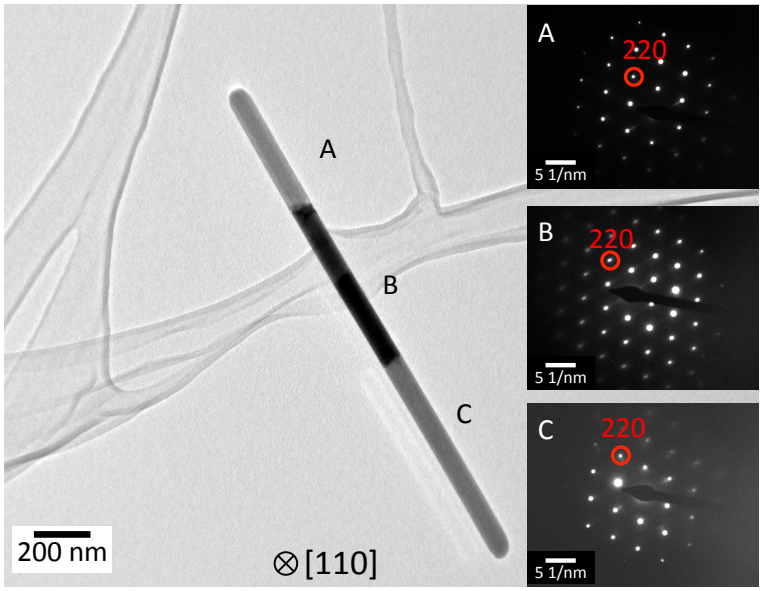


Figure 3.38 TEM BF image of a Au-Ni whisker heterostructure. The diffraction patterns on the right were taken from zone A, B and C respectively while maintaining the same incident angle of the electron beam.

EDX line-scan across the heterojunction of another Au-Ni whisker heterostructure (Figure 3.39-b) shows a switch in chemical composition from 95.03% Au and 4.96% Ni in the brighter zone to 39.88% Au and 60.11% Ni in the darker one. This is further confirmed by the line-scans running separately through each zone. The Au (Ni) concen-

tration was found to be 95.44% (4.55%) in the center of the brighter zone (Figure 3.39-c) and 42.43% (57.56%) in the center of the darker one (Figure 3.39-d). These values are consistent with the result of the first EDX scan (Figure 3.39-b). Moreover, it seems that only Au was detected near the two extremities of the scans (brighter and darker zone). This indicates the presence of a pure Au shell covering the surface of the sidewalls of the entire whisker heterostructures.

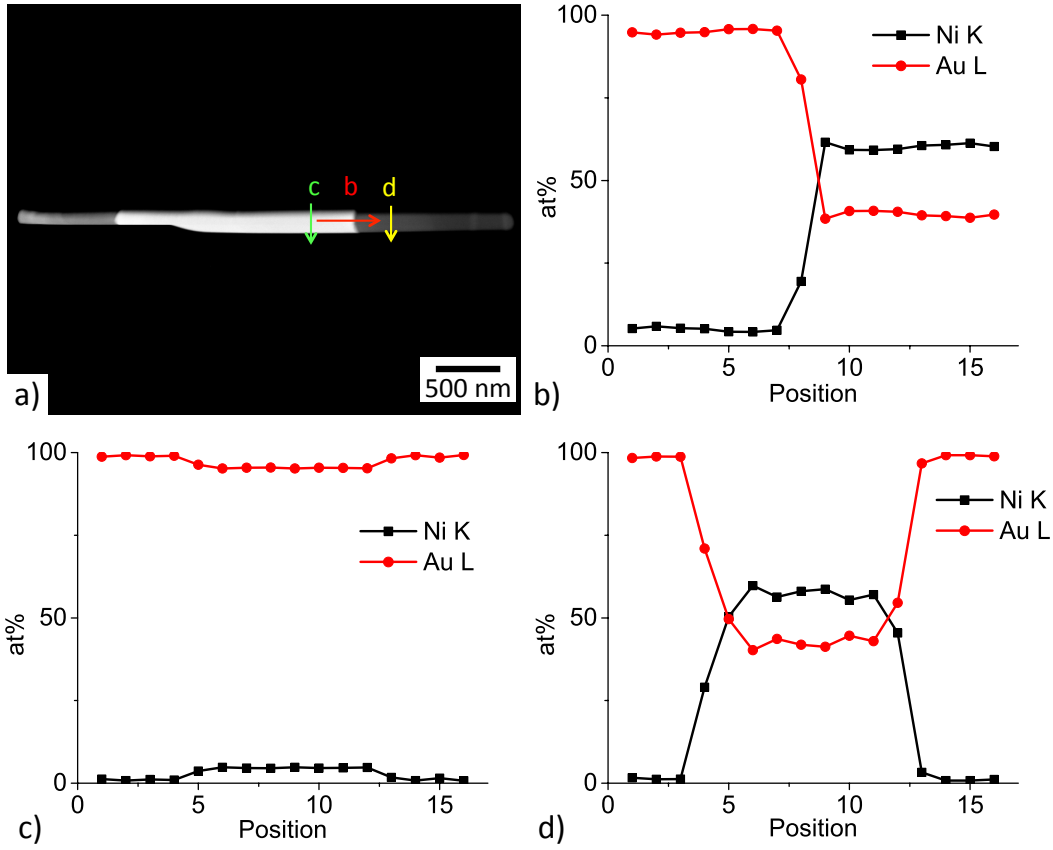


Figure 3.39 (a) HAADF image and (b), (c), (d) EDX line scan results on a Au-Ni whisker heterostructure. Their paths are marked by the red, green, yellow arrows respectively.

The entire growth process of the Au-Ni whisker heterostructure is speculated as follows. Axial elongation during Ni deposition proceeded simultaneously at the tip and at the root of the Au whiskers as both of them turned out to be the active sites for the incorporation of Ni atoms (tip plus root growth mechanism). In the meantime, there was a substantial amount of intermixing between Ni and Au at the temperature of growth (760 °C, 1033K) as can be inferred from the phase diagram (Figure 3.40). As a result, the more mobile Au atoms were constantly diffusing into the newly grown Ni segments, while the originally formed Au segment remained relatively intact except for a thin surface layer formed by the Ni atoms deposited directly on the whisker sidewall. The miscibility then declined when the sample was cooled, forcing the alloy to separate. In the process, the Au atoms, having a lower surface energy [187], diffused towards the

surface, forming the pure Au shell that covers the sidewalls of the entire whisker heterostructures. It is worth mentioning that the Au shell should theoretically be capable of protecting the Ni segments from being oxidized, which may prove interesting, as the Ni whiskers themselves are fairly prone to oxidation.

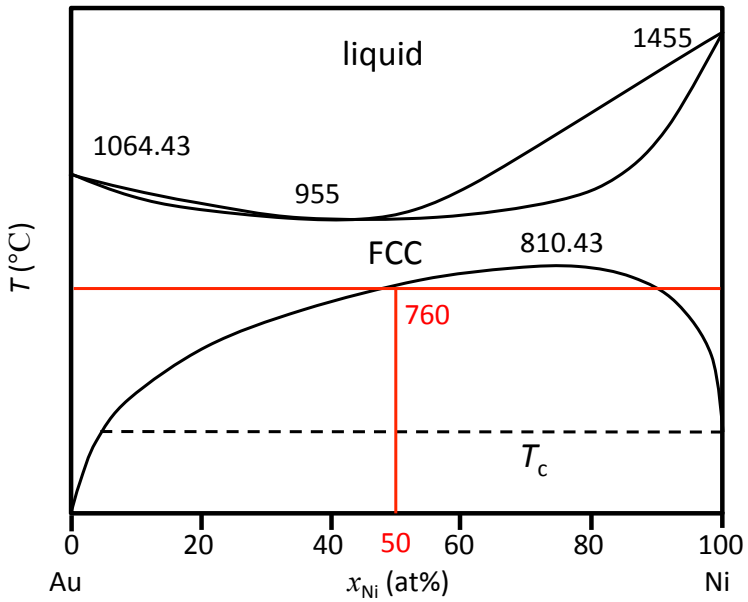


Figure 3.40 Calculated Au-Ni binary phase diagram [188].

## 3.3.6 Fe-Cu

All of the above whisker heterostructures were synthesized at a fixed temperature, as the substrate temperature remained unchanged during the deposition of both materials. However, each material has its own temperature window for its respective whisker growth. And since these windows do not always overlap, it would be interesting to see the results of depositing each material at its own optimal growth temperature.

In order to have a stable whisker structure, the deposition temperature for the first material should be higher than that of the second one. Because the Fe whiskers have a higher growth temperature than the Cu ones, the substrate (Mo wire) was first heated to 780 °C for the deposition of 90 nm Fe and, then, cooled down to 650 °C where it received the subsequent deposition of 90 nm Cu. The result is shown in Figure 3.41. A core-shell structure was formed as evidenced by the diffraction contrast on the DF image. The thin bright shell was further identified as FCC Cu while the whisker core was identified as BCC Fe. Meanwhile, no axial heterostructure was observed on the sample.

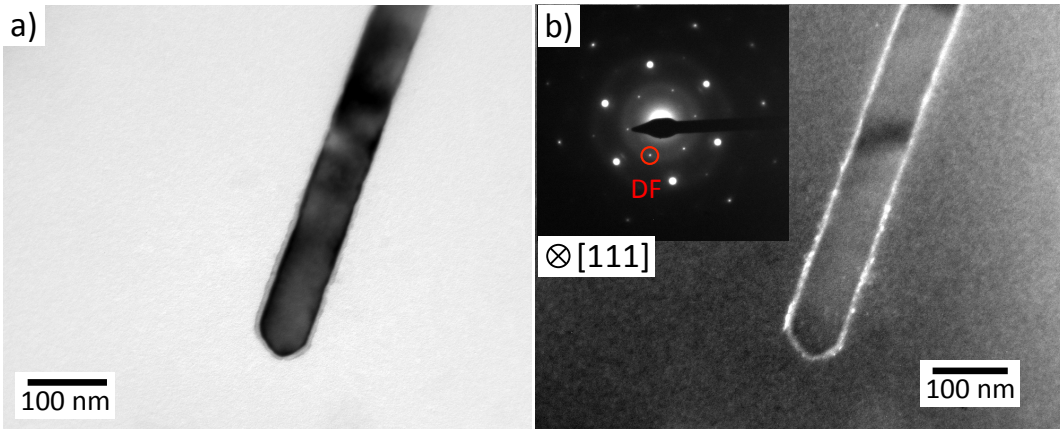


Figure 3.41 (a) TEM BF image of a Fe-Cu whisker heterostructure obtained on a Mo wire. (b) TEM DF image and (inset) corresponding diffraction pattern of the same whisker heterostructure showing the existence of a core-shell structure. The red circle marks the diffraction condition (FCC Cu [110]) at which the DF image was taken.

## 3.3.7 Ni-Ag

The same has been achieved with Ni and Ag on Mo wires. The substrate temperature was held at 760 °C during the deposition of 90 nm Ni before being reduced to 650 °C for the subsequent deposition of 90 nm Ag. Despite that no material contrast was observed on the HAADF image Figure 3.42-a), EDX mapping (Figure 3.42-b) revealed once again a core-shell only heterostructure (*i.e.* without the presence of an axial whisker heterostructure). The Ni (red) whisker core was found to be surrounded by a Ag (green) shell. The inhomogeneity of the Ag shell layer was attributed to the shadowing effect by the Ni whisker which was growing almost parallel to the substrate surface.

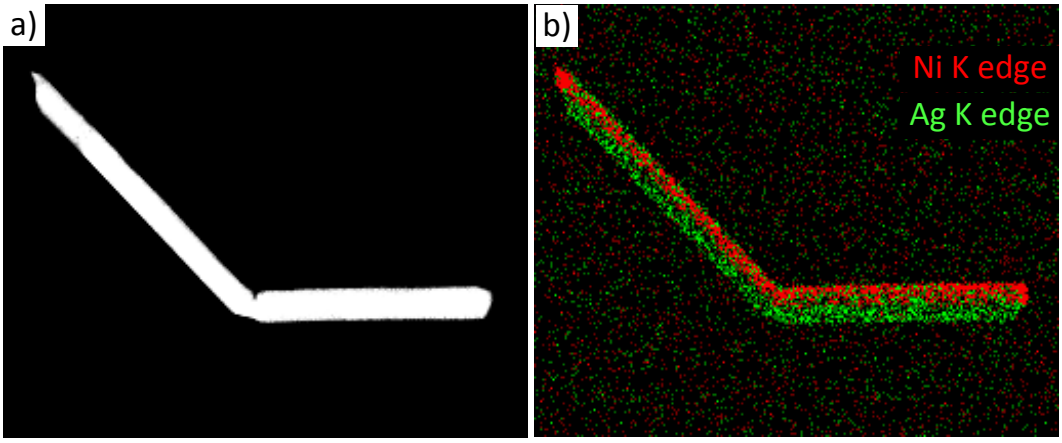


Figure 3.42 (a) HAADF image and (b) EDX mapping result on a Ni-Ag whisker heterostructure obtained on Mo wires.

To conclude, it seems that only radial growth occurred when growing whisker heterostructures for the systems Fe-Cu and Ni-Ag at disparate temperatures. The absence of

the root growth is explained by a more stable binding with the substrate for whiskers of the first material than for whiskers of the second material. As a result, it is energetically not favorable to insert, for instance, Cu atoms at the root site of the already grown Fe whiskers. The absence of the tip growth can be understood as due to insufficient surface diffusion of Cu adatoms on the surface of Fe whiskers. The transport of the adatom of the second material all the way to the tip of the whisker structure was hindered by the low adatom mobility at lower substrate temperatures. Details will be discussed in Section 5.

# 4 Size Effects of Whiskers

One of the better known size effects for metal whiskers is "smaller is stronger" [18,78]. It states the phenomenon that materials with reduced dimensions usually exhibit extraordinary mechanical properties. Size effects have been observed in both semiconductor nanowires [82] and metallic whiskers, affecting not only their mechanical but also their electrical, optical and magnetic properties [68,80,81,84]. Size effects can usually be explained by surface effects which become more pronounced with the decreasing size of objects [18]. It has previously been demonstrated that size of the Co nanoparticles has an impact on their phase transformation [106,113] as well as on their magnetic properties [86,112]. In this chapter, we will present our results concerning the effect of size on the phase transformation (Paragraph 4.1) and magnetic domain structure (Paragraph 4.2) of Co, Ni and Fe whiskers.

## 4.1 Phase Transformation of Co Whiskers

Bulk Co exists as two allotropes over a wide range of temperatures. The stable crystal structure is FCC at higher temperature and HCP at lower temperature. The phase transformation between the two allotropic phases is a martensitic one [189], which is a diffusionless process often accompanied by volume changes. The optimal growth temperature for Co whiskers is 760 °C. The sample cool-down after growth thus inevitably involves passing through the equilibrium point of phase transformation $T_0$ at 422 °C [53]. Co whiskers of either FCC or HCP (Figure 3.16) structure have been observed at room temperature. Traces of the other phase (*i.e.* HCP for a FCC whisker and FCC for a HCP whisker) were also detected in the form of microtwins and stacking faults.

It has been established that the phase transformation of bulk Co from FCC to HCP can be promoted by thermal treatment [111]. In order to understand the phase transformation process, *in situ* heating and cooling experiments were carried out in a JOEL ARM1250 TEM. The crystal structure of Co whiskers was first studied at room temperature (RT). The TEM grid was then rapidly heated to 700 °C, before being cooled down in steps back to RT. After that, the whiskers were slowly heated up to 750 °C again. Detailed microstructural studies were performed at different temperatures during the cooling and the second heating process. The specimen was later transferred onto a cooling holder which allowed the effect of overcooling to be studied down to -161 °C. Both the FCC and the HCP structures have been constantly observed over the entire process. Typical HR images of the measurements at different temperatures are shown in

Figure 4.1. The co-existence of the two allotropes is explained by an incomplete phase transformation process.

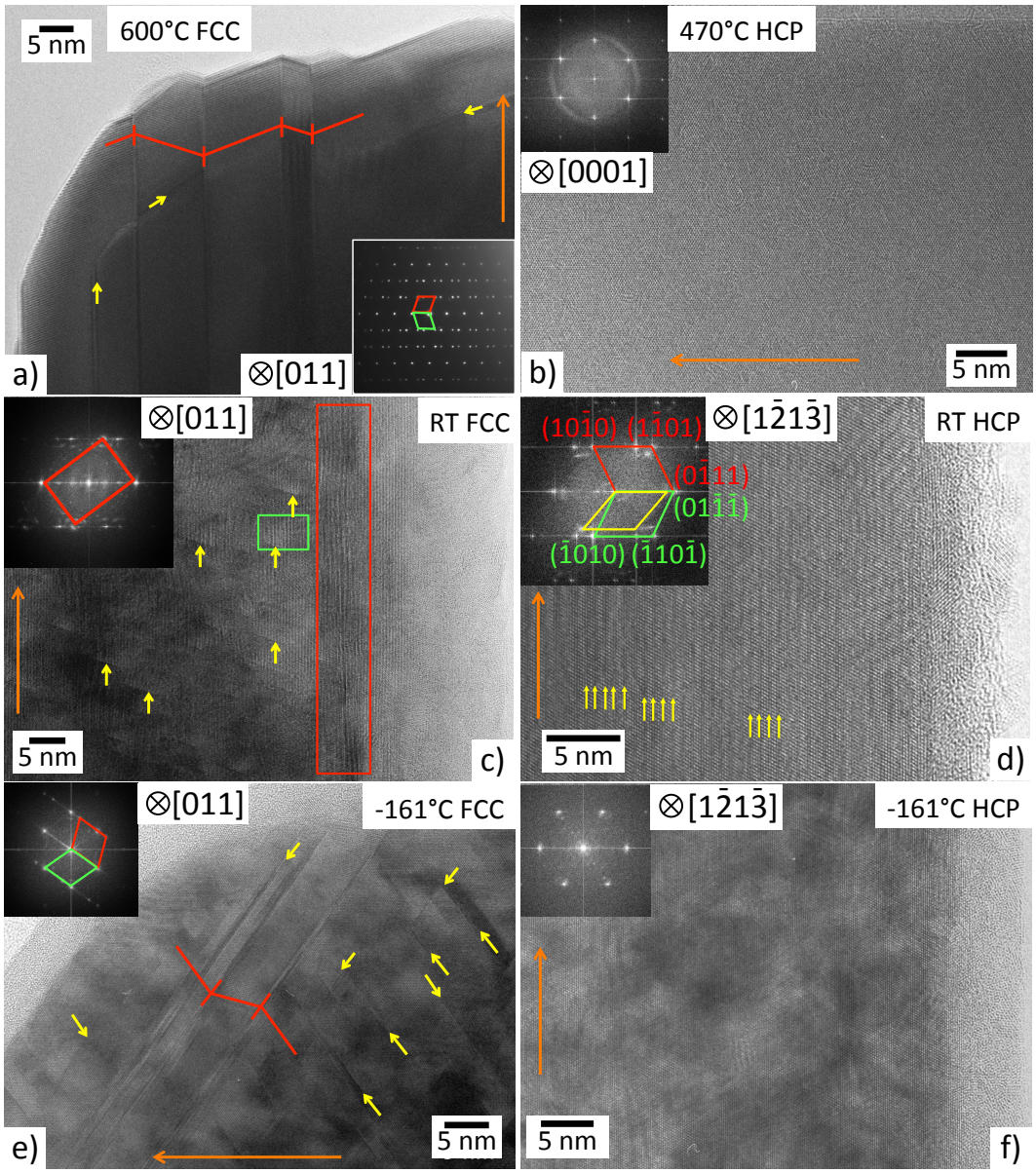


Figure 4.1 HRTEM micrographs of Co whiskers with FCC and HCP structures at (a,b) high temperature, (c, d) room temperature and (e, f) low temperature. The orange arrows mark the axial direction of the whiskers. Diffractions from twin grains were marked in red and green frames, respectively. Diffraction from the oxide was marked in a yellow frame. The yellow arrows indicate the position of the stacking faults. The red lines mark the reflected orientations and the twin grain boundaries.

At RT (Figure 4.1-c), numerous partial dislocations (of type $\frac{1}{6}$<112>) and stacking faults (marked by the yellow arrows) were observed on the FCC whisker. Series of microtwins were also observed near the Co-oxide interface (marked by the red rectan-

gle). In comparison, (Figure 4.1-b) the HCP whisker is composed of homogenously distributed microtwins, with stacking fault appears at every 4$^{th}$ {0111} crystal plane. The existence of the twin structure was further confirmed by the FFT pattern (inset).

At 600 °C (Figure 4.1-a), the stacking faults (yellow arrows) in the FCC whisker became comparably longer. The accompanying partial dislocations were still of type $\frac{1}{6}$<112>. The part of the FCC whisker within the field of view consists of 5 twin grains. The reflected orientations and the twin grain boundaries are marked with red lines. The coherent twin grain boundaries are parallel to the direction of the whisker axis (orange arrow) and to one of the <112> directions. This is in sharp contrast to what was observed (Figure 4.1-b) on the HCP whisker at 470 °C. The HCP whisker showed a perfect crystalline structure without the presence of any defects. The whisker axis is along the $[\bar{1}2\bar{1}0]$ direction. No oxide has been observed on either the FCC or the HCP whisker at these temperatures.

An increase in the defect density (stacking faults and partial dislocations) was observed when cooling the FCC whisker down to -161 °C (Figure 4.1-e). Twin grains (red lines) were also observed. The twin grain boundaries were not parallel to the whisker axis but still parallel to one of the <112> direction. The perfect crystalline structure in the HCP whisker after annealing was preserved during the cool down process (Figure 4.1-f). The observed moiré patterns were caused by the epitaxial crystallized oxide on the whisker surface.

Figure 4.2 shows the cross-sectional area of a Co whisker without any thermal treatment. The pentagon shaped cross section contains many defects, which were identified as microtwins and stacking faults on the HRTEM image. The cross section can be further divided into 7 zones bordered by microtwins. FFT were performed on each of the 7 zones. All of the FFT patterns fit to FCC structures in <110> zone axis. The image was thus taken from a (mainly) FCC whisker. The crystal orientation of the different zones are perhaps better visualized with the help of the colored rectangles connecting the {111} diffraction spots on the FFT pattern. For instance, zone 4 and 5 has almost identical orientation and were thus marked with the same color. A total of 5 different orientations were thus observed, which explains the pentagonal shape of the cross section. The node where 5 zones of different orientations joined together was marked by the red asterisk. Each line of the asterisk lies on the transition boundary between two adjacent zones and is along the <112> direction. These transition boundaries are all made of {111} planes. The angles between adjacent boundary planes were measured as 71±3.5°, which correspond well to the angle (70.32°) between two <112> directions or between two {111} planes. However, an additional grain is needed to complete the node since 5 times 70.32° is 8.4° short of 360°. No such grain was observed on the cross section, and the missing

8.4° was filled jointly by the 5 transition boundaries. A similar phenomenon was reported in the case of 5 fold twinning Ag [177], and Cu [178] nanowires. Each side of the pentagonal cross section of the FCC Co whisker is a {100} plane. At the junction of adjacent sides, some small {112} planes were found, probably formed by microtwins or roughening transitions.

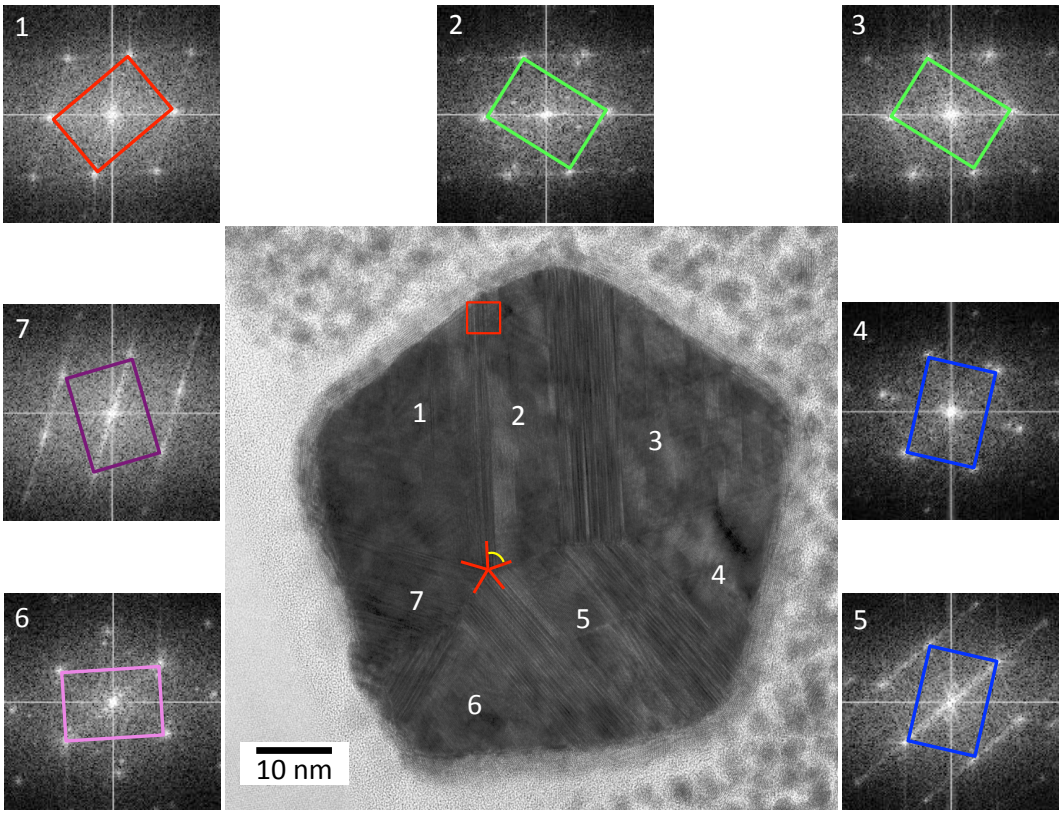


Figure 4.2 HRTEM micrograph of the pentagonal cross section of a Co whisker. The cross section can be divided into 7 zones with different orientations. The colored rectangles mark the {111} diffraction spots on each of the corresponding FFT patterns.

The transition boundary between adjacent zones was composed of microtwins. To study these, HAADF images were taken on these transition areas. One of them is shown in Figure 4.3-a. An average background subtraction filter (ABSF) was applied to remove the contribution of the amorphous phase [191]. The stacking sequence of the {111} planes along the <112> direction is marked with green lines. The blue (A), green (B) and red (C) triangles each represent a different layer in the stacking sequence. On the upper part of the HAADF image were a series of microtwins. The twin structures changed the FCC stacking sequence from ABCABC to ABCACB. The latter can be regarded as a small HCP grain (CAC) inserted in the FCC structure. With that in mind, the observed atomic structure can be divided into regions of FCC and HCP crystals with twin boundaries as their overlapping area. The FCC crystals on the upper part of the HAADF image consist of only 3 atomic layers, much thinner than their neighboring

HCP crystals. As a result, they can be considered as stacking faults in the larger HCP matrix which occupies the upper half of the field of view. The FFT pattern (Figure 4.3-b) of the upper part of the image also indicates a HCP crystal structure. On the other hand, the atomic structure of the lower part of the image is mainly FCC, as confirmed by the corresponding FFT pattern (Figure 4.3-c). The FCC and the HCP phases follow the Shoji-Nishiyama (S-N) relationship with $(111)_{FCC}$ // $(0001)_{HCP}$ and $[110]_{FCC}$ // $[11\bar{2}0]_{HCP}$ [192,193]. These indicate that the transformation from FCC to HCP during the cool-down process after growth was completed for half of the crystal in the HAADF image. Coming back to Figure 4.2, the microtwins (HCP phase) between two adjacent FCC grains are the preferred nucleation site for the phase transformation. This applies also to the transition areas between grains with the same orientation (*e.g.* zone 4 and 5).

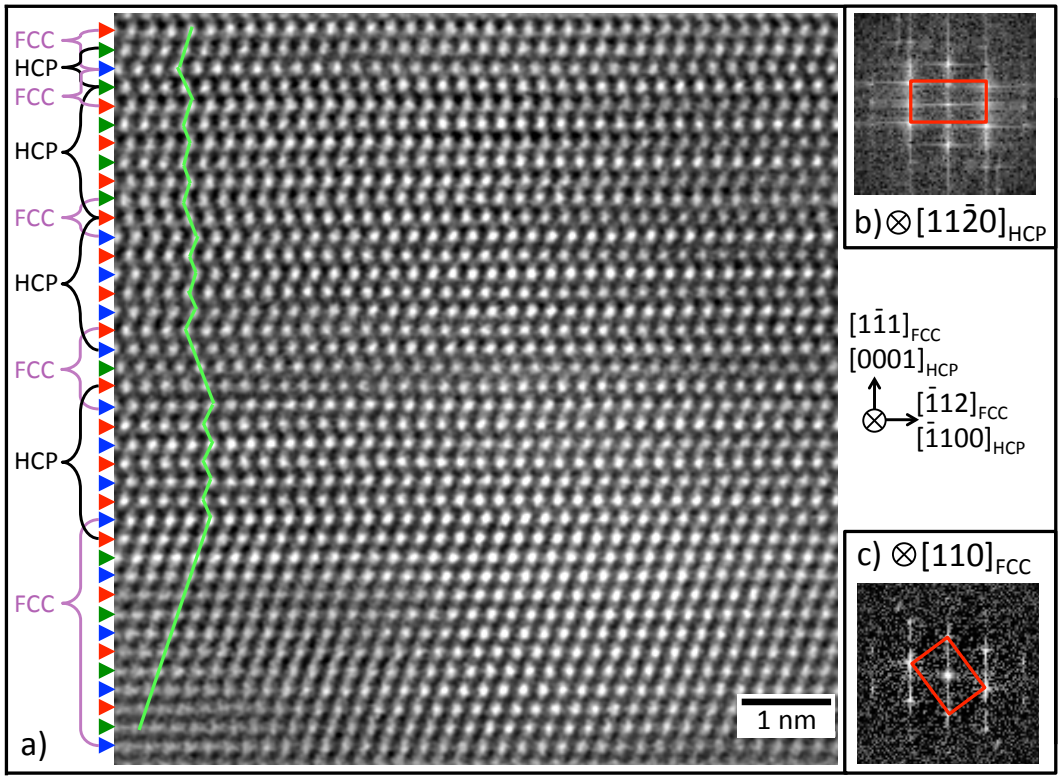


Figure 4.3 (a) ABSF filtered HAADF image of the area marked in the red rectangle in Figure 4.2. The image was rotated counterclockwise by about 90 degree. The colored triangles mark different stacking of the {111} planes. FFT patterns were extracted individually from the upper part (b) and the lower part (c) of the HAADF image. The result shows the Shoji-Nishiyama relation between the FCC and HCP phases.

*In situ* cooling experiment can provide better insight into the phase transformation process. The HR images of the tip of a Co whisker during different stage of the cool-down procedure are shown in Figure 4.4. Two grains (marked with red arrows) were observed at 700 °C which have twinned orientation with regard to the rest of the whisker. Their grain boundaries were parallel to the whiskers axis (orange arrow). During the

cool-down, the grain boundaries glided towards the left edge until they were completely expelled from the whisker, leaving behind a single grain FCC structure. This is quite surprising as the HCP is the more stable phase at RT. The number of stacking faults (yellow arrows) also increased with decreasing temperature.

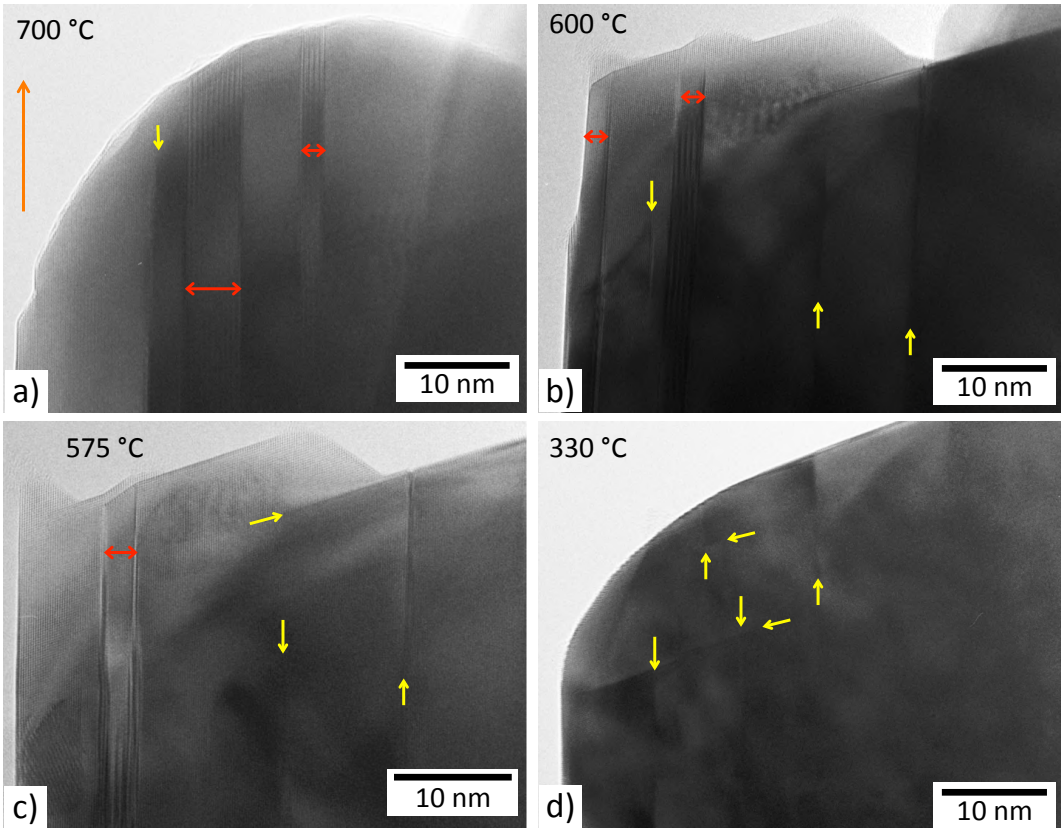


Figure 4.4 TEM micrographs of the tip of a Co whisker at different temperatures during the cool down process from 700 °C to RT.

The microtwin structures inside the twin grains fluctuated during cool-down as they were seen disappearing and reappearing throughout the process. After being heated for the first time to 700 °C (Figure 4.5-a), the two twin grains are composed completely of microtwins. When cooled down to 600 °C (Figure 4.5-b), the microtwins started to de-twin. The entire grain on the left as well as the upper part of the one on the right showed a perfect FCC structure. Microtwins were only preserved in the lower part of grain on the right. The shape change of the whisker tip in the video is understood as due to atoms being evaporated from the whisker surface at high temperature and under high-energy electron beam.

We have previously treated the microtwins as HCP structures in the FCC whisker. The FCC-HCP transformation expected in the above cool-down process was thus realized by the gliding and disappearance of the microtwins (Figure 4.4). This transformation process was not reversible as no twins or microtwins were formed during the second

heating process from RT to 750 °C (Figure 4.6). A huge amount of stacking faults was observed instead. The stacking faults fluctuated upon reheating, although their density remained relatively constant.

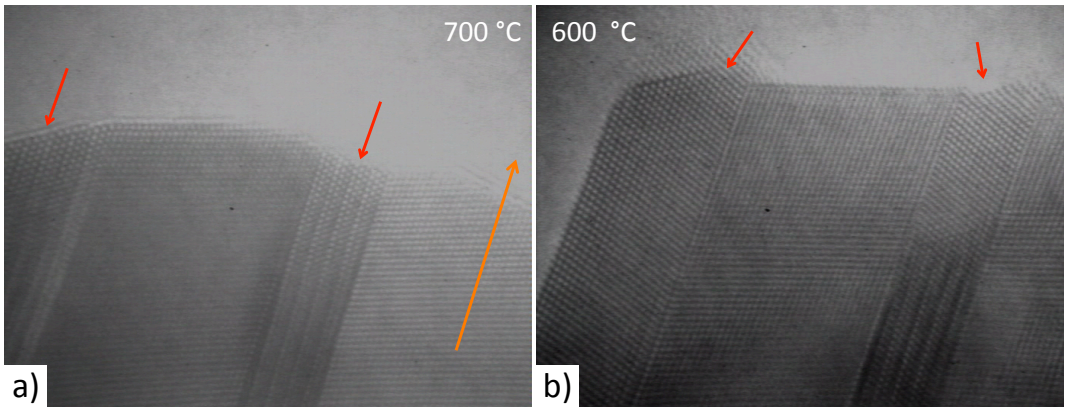


Figure 4.5 Screen captures from the video of the *in situ* cooling experiment showing fluctuations of the microtwins inside the twin grains (red arrows). The twin grains were the same as the ones shown in Figure 4.4.

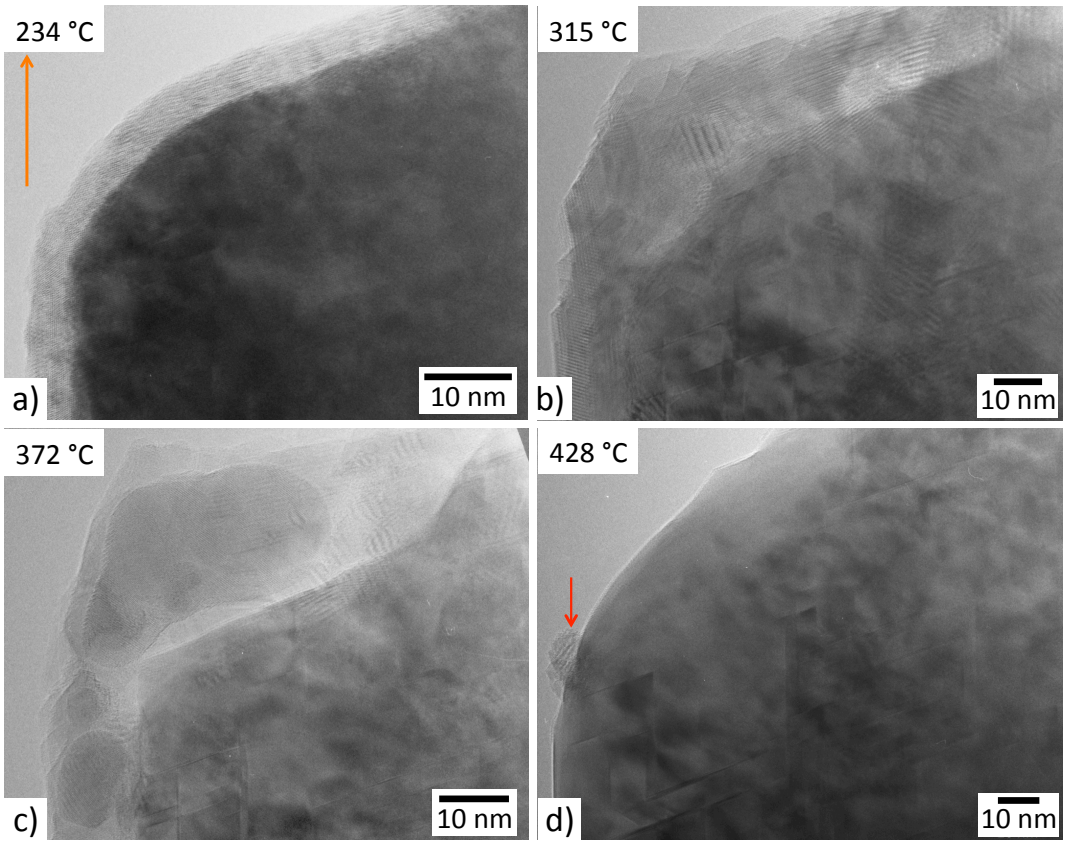


Figure 4.6 TEM micrographs of the tip of a Co whisker at different temperatures during the second heating process from RT to 750 °C.

Due to the high growth temperature ($T > T_0$), the more stable phase during growth should be FCC. However, the rather fast kinetic growth process (deposition rate at 0.5

nm/s) inevitably led to the formation of some defected segments, which manifested themselves as HCP (under the form of microtwins). Despite HCP being the more stable phase for bulk materials at RT, the cool down process after growth did not facilitate the conversion of the already formed FCC to HCP. It was possible, however, to convert HCP to FCC by annealing. The preference of forming and preserving the FCC phase was probably related to the small grain size and the high aspect ratio of the Co whiskers. Similar findings have been reported by Owen [106] in 1954, where it was concluded that the FCC phase is more stable in smaller grains due to its lower surface energy [113].

It has been previously established [103,111,189] that the martensitic transformation is accomplished by the motion of Shockley partial dislocation, and that the transformation process can be affected by external stress [109]. To confirm this, tensile tests were performed on the Co whiskers. The experiments were carried out inside a dual beam (SEM/FIB) system using an *in situ* manipulator [194]. The application of the external stress is expected to promote the FCC to HCP transformation.

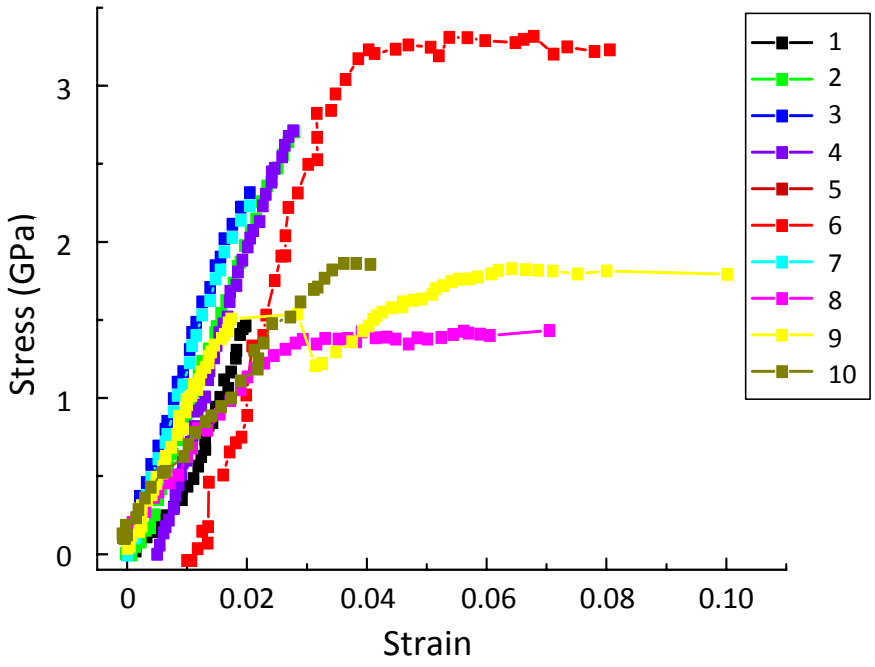


Figure 4.7 Stress-strain curves from the tensile tests on the Co whiskers.

Figure 4.7 shows the stress-strain curves of the tensile tests on 10 Co whiskers with diameter ranging from 44 to 112 (±10) nm. Specimen 3 and 4 were actually the same whisker, with the latter being one of the fractured parts of the former after its failure. The same applies to specimen 5 and 6. Among the 10 specimens, only 4 whiskers (6, 8, 9 and 10) showed plasticity before fracture, while the other 6 exhibited brittle fracture with only linear stress strain behavior. The results of the tensile tests are summarized in Table 4.1. No definitive size dependence was observed on the calculated Young's modulus, tensile strength or fracture strain, probably due to the small sample pool size and

the arbitrary defect density in the whiskers. The absence of a size dependent trend in mechanical response was previously reported on Cu whiskers synthesized with the same method [68]. The fracture strain scattered between 1.98 and 10.01%, and the Young's modulus (the slope of the linear segment of each curve) varied from 51 to 132 GPa. Despite the observed brittle behavior, the average tensile strength of the Co whiskers (2.2±0.58 GPa) is much higher compared to their bulk counterparts (800-875 MPa) [102]. The average value also exceeds that of the nanocrystalline Co whiskers (whisker diameter ~ 300 nm) synthesized via electrochemical deposition (1.6±0.4 GPa) [195] as well as that of the nanocrystalline (grain size ~12 nm) Co sheet (1.9±0.7 GPa) [196]. The high tensile strength of the Co whiskers was attributed to the high defect density (partial dislocations, stacking faults, grain boundaries) as well as to their high aspect ratio, which in turn blocked or retarded the motion of lattice dislocations.

Table 4.1 Results of tensile tests on Co whiskers.

| Whisker # | Diameter (nm) | Young's modulus (GPa) | Tensile strength (GPa) | Fracture strain (%) |
|---|---|---|---|---|
| 1 | 100 | 72.38 | 1.46 | 1.98 |
| 2 | 112 | 102.61 | 2.71 | 2.79 |
| 3 | 92 | 116.65 | 2.32 | 2.05 |
| 4 | 92 | 124.66 | 2.71 | 2.77 |
| 5 | 50 | 80.02 | 2.29 | 3.01 |
| 6 | 50 | 132.16 | 3.23 | 8.06 |
| 7 | 44 | 115.81 | 2.23 | 2.05 |
| 8 | 48 | 48.69 | 1.43 | 7.05 |
| 9 | 98 | 87.22 | 1.79 | 10.01 |
| 10 | 66 | 51.14 | 1.86 | 4.06 |
| Average | 75.2 | 93.13 | 2.20 | 4.38 |
| STDEV | 26.08 | 29.91 | 0.58 | 2.91 |

Postmortem TEM analysis was carried out on the whiskers after their fracture from the tensile test, to study the effect of tensile stress on the crystal structure. The BF image of specimen 4 is shown in Figure 4.8. The fracture strength of the whisker was 2.71 GPa where a failure strain of 2.77% was measured. A kink (blue circle) was observed near

the fracture (green circle). Diffraction patterns were acquired (inset A) near the fracture, (inset B) on the kink and (inset C) far away from the fracture. It became obvious that pattern A and C are almost identical and match that of the FCC structure in [110] zone axis. In comparison, pattern B was found to better fit with HCP structure in [0001] zone axis. This implies that the tensile stress applied during the test might have promoted the formation of the HCP phase in the FCC Co whisker. The FCC-HCP phase transformation was accomplished by the motion and interaction of the partial dislocations. These motion and interactions can result in formation of twins, which may in turn be responsible for the kinks that were observed. Another possibility to form the kinks would be the deformation twins under tensile stress [97].

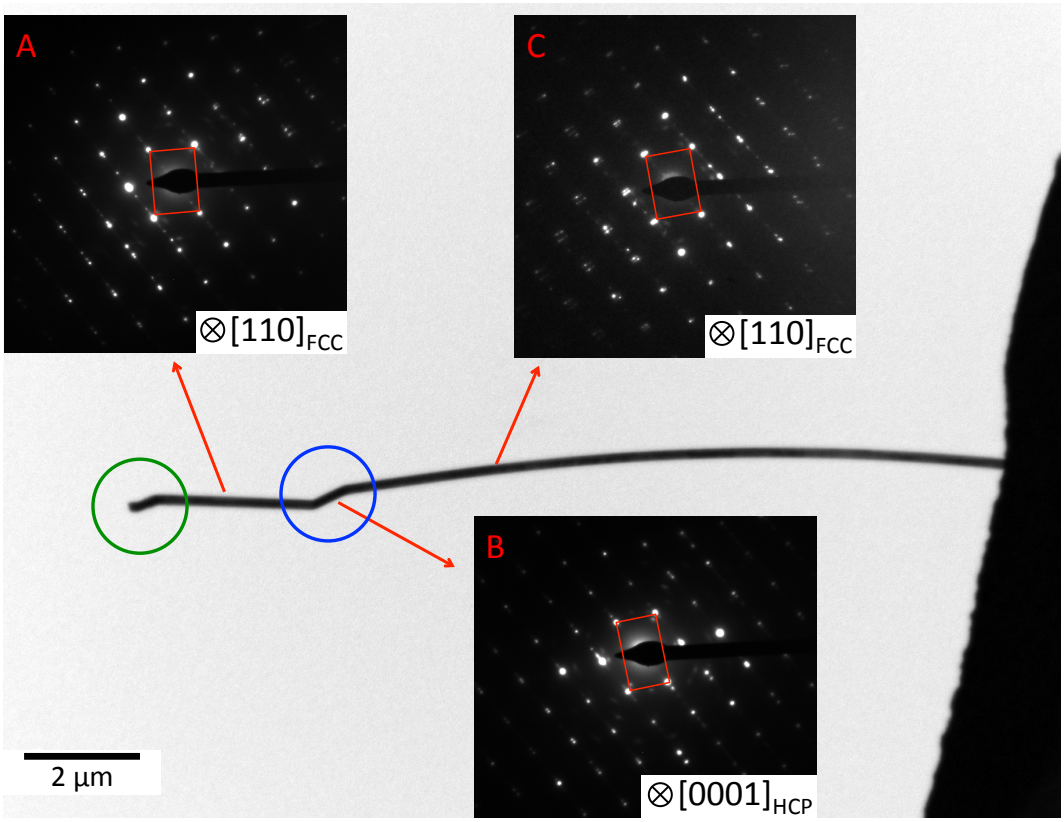


Figure 4.8 TEM BF image on a FCC Co whisker fractured after the tensile test as well as the diffraction patterns (insets) taken on different parts of the whisker. Inset A and C show a FCC structure while inset B shows a HCP structure.

To conclude, the stable crystal structure of Co whiskers at ambient condition is FCC. HCP crystals can also be observed in the FCC whiskers, in the form of microtwins. They are the result of the fast kinetic growth and of the incomplete phase transformation during the cool-down process. The HCP phase formed during growth separated the FCC crystal into multiple twin grains, which in turn gave rise to a pentagonal cross section in the whisker structure. The HCP phase was eliminated by slow cool-down after annealing and did not appear upon reheating. The FCC-HCP transformation can be promoted

by applying an external tensile stress. In general, the Co whiskers synthesized in this work demonstrated extraordinary tensile strength.

## 4.2 Magnetic Domain Structures

The whiskers synthesized in this work are, with the exception of Co, large perfect crystal structures that may or may not contain Σ3 twins. They all have perfect crystal facets with clean and smooth surfaces. These whiskers are the ideal samples for studying the magnetic properties of materials, as they are not affected by incoherent grain boundaries (excluding twin boundaries) or impurities. The peculiar geometry of the whiskers and platelets also provide a unique perspective to the understanding of size related properties in magnetic structures. Whiskers and platelets of Fe and Co were studied with electron holography at room temperature under zero-field conditions. For each measurement, a second hologram was recorded with the specimen inverted, in order to separate the mean inner potential (MIP) with the magnetic field (MAG) contributions in the total phase shift. A reference hologram was also recorded in vacuum for each measurement for the correction of instrumental and experimental artifacts.

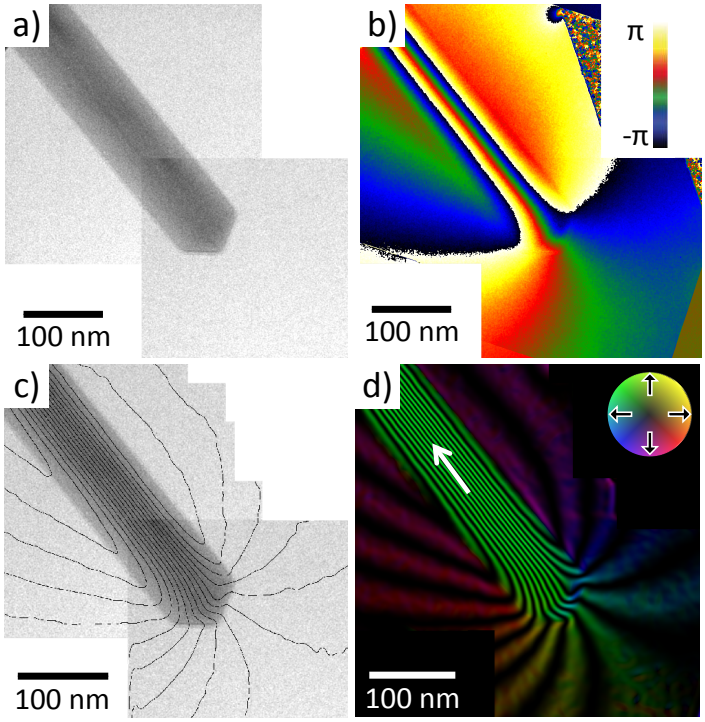


Figure 4.9 Electron holography results on a Co whisker: (a) amplitude image; (b) MAG phase shift; (c) MAG phase contour overlaid with the amplitude image showing the in plane magnetic induction, the spacing of the contour is 0.75 radians; (d) Magnetic flux lines calculated as the cosine of 7 times the MAG contribution to the measured phase shift. The magnetization direction is marked by the white arrow.

Figure 4.9 shows the electron holography results of a Co whisker. The morphology of the whisker can be visualized in the amplitude image (Figure 4.9-a). The whisker has a uniform diameter of about 90±2 nm. Figure 4.9-b is the MAG phase shift image. The so-called wrapped phase, calculated as the modulo of 2π, is indicated by the false color scale. The outline of the whisker is clearly distinguishable on the phase shift image. The MAG phase shift was along the direction perpendicular to the whisker axis, indicating that the magnetization was along the direction of the whisker axis. A phase-unwrapping algorithm was later applied to remove the discontinuities in the wrapped phase. The contour map (Figure 4.9-c) generated from the unwrapped MAG contribution shows the remnant magnetic state of the whisker, which allows for quantitative analysis of the strength and direction of the local flux. The contour lines were homogeneously distributed within the whisker. Their density is proportional to the in-plane component of the induction of the specimen integrated along the electron beam direction. Figure 4.9-d shows the magnetic flux lines calculated as the cosine of 7 times the MAG contribution. The value 7 is arbitrary and was chosen in order to obtain a reasonable density of the flux lines inside the specimen. A low pass filter was applied to suppress the high frequency noise. The direction of the induction is represented by the flux lines while its magnitude is shown in fake color scale. The flux lines within the whisker are parallel to the sidewall. No disturbance from domain wall was observed, indicating a single domain structure inside the Co whisker.

In Figure 4.10 is shown the holography results on a Fe whisker. The diameter of the whisker is 70±2 nm. The montage of the 12 holograms covers a total 2.2±0.05 μm of the 6.25±0.05 μm long whisker. No domain wall was observed. The whisker showed a homogeneous magnetization along its axial direction. Some particles were observed on the whisker surface. EDX analysis showed the particles to consist primarily of Mo. These particles were probably substrate dusts introduced during TEM sample preparations. Further analysis indicated that these particles exhibited no magnetic feature and had hence no effect on the magnetic domain structure of the whisker.

We shall now calculate the energy densities of this Fe whisker. For BCC Fe whiskers, the whisker axis coincides with the crystal easy axis, along the <001> direction. The whiskers were randomly distributed on the TEM grids, with enough separation between them to be considered each as an isolated object. Regardless of the magnetostriction effects, the energy density of the 3 different magnetization configurations of the Fe whisker (Paragraph 1.4.3.3) can be calculated with $M_s = 1714$ emu/cm$^3$ [127] and $\sigma_{w,Fe}^{180} = 2$ erg/cm$^2$ [130], the latter being the specific energy of the (100)-180° wall. The aspect ratio of the whisker is $c/a \approx 90$. This gives a demagnetization coefficient of $N_d = 0.00528$ [197]. For a multi-domain structure with magnetization perpendicular to the whisker axis, the minimum energy density is calculated as

$$e_{min} = 4\sqrt{\frac{1.7\sigma_w}{W}} \cdot M_s = 4.778\times10^6 \text{ erg/cm}^3, \quad (1.41)$$

with a domain size of $D = \sqrt{\frac{\sigma_w W}{1.7{M_s}^2}} = 16.7$ nm (1.39).

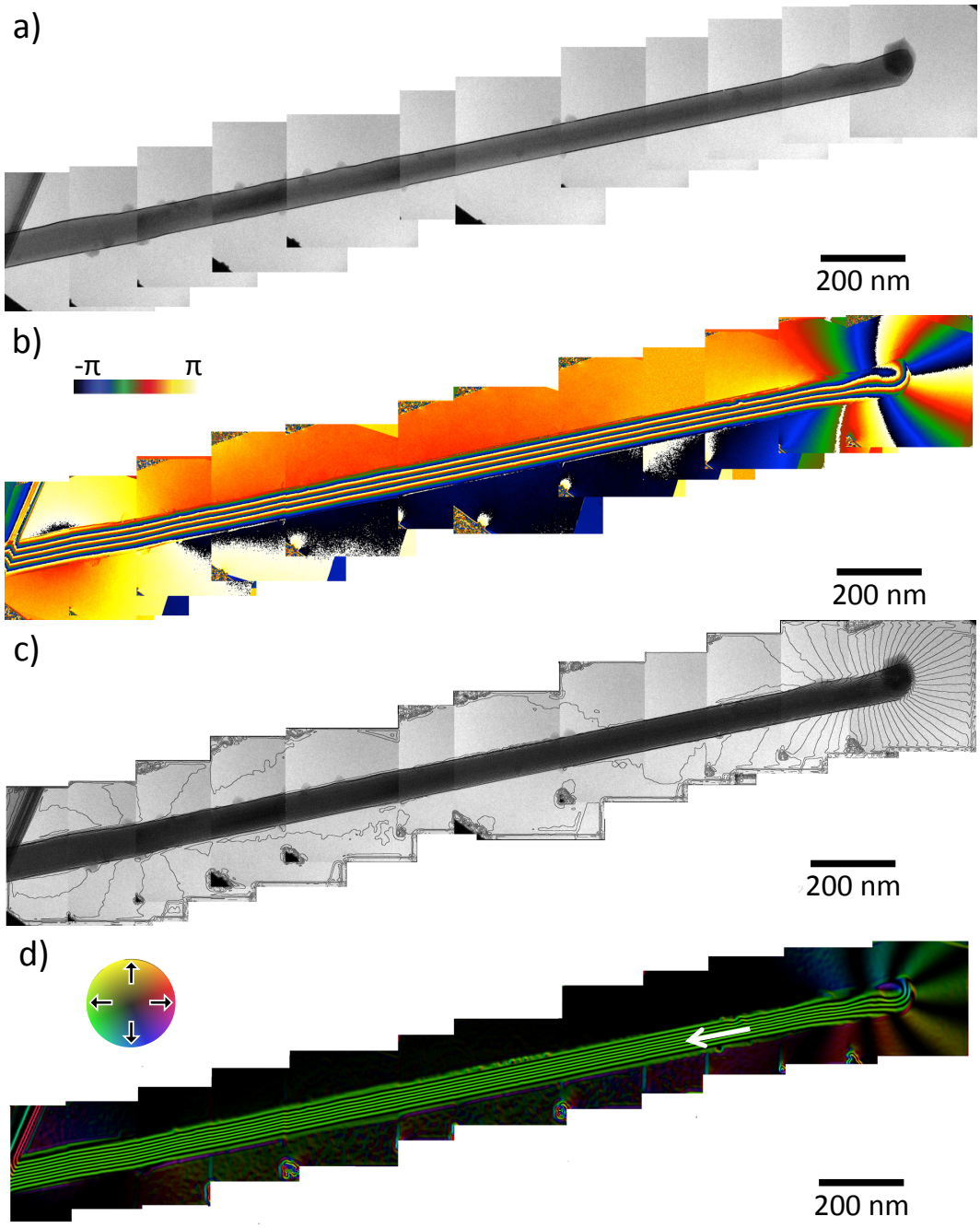


Figure 4.10 Electron holography results of a Fe whisker: (a) amplitude image; (b) MAG phase shift; (c) MAG phase contour overlaid with the amplitude image showing the in plane magnetic induction, the spacing of the contour is 0.49 radians; (d) Magnetic flux lines calculated as the cosine of 2 times the MAG contribution to the measured phase shift. The magnetization direction is marked by the white arrow.

The energy density of a two-domain structure with magnetization parallel to the whisker axis is

$$e_w = \frac{\sigma_w}{W} = 2.8\times10^5 \text{ erg/cm}^3. \quad (1.42)$$

At last, the energy density of a single domain structure at saturation magnetization writes

$$e_{ms} = \frac{1}{2} N_d {M_s}^2 = 7.756\times10^3 \text{ erg/cm}^3. \quad (1.43)$$

It is then obvious from the comparison that single domain is energetically the most favorable structure for Fe whiskers of high aspect ratio.

Let us now consider the FCC Ni whiskers. Their easy axis (<111>) is not along the whisker axis (<011>). As a result, extra magnetocrystalline anisotropy energy is required for magnetizations along the whisker axis. For Ni whiskers, $M_s = 485$ emu/cm$^3$ [127] and $\sigma_{w,Ni}^{180} = 2$ erg/cm$^2$ [130]. Considering whiskers of length 5 μm and width 100 nm, we have an aspect ratio of $c/a \approx 50$ and a demagnetization coefficient of $N_d = 0.0094$ [197]. The minimum energy density for a multi-domain structure with magnetization perpendicular to the whisker axis is thus

$$e_{min} = 4\sqrt{\frac{1.7\sigma_w}{W}} \cdot M_s = 1.13\times10^6 \text{ erg/cm}^3, \quad (1.41)$$

with a domain size of $D = \sqrt{\frac{\sigma_w W}{1.7{M_s}^2}} = 70.7$ nm (1.39).

The energy density of a two-domain structure with magnetization parallel to the whisker axis is

$$e_w = \frac{\sigma_w}{W} = 2\times10^5 \text{ erg/cm}^3. \quad (1.42)$$

At last, the energy density of a single domain structure at saturation magnetization writes

$$e_{ms} = \frac{1}{2} N_d {M_s}^2 = 1.106\times10^3 \text{ erg/cm}^3. \quad (1.43)$$

But that is not all. Since the easy axis is not parallel to the whisker axis, the magnetization along the whisker axis will cost extra anisotropy energy. The cosine between the two axes is $\pm\sqrt{6}/3$. The extra anisotropy energy density cost is, according to Table 1.1

$$\Delta e_{mc} = e_{mc(110)} - e_{mc(111)} = -\frac{K_1}{12} - \frac{K_2}{27},$$

with $K_1 = -4.5\times10^4$ erg/cm$^3$, $K_2 = -2.5\times10^4$ erg/cm$^3$ [130], the extra anisotropy energy density is thus $\Delta e_{mc} = 4.676\times10^3$ erg/cm$^3$. Even when taking into account this additional energy, the energy density of the single domain structure is still the lowest among the three structures. The direct implication is that the single domain structure is, to a large extent, the most energetically favorable structure for all whiskers with high aspect ratio, as the shape anisotropy in these cases predominates over the magnetocrystalline anisotropy.

Next, we shall apply this conclusion to the FCC Co whiskers. Like the Ni whiskers, their easy axis is along the <111> direction while their whisker axis is along the <011> direction. With $M_s = 1445$ emu/cm$^3$, the exchange stiffness constant $A = 3.0\times10^{-6}$ erg/cm [198] and the anisotropy constants $K_1 = -5.7\times10^5$ erg/cm$^3$, $K_2 = 1.3\times10^5$ erg/cm$^3$ [199], we obtain the specific domain wall energy $\sigma_{w,Co}^{180} = 2.6$ erg/cm$^2$. Taking the same aspect ratio (50) and the same demagnetization coefficient (0.0094) as before, the minimum energy density for the multi-domain structure with magnetization perpendicular to the whisker axis is calculated as

$$e_{min} = 4\sqrt{\frac{1.7\sigma_w}{W}}\cdot M_s = 3.84\times10^6\ \text{erg/cm}^3, \qquad (1.41)$$

with a domain size of $D = \sqrt{\frac{\sigma_w W}{1.7{M_s}^2}} = 27.1$nm (1.39).

The energy density of a two-domain structure with magnetization parallel to the whisker axis is

$$e_w = \frac{\sigma_w}{W} = 2.6\times10^5\ \text{erg/cm}^3. \qquad (1.42)$$

At last, the energy density of a single domain structure at saturation magnetization writes

$$e_{ms} = \frac{1}{2}N_d{M_s}^2 = 9.81\times10^3\ \text{erg/cm}^3. \qquad (1.43)$$

The extra energy density costs from magnetocrystalline anisotropy is

$$\Delta e_{mc} = e_{mc(110)} - e_{mc(111)} = 4.27\times10^4\ \text{erg/cm}^3.$$

And the single domain structure is still the lowest free energy state among the three domain structures.

Regarding the HCP Co whiskers, the uniaxial symmetry of the HCP lattice initially caused a large magnetocrystalline anisotropy. However, for whiskers with very high aspect ratios, the shape anisotropy becomes predominant which forces the magnetization to align with the whisker axis. Hubert and Schäfer [134] calculated the critical value of the aspect ratio to be 3.5, at which point the shape anisotropy constant becomes comparable to the crystal anisotropy constant with $K_s \approx K_1 = 4.5\times10^6$ erg/cm$^3$.

The magnetization properties may change with the redimensioning of the nano-object. For instance, the magnetization direction of the Ni lamella (the same one shown in Figure 3.14-a) was found to have changed from being originally along the whisker axis to being in the cross-sectional plane. The longer diagonal measures 145±5 nm and the short one 110±5 nm. The MAG phase shift image in Figure 4.11 shows only a tiny phase shift along the short diagonal (the <110> direction), indicating the presence of a weak magnetization along the long diagonal (white arrow, the <100> direction). Moreover, no disturbance from domain wall was observed. The Ni cross-sectional lamella is thus composed of one single domain structure.

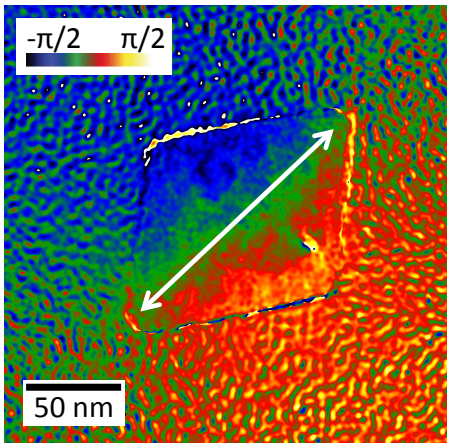


Figure 4.11 Magnetic phase shift image of a Ni cross section sample.

As a matter of fact, the thickness of the lamella is only about 80-100 nm, which is comparable to the length of the short diagonal. Hence, the cross section can be approximated to an ellipsoid. According to Hubert and Schäfer [134], the demagnetizing factor along the longer diagonal is $N_c = 0.04$. With $N_a = N_b = \frac{1}{2}(1 - N_c) = 0.48$, the shape anisotropy constant can be calculated from equation (1.28) as

$$K_s = \frac{1}{2}(N_a - N_c)M^2 = 5.175 \times 10^4 \text{ erg/cm}^3.$$

The extra energy cost for the magnetization along the <100> direction (rather than the easy axis <111>) is (Table 1.1)

$$\Delta e_{mc} = e_{mc(100)} - e_{mc(111)} = -\frac{K_1}{3} - \frac{K_2}{27} = 1.593\times10^4\ \mathrm{erg/cm^3}.$$

In this case, the shape anisotropy is slightly higher than the crystal anisotropy. The magnetization is thus aligned to the direction of the longer diagonal to reduce the demagnetization energy of the magnet.

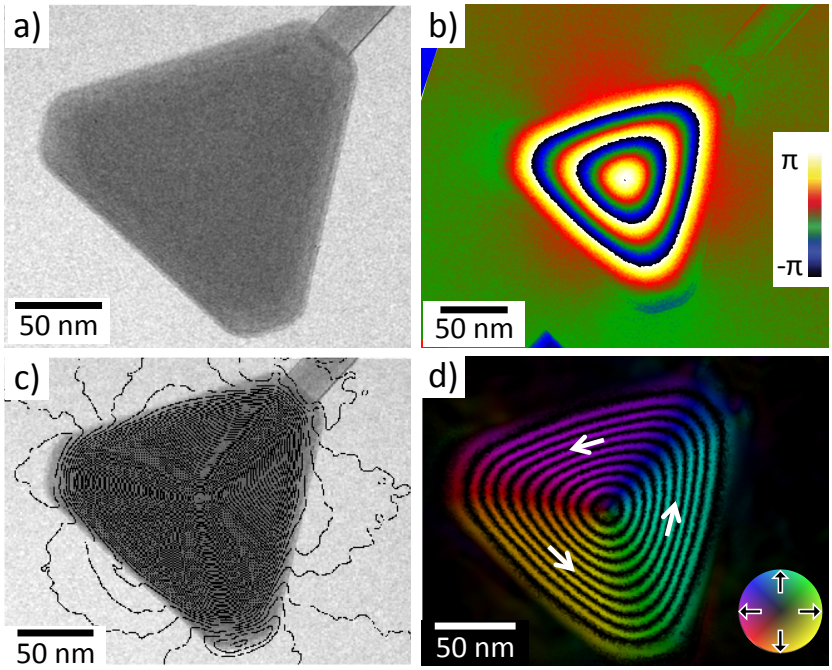


Figure 4.12 Electron holography results of a Co platelet: (a) amplitude image; (b) MAG phase shift; (c) MAG phase contour overlaid with the amplitude image showing the in plane magnetic induction, the spacing of the contour is 0.21 radians; (d) Magnetic flux lines calculated as the cosine of 4 times the MAG contribution to the measured phase shift. A low pass filter was applied to suppress the high frequency noise. The magnetization direction is marked by the white arrow.

The situation is different for platelets with higher symmetry. The electron holography results on a Co platelet are shown in Figure 4.12. The platelet is a truncated-triangle with a 3-fold symmetry as can be inferred from the amplitude image (Figure 4.12-a). The average length of the three longer sides is 150±4 nm. The vortex state observed in the MAG phase shift image (Figure 4.12-b) is understood as due to the high symmetrical shape of the platelet. Larger phase shift is obtained as one moves towards the center of the platelet. The phase shift is well confined within the platelet (since the vortex state is a stray field free or flux closure state), with only a few weak phase shift detected outside the platelet area. The induction lines (Figure 4.12-c) and the magnetic flux lines (Figure 4.12-d) indicate the presence of a magnetic vortex in the platelet. With the absence of external field, the center of the vortex lies on the central point of the rotational symmetry of the platelet. The vortex state was stabilized by the “round” truncated

edges. The sharp angles of the triangle are not favorable for the vortex state due to the high exchange energy they introduced [147].

For large platelets that are not highly symmetric, multi-domain structures were observed instead. Figure 4.13 shows the Lorentz microscope image of such a platelet. The Co platelet exhibited a closure multi-domain structure with its domain walls (bright and dark lines) highlighted by the red dashed lines. The dimension of the platelet is very different from that of a whisker. The width of the platelet is 400±10 nm, its length is 1.2±0.02 μm. The magnetostatic energy of the single domain state of the platelet, estimated with equation (1.31), is about 39.2 erg/cm, while the domain wall (total length 2.5±0.5 μm) energy of the closure domain state in Figure 4.13, estimated with equation (1.33), is only about $3.28\times10^{-4}$ erg/cm. The magnetostatic energy of the single domain structure is hence more than 5 orders of magnitude higher than the domain wall energy of the multi-domain structure. It seems that, unlike whiskers, the single domain structure is not favored for platelets with large surface area and small aspect ratio, nor is the vortex state if the platelet is not highly symmetric, the most stable state in this case is thus the closure multi domain structure.

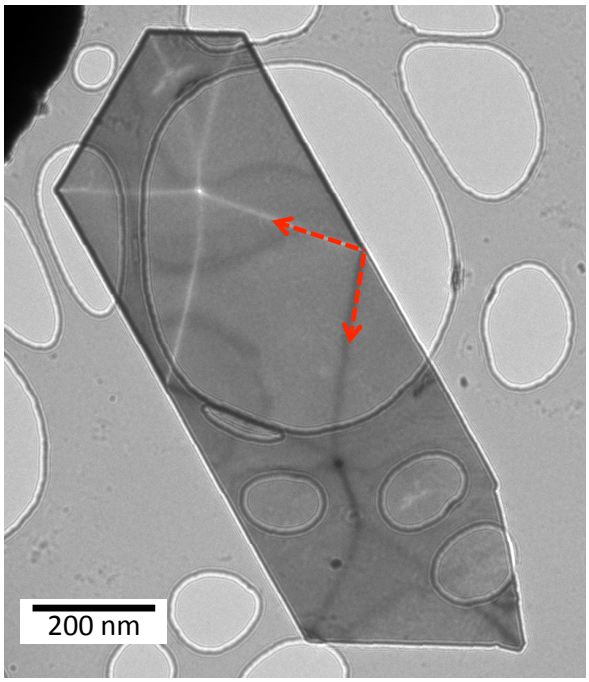


Figure 4.13 Lorentz microscope image (2mm under-focus) of a Co platelet with closure multi-domain structure. The bright and dark lines are the domain walls, and are highlighted by the red dashed lines.

I*n situ* Lorentz microscope experiments showed that the magnetic platelets were perfect candidates to study the magnetic skyrmion phenomenon. Increasing the external magnetic field perpendicular to the surface plane of the platelet changed the initial multi domain structures to helical state before breaking them into magnetic dots in skyrmion

state. The in plane magnetization then completely vanished above a certain point, the platelet became thus a single domain structure with magnetization aligned with the direction of the external field. The entire process can be reversed by returning the external field back to zero (Figure 4.14).

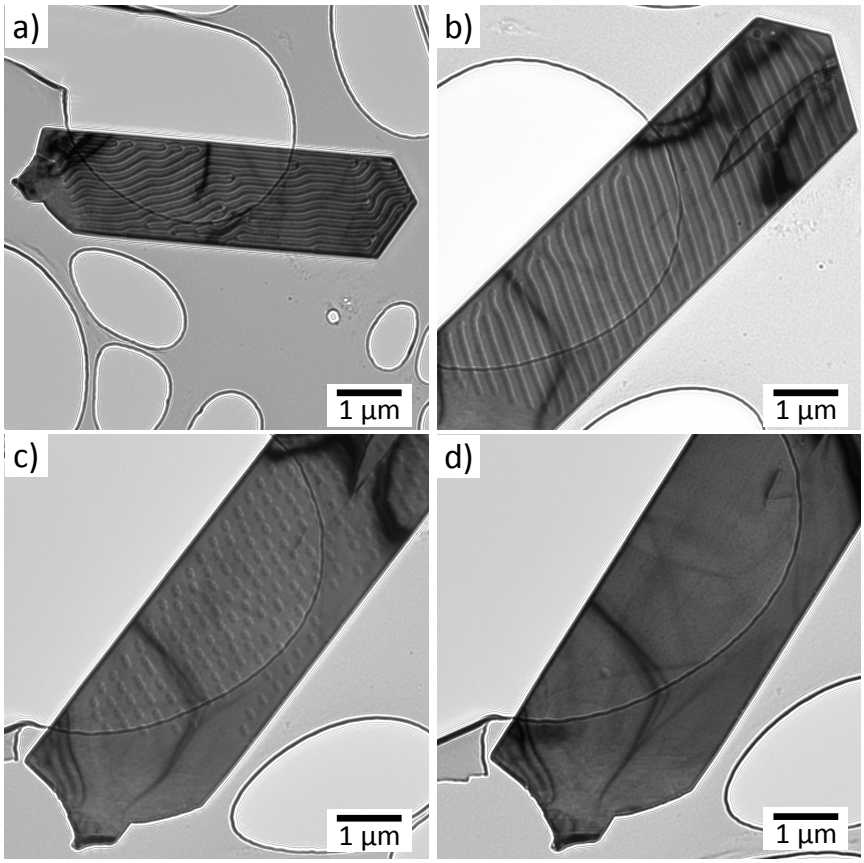


Figure 4.14 *In situ* Lorentz microscopy of a Co platelet under external magnetic field from the objective lens. The perpendicular component of the magnetic field was increased by tilting the specimen holder. The tilt angle were a) 0.1° (b) 36.48° (c) 42.29° (d) 46.12°. All the images were taken with an under-focus of 1 mm.

Finally, preliminary trials have been carried out to create a domain wall in the whisker. It has been explained in section 2.4 and that the magnetization reversal of the specimen can be achieved by tilting the specimen while applying a current on the objective lens. This is shown in Figure 4.15-a and -b on a Co whisker with diameter of 150±5 nm. The whisker was saturated in opposite directions by tilting it from -60° to +60° under 0.8 T magnetic field applied by the objective lens. The opposite magnetization directions can be verified from the opposite distributions of the Fresnel fringes on the two images. By slowly changing the tilt angle (to 22°) and the strength of the magnetic (to 1.0T), it is possible to create a 180° domain wall (red arrow) inside the whisker, as demonstrated in Figure 4.15-c, with a projected wall width of about 500±10 nm. The magnetization on the two sides of the domain wall is in opposite directions (evidenced again by the Fres-

nel fringes). An in-focus image of the whisker (Figure 4.15-d) is also shown as a reference for the position of the Fresnel fringes. This trial shows the possibility to control the domain wall propagation by manipulating the magnetic field, which can be proven interesting for many electronic applications [200,201]. The thickness of the domain wall is much larger than the theoretical value (72 nm, eq. (1.34)), which is attributed to the high shape anisotropy energy of the whisker [202,203].

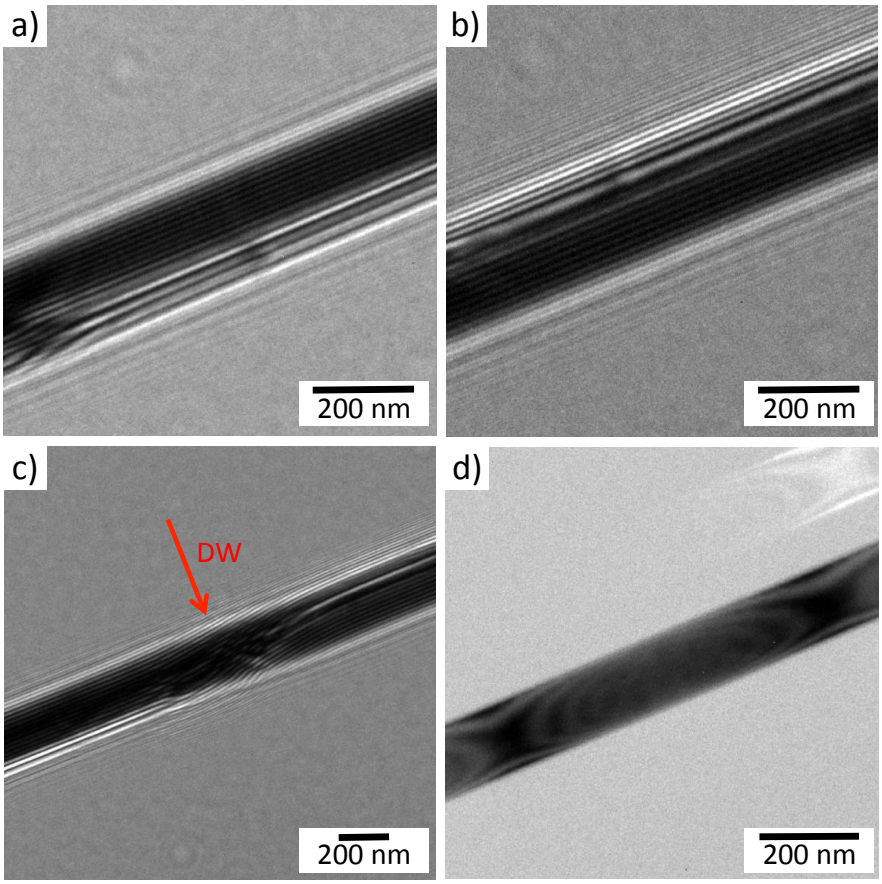


Figure 4.15 Lorentz microscopy images of a Co whisker: (a) after saturation with -60° tilting; (b) after saturation with +60° tilting; (c) Fresnel wall; (d) in focus.

In conclusion, the Co, Fe and Ni whiskers synthesized in this work were all single domain structures. The large shape anisotropy induced by the high aspect ratio of the whiskers forced the magnetization to be aligned along the direction of the whisker axis. The direction of the magnetization may change with the shape of the nanostructures. The cross section lamella cut from a Ni whisker had its magnetization direction along the direction of the longer diagonal. Vortex state was observed in highly symmetric small platelets. Larger platelets with lower level of symmetry, on the other hand, exhibited a multi-domain structure.

.

# 5 Discussion: Growth Mechanism and Process

The main task of this work is the study of the growth process of the nano-objects, including whiskers, blades and platelets. With a better understanding of the growth mechanism, the dimension of the nanostructures can be tailored to the need of the potential applications. The ideal situation would be, for instance, to achieve whisker-only growth under one condition and platelet-only growth under another. The results of this study are discussed below. The discussion is based on the microscopic structural analysis on samples with different growth conditions (growth temperature, substrate, mediating layer).

## 5.1 Conditions for Whisker Growth

The growth of the whiskers can be considered as an extreme case of 3D growth in thermodynamic equilibrium during thin film deposition. The 3D growth or Volmer-Weber growth occurs when $\gamma_s < \gamma_i + \gamma_f$, in which case the deposition material does not wet the substrate surface ($\theta > 0$). The whisker growth is thus dependent on the surface energy and the interface energy between the substrate and the deposited material. The surface and interface energies also affect the mobility of the adatoms (surface diffusion), which in turn determines the density and the size of the whiskers.

Surface heterogeneity plays an important role in the formation of nanostructures. The high aspect ratio of the whiskers, in particular, requires a highly selective nucleation [70]. Adatoms tend to congregate at sites of higher surface energy, *e.g.* at terraces, ledges and kinks (TLK model), before growing into stable nuclei. With more dangling bonds available in these areas, stronger bonds were formed between the adatoms and the substrate, leading to an increase in the density of stable nuclei. In this work, the preferred nucleation sites observed were steps [204] (terrace and ledges on graphite surfaces), surface contaminations (Mo and W wire), intrinsic lattice defects (vacancies in the amorphous C layer [205]), and artificial defects (FIB [70] or HIM etched pits).

The amorphous C layer was deposited via magnetron sputtering. Successful whisker growth was observed on substrates covered by amorphous C for most the materials concerned in this work, with the exception of Fe. The latter is explained by the low Fe-C interface energy [206] and the lowered surface energy of the amorphous C film after Fe incorporation [207]. The stable Fe-C bonding inhibits the diffusion of the Fe atoms on the C surface, therefore limiting the possibility of 3D growth. Fe whiskers were, however, obtained on STO substrates with a TiC layer. The amorphous TiC layer pro-

vides another bonding Fe-Ti for the Fe adatoms, in addition to the stable Fe-C. The different strength of the two bondings [208] results in inhomogeneous diffusion and nucleation of the Fe adatoms, which makes the growth of the whiskers possible. Only two growth directions (relative to the substrate) were observed for the Fe whiskers on STO (100) substrates (Figure 3.20-b). The growth directions are perpendicular to each other, which indicates that they are inherited directly from the STO substrate. This is particularly interesting as it implied that the nucleation sites in this case were not actually on the mediating layer itself (C or TiC) but rather on the exposed area (through the vacancies in the mediating layer) of the underlying substrate. Together, these provide two different perspectives to the role of the mediating layer. It limits the amount of nucleation site when there are too many (*e.g.* on STO) and supplies them when there are too few (*e.g.* on TEM grid).

Indeed, a high nucleation density is unfavorable for whisker growth as each whisker requires a minimum amount of materials due to their high aspect ratio, while the total supply is limited by the amount of the diffusing adatoms [68,209]. For instance, the high density of the Au nanoparticles (nucleation site for Ag) at the surface resulted in island-only growth for Ag deposition (Figure 3.7). The same was observed on graphite terraces with high density of defects (Figure 3.6).

Temperature and deposition rate also affect the nucleation and growth process of the whiskers. With the same amount of deposition, the length of the Cu whiskers grown on the TEM grids is longer at higher temperatures while their density is smaller (Figure 3.2). This is consistent with what was previously explained in section 1.3 for thin film deposition. Higher substrate temperature results in larger (1.13) but fewer nuclei (1.14). Higher deposition rate, on the other hand, would yield larger (1.15) and higher number of stable nuclei (1.17). The nucleation density has to be limited to have sustainable whisker (high aspect ratio) growth, the optimal growth parameter should thus be a combination of a high substrate temperature and a low deposition rate. There is, however, an upper limit to the substrate temperature. As the dwell time (1.6) and the diffusion length (1.10) of the adatoms both drop exponentially with increasing temperature, the effective deposition rate is significantly reduced at high temperatures due to the high desorption rate (1.7). The whisker growth can no longer be sustained under these conditions due to insufficient materials reaching the incorporation sites before being desorbed back into the vacuum.

The optimal whisker growth temperature was, from our experience, generally at about 60% of the melting temperature. The nominal deposition rate was chosen at 0.05 nm/s to allow whiskers to be grown in a reasonable amount of time. The actual growth rate of the whiskers varied as the result of different interface and surface (substrates or mediating layers) energies.

Finally, there is also a correlation between the surface roughness of the mediating C layer and the resulted whisker density, as has been demonstrated in a previous work from our group [69]. The whisker density is, in addition, influenced by the hybridization of the C layer. The amount of whisker obtained on HOPG increases with increasing sp3 hybridization ratio after annealing [165]. This is understood as due to the different surface energies between graphite and diamond [205] as well as their interface energies with metals [206].

## 5.2 Whisker Growth Mechanism: Incorporation Site

The equiaxed growth only results in structures of equilibrium crystal shape after nucleation. In this case typical adatoms are incorporated into the structure by nucleation on the structures surfaces, or by attachment at surface defects (steps, ledges or kinks). In order to obtain (one-dimensional) whisker structures, the equilibrium growth condition has to be broken with kinetic anisotropy, *i.e.* the axial growth needs to be much effective than the radial growth. This was thought to be achieved through the introduction of defects (*e.g.* screw dislocation, steps or impurities) or interfaces into the system. Since no screw dislocation was observed in the whiskers obtained in this work, the screw dislocation theory can be ruled out here. The only place where symmetry (for an equiaxed nucleus) is broken is the whisker/substrate interface. To achieve one-dimensional growth, the adatoms have to be incorporated into the interface. The interface can be coherent, incoherent or semi-coherent. Incoherent interfaces are regions with high density of vacancies and free bondings, while semi-coherent interfaces contain misfit dislocations. Therefore, interfaces are believed to be the effective diffusion paths [54,211] and nucleation site [212] for metal atoms. The much faster incorporation rate at the whisker/substrate interface than at the whisker surface is responsible for the kinetic anisotropy that leads to the high aspect ratio of the whisker. Diffusion at these interfaces can proceed with a mechanism that involves the creation and annihilation of vacancies because:
- The vacancy concentration at the interface is higher than the equilibrium concentration in the bulk.
- Adatoms can attach to a vacancy close to the surface at the triple line of whisker surface, substrate surface and their interface.
- By this vacancy annihilation, the vacancy concentration is lowered to below the equilibrium concentration for whisker surface/interface. The vacancies can then migrate from the interface towards the triple line and by doing so move the attached adatoms into the interface area.

Most likely, the vacancy mechanism does not apply in the case of coherent interfaces as the perfect matching between the lattices leave no defects at the interface. The role of the interface is even more complicated if alloy is being formed between the deposited material and the substrate. For instance, it has been reported that the silicide formation with the Si substrate makes the Fe-Si and Ni-Si interface more reactive [213]. The

intrinsic defects in the Si substrate allow the diffusion of the metal atoms into the Si lattice, which in turn remove the Si atoms from the lattice to form silicide at the interface. This interdiffusion at the interface makes the interface a high-energy region with high density of defects (interstitial defects and vacancies). This will increase the diffusion of adatoms on the substrate surface towards the interface and their incorporate into the silicide whisker.

Our experimental observations (Figure 3.3-d) revealed the root of the nano-objects (platelets and whiskers) to be faceted. It was further pointed out by Kappel [167] that, except for the low index facets, the root of the whiskers is composed of many small $\{11\ell\}$ crystal planes. The mechanism behind the stabilization of these small facets remains obscure. The small $\{11\ell\}$ facets are among those undergoing a roughening transition upon heating, and provide high density of steps and vacancies for adatom incorporation [214]. This will enable the proposed incorporation mechanism. Moreover, the majority of the adatoms are those impinged directly at the substrate surface. The adatoms on the substrate surface tend to diffuse towards the whisker root and contribute to the axial growth of the whisker. Therefore, the root growth mechanism is more effective than the tip growth and the radial growth of the whiskers. There exists probably a delicate balance of adatom diffusion towards the whisker root, the incorporation into the interface, the vacancy formation and diffusion rate and the adatom diffusion in the interface. The whisker root would be overloaded, if more adatoms arrive than the root site can incorporate. The aggregation of adatoms without incorporation into annihilated vacancies at whisker root would result in the growth of islands. Finally, it has been reported that the oxide layer surrounding the whiskers surface can also impede the whisker growth by preventing the adatoms from diffusing into the whisker root [215].

If the whisker-substrate interface energy or the adatoms-substrate bonding energy is too high or the vacancy density at the interface is too low, the root incorporation of adatoms may be hindered. The growth of the whisker then relies mainly on the adatoms diffusing along the whisker surface. It is still under debate as to why the whiskers grow preferentially at the tip rather than on the sidewalls. The tip growth may be favored for two reasons: first, the tip contains higher density of defective facet edges, which are spontaneously formed at elevated growth temperatures due to the high entropy term in surface free energy. These defects are energetically favored sites for adatom nucleation [212,216,217]. Second, axial growth (tip or root) is more visible for a given amount of adatoms compared to radial growth (sidewall) because of the much smaller surface area. As a simple estimation, for a whisker of 50 nm wide and 10 μm long, the number of atoms for one atomic layer growth on the sidewall is equivalent to 400 atomic layer growth on the tip.

In the case of whisker growth with more than one material, one also has to consider the interface between the different deposited materials. In principle, adatom incorporation

at the heterojunction is negligible, mainly because the interface of an epitaxial growth is usually coherent with very few defects. In contrast, when the interface is highly defective (*e.g.* contains kink [218]), whisker growth can also occur at the heterojunction.

The synthesis of various whisker heterostructures has provided invaluable insights to the whisker growth process, especially on the identification of the incorporation site. (Figure 3.30) The different incorporation sites (tip, root and side surface) were experimentally observed by the use of different substrate and/or deposited materials.

In the case of Cu-Fe whisker heterostructures on an Au TEM grid with a mediating C layer, the growth of the Fe segment was observed at the tip of the Cu whisker (Figure 3.32). Although the root is generally considered as the primary site for most growth processes, tip growth is observed when adatom incorporation at root is not possible. Indeed, root growth in this case would require the incorporation of Fe adatoms at the whisker-C interface, which has been proven impossible in our experiment of growing Fe whiskers directly on TEM grid with lacey C film. Moreover, only the adatoms directly impinged on the whisker sidewall can diffuse to the tip due to the inhibited diffusion of Fe on C surface (stable Fe-C bonding), which explains the much shorter Fe segment found on top of the Cu whiskers despite the same nominal film thickness.

When incorporation at root is allowed, the majority of the adatoms would end up in the root sink, making the tip growth almost unnoticeable. This is what was observed when the same Cu-Fe deposition took place on a Si substrate. The growth of the Fe segment was obtained only at the root of the Cu whisker (Figure 3.34). The growth scenario was completely different as the two metals formed their respective silicide with the Si atoms. Taking into account the successful synthesis (Figure 3.23) of Fe silicide whiskers directly on TiC (and not C) mediating Si substrates, the role of Cu in this case can be understood as to provide either inhomogeneous bonding sites (replacing Ti) or vacancy sites (formed during the growth of $Cu_3Si$ whiskers) for the root incorporation of the Fe adatoms. The presence of Cu (and Si) altered the primary incorporation site of the whisker growth. The same was observed for the growth of Cu-Ni (Figure 3.36) and Cu-Ni-Si (Figure 3.37) whisker heterostructures.

The less visible radial growth (slight diameter expansion of the whiskers) is perhaps more evident in the growth of whisker heterostructures by the presence of the core-shell structures. The radial growth of the whiskers was mostly attributed to the direct atom impingement on the whisker sidewalls [70]. Only radial growth was observed (Figure 3.41) when the deposition order of Cu and Fe was reversed. The absence of root incorporation was explained by the more stable binding of the Fe atoms with the substrate than the Cu atoms while the absence of tip incorporation was explained by insufficient Cu diffusion on the Fe whisker sidewall. Similar observation was made when growing

Ni-Ag whisker heterostructures (Figure 3.42). Finally, the tip growth and the root growth can be activated at the same time as was demonstrated during the growth of Au-Ni whisker heterostructures (Figure 3.38).

## 5.3 Defects, Shape and Oxidation

Although the specific growth conditions for whiskers, platelets, blades and islands are yet to be identified, it was apparent that the crystallographic orientations are different for different nano-objects from the TEM measurements. The islands are usually poly-crystalline while the whiskers and platelets are mostly single crystal with the exception of the Co whiskers due to their complex phase transformation. No screw dislocation was observed in any of the whiskers synthesized in this work. Twin structures were occasionally found in Ni and Co whiskers. The coherent boundary of the Σ3 $(1\bar{1}1)[110]$ twin was found to be parallel to the whisker axis. The energy of the coherent twin boundaries is small, about half of the value of the stacking faults, and decreases with increasing temperature [219]. In fact, the existence of the twin boundary can even promote the nucleation and growth of the whiskers. It has been previously demonstrated that the nucleation barrier was lowered at the twin plane re-entrant groove [56]. The diffusion of adatoms towards the twin boundary is thus energetically favored, which then contributes to the axial growth of the whiskers.

In principle, the cross-sectional shapes of the whiskers obey the Wulff theorem, but are elongated along the direction of the whisker axis (Figure 3.3, Figure 3.11 and Figure 3.14). For the minimization of the total free surface energy, the surface facets are low index crystal planes with low surface energies. A transition of the cross-sectional shape from octagonal to square was observed on the $FeSi_2$ whiskers (Figure 3.26). The transition was probably linked to kinetic effects. The kinetic effect is also responsible for the high aspect ratio of the whiskers. The roughly equiaxed equilibrium crystal (Wulff) shape is broken by the kinetic anisotropy, which caused a much faster axial growth rate than the radial one [54]. A similar kinetic effect can be used to explain the shape transition. The freshly grown part near the root of the whisker (root growth) has the equilibrium cross-sectional shape of an octagon. The four facets with faster kinetic growth rate vanished with the extensive radial overgrowth, resulting in a square cross section. This also explains why the octagonal part has a much smaller diameter (no radial overgrowth) compared to the square part.

An oxide layer was observed covering the surface of all the metal whiskers (except Ag) synthesized in this work. The thin layer of oxide (typical about 5 nm) was probably amorphous when they were first formed upon exposing the whiskers to ambient condition. The epitaxial crystalline oxide observed with TEM was likely to be related to the

effect of the electron beam. No further oxidation was observed after prolonged exposure to the electron beam or further heating. It would seem that the whisker structures were protected against oxidation and corrosion by the thin oxide surface layer [220].

# 6 Summary

In this work, whiskers of IB, VIII metals and their alloys were synthesized using physical vapor deposition. Their structural, morphological and magnetic properties were studied by electron microscopy techniques. A summary of some of the specimens is shown in Table 6.1.

Table 6.1 Crystal structure, axis and cross section of the whiskers.

| Material | Crystal structure | Whisker axis | Cross section |
|---|---|---|---|
| Cu | FCC | <110> | 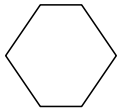 |
| $Cu_3Si$ | HCP | <0001> | |
| Ag | FCC | <110> | 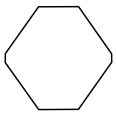 |
| Ni | FCC | <110> | 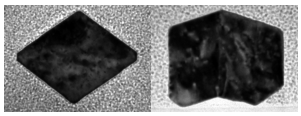 |
| Co | FCC/HCP | <110>/<1210> | 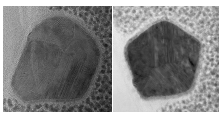 |
| Fe | BCC | <100> | 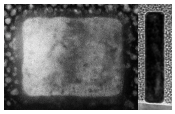 |
| $FeSi_2$ | Tetragonal | [100]/[001] | 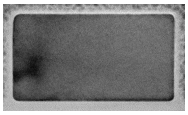 |
| Cu-Fe | FCC-BCC | <110>-<100> | |
| $Cu_3Si$-$FeSi_2$ | HCP-Orthorhombic | <0001>-<100> | 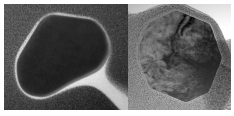 |
| Au-Ni | FCC-FCC | <110>-<110> | |

The Cu, Ag and Ni whiskers were all FCC single crystal structures with the whisker axis along the <110> crystallographic directions. Their cross-sectional shape followed what was predicted by the Wulff theorem. Depending on the surface energy of the crystal planes, the cross-sectional shape can be either quasi-hexagonal or quasi-octagonal. The hexagonal cross section of the Cu whiskers was constructed by the {111} and the {100} planes. The octagonal cross section of the Ni and Ag whiskers contains in addition two {110} planes. The presence of the {110} planes might be explained simply by their relatively low energy, but was more likely to be related to kinetic anisotropy or roughening transitions. The former was the direct result of the non-equilibrium growth conditions and the latter was responsible for breaking large flat surfaces to smaller rugged ones. A Σ3 $(1\bar{1}1)[110]$ twin boundary was found in some of the Ni whiskers, separating the cross section into two almost mirrored halves. The low energy coherent twin is thought to have promoted the whisker growth process by lowering the nucleation barrier.

The Fe whiskers were single crystal BCC structure growing along the <100> directions. Their rectangular cross section was surrounded by the {110} planes. The variation in aspect ratio between the cross sections of different whiskers was explained by kinetic anisotropy.

The crystal structure of the Co whiskers was complicated by the inevitable phase transformation occurred at 430 °C. The Co whiskers synthesized in this work were FCC, HCP or a mixture of both. FCC was found to be the more stable phase, mostly because of the slightly smaller surface energy. The cross section of the FCC Co whiskers was a pentagon joined by 5 twin structures. HCP crystals can often be observed in the FCC whiskers, under the form of microtwins. They are the result of the fast kinetic growth and of the incomplete phase transformation during the cool-down process. Post-mortem analysis of the whiskers indicated that the HCP phase could be promoted by applying a tensile stress along the direction of whisker axis.

Silicide whiskers were obtained by performing the growth procedures on C mediated Si substrates. The $Cu_3Si$ whiskers were HCP single crystals with whisker axis parallel to the <0001> directions. The $FeSi_2$ whiskers were tetragonal structures with two different growth directions, <100> and <001>. The root part of the $FeSi_2$ whiskers has a smaller diameter and a different shape compared to the rest, due to the lack of radial overgrowth. The growth of the silicide whiskers was partially driven by the vacancies at the whisker-substrate interface, left behind by the diffusion of the Si atoms along the whiskers. The vacancies were also responsible for the diffusion of Fe adatoms into the substrate lattice.

Several whisker heterostructures were synthesized in this work. By combining different materials, the whisker properties can be tuned to the need of different applications. Both

axial (Cu-Fe, Au-Ni) and radial (Fe-Cu, Ni-Ag) heterostructures were obtained. The morphology of the final structure depends on the deposition sequence and the growth temperature.

The magnetic domain structure of the nanostructures was studied with electron holography. Despite the sometimes observed stacking faults and twin boundaries, the magnetic whiskers in this work (Ni, Fe, Co) were all single domain structures with magnetization along the whisker axis. The magnetization direction was dictated by the predominating shape anisotropy (rather than the magnetocrystalline anisotropy), which itself is the result of the high aspect ratio of the whiskers. The direction of the magnetization may change with the shape of the nanostructures. The cross section lamella cut from a Ni whisker had its magnetization direction along the direction of the longer diagonal. Vortex state was observed in highly symmetric small platelets. Larger platelets with lower level of symmetry, on the other hand, exhibited a multi-domain structure.

The growth process has been further studied in this work. The nucleation and growth of the whiskers were strongly affected by the surface energies as well as the interface energy of the substrate and the whisker. The nucleation took place preferentially on the heterogeneities at the substrate surface as it lowered the total free energy of the system. The surface heterogeneities observed in this work includes the intrinsic defects (the vacancies in the substrates or in the mediating layers), the contaminations (W and Mo wires), the ledges (graphite) and artificial defects (HIM holes). The density and size of whiskers can be tuned by controlling the growth temperature and the density of defects on the substrate surface.

Although the exact conditions for growing whiskers and platelets are still not clear, the incorporation sites for the whisker growth have been identified experimentally from the whisker heterostructures. Both root and tip growth were observed. Root growth was the default mode of growth, since the majority of the adatoms were found at the surface. When incorporation at the root site is not possible, tip growth was observed instead. Whisker segments by tip growth were often shorter as it was mainly fueled by the adatoms directly impinged on the whisker sidewall. The axial elongation was accompanied by the inevitable albeit often slight diameter expansion of the whiskers.

A thin oxide layer (≈ 5 nm) was observed covering the surface of all the metal (but Ag) whiskers synthesized in this work. The layer was usually composed of amorphous metal oxide except for $FeSi_2$ whiskers, in which case the oxide layer was made of $SiO_2$ due to its relatively lower surface energy. The oxide layer was stable enough to prevent any further oxidation of the whiskers even after years of exposure to ambient conditions.

There exist certain limitations to the results presented in this work. First, the substrate temperature was usually pre-calibrated and might deviate over time. The uncertainty

was about 20-50 °C. Second, the conventional TEM collects projected data, and is thus not sensitive to the information along the direction of the electron beam. In order to determine the orientation of the whiskers and platelets, it is necessary to tilt the specimen to different zone axes, which is not always possible depending on the setup. Last but not least, statistical analysis (*i.e.* averaged results on a large surface area) is difficult due to the small Field of View of the TEM.

# Bibliography


[1] R. Feynman, Caltech Eng. Sci. **23**, 22 (1960).

[2] N. Taniguch, in *Proc. Int. Conf. Prod. Eng.* (1974), pp. 18–23.

[3] E. Drexler, *Engines of Creation: The Coming Era of Nanotechnology* (1987).

[4] G. Binnig and H. Rohrer, IBM J. Res. Dev. **30**, 355 (1986).

[5] E. T. Thostenson, Z. Ren, and T. W. Chou, Compos. Sci. Technol. **61**, 1899 (2001).

[6] P. Qi, O. Vermesh, M. Grecu, A. Javey, Q. Wang, H. Dai, S. Peng, and K. J. Cho, Nano Lett. **3**, 347 (2003).

[7] J. Wang, Electroanalysis **17**, 7 (2005).

[8] J. N. Coleman, U. Khan, W. J. Blau, and Y. K. Gun'ko, Carbon **44**, 1624 (2006).

[9] K. H. An, S. Y. Jeong, H. R. Hwang, and Y. H. Lee, Adv. Mater. **16**, 1005 (2004).

[10] A. Dmitriev, C. Hägglund, S. Chen, H. Fredriksson, T. Pakizeh, M. Käll, and D. S. Sutherland, Nano Lett. **8**, 3893 (2008).

[11] J.-M. Tarascon, P. Poizot, S. Laruelle, S. Grugeon, and L. Dupont, Nature **407**, 496 (2000).

[12] Y. Cui, Q. Wei, H. Park, and C. M. Lieber, Science **293**, 1289 (2001).

[13] A. Balandin and K. L. Wang, Phys. Rev. B **58**, 1544 (1998).

[14] A. A. Balandin, S. Ghosh, W. Bao, I. Calizo, D. Teweldebrhan, F. Miao, and C. N. Lau, Nano Lett. **8**, 902 (2008).

[15] T. Takagahara and K. Takeda, Phys. Rev. B **46**, 15578 (1992).

[16] L. Vayssieres, C. Sathe, S. M. Butorin, D. K. Shuh, J. Nordgren, and J. Guo, Adv. Mater. **17**, 2320 (2005).

[17] X. Y. Zhao, C. M. Wei, L. Yang, and M. Y. Chou, Phys. Rev. Lett. **92**, 236805 (2004).

[18] E. Arzt, Acta Mater. **46**, 5611 (1998).

[19] M. A. Meyers, A. Mishra, and D. J. Benson, Prog. Mater. Sci. **51**, 427 (2006).

[20] N. I. Kovtyukhova and T. E. Mallouk, Chem. - A Eur. J. **8**, 4354 (2002).

[21] P. Lee, J. Lee, H. Lee, J. Yeo, S. Hong, K. H. Nam, D. Lee, S. S. Lee, and S. H. Ko, Adv. Mater. **24**, 3326 (2012).

[22] G. Agricola, *De Natura Fossilium Libri X. von G. Agricola* (Deutscher Verlag

der Wissenschaften, 1546).

[23] J. Gerhard, *Decas Quaestionum Physico-Chymicarium de Metallis* (Tübingen, 1643).

[24] L. Ercker, *Beschreibung Allerfürnemisten Mineralischen Ertzt, Unnd Bergwercksarten, Wie Dieselbigen, Unnd Eine Jede Insonder- Heit, Der Natur Und Eigenschafft Nach, Auff Alle Metale Probirt . . . In Fünff Bücher Verfast* (Georg Schwartz, Prag, 1574).

[25] J. F. Henckel, *Flora Saturnizans, Die Verwandschaft Des Pflanzen Mit Dem Mineralreich, Nach Der Naturalhistorie Und Chymie Aus Vielen Anmerkungen Und Proben; Nebst Einem Anhang von Kali Geniculato Germanorum Oder Gegliederten Saltzkra* (In der Grossischen Handlung, Leipzig, 1755).

[26] G. Bischof, Ann. Der Phys. Und Chemie, Band LX 285 (1843).

[27] W. Ostwald, Kolloid-Zeitschrift **102**, 35 (1943).

[28] W. Ostwald, Kolloid-Zeitschrift **102**, 181 (1943).

[29] S. S. Brenner, Acta Metall. **4**, 62 (1956).

[30] S. S. Brenner, The Growth and Mechanical Properties of Metal Whiskers, Rensselaer Polytechnic Institute, 1957.

[31] S. S. Brenner, Science **128**, (1958).

[32] F. C. Frank, Discuss. Faraday Soc. **5**, 48 (1949).

[33] M. O. Peach, J. Appl. Phys. **23**, 1401 (1952).

[34] S. E. Koonce and S. M. Arnold, J. Appl. Phys. **24**, 365 (1953).

[35] J. Eshelby, Phys. Rev. **91**, 755 (1953).

[36] F. C. Frank, Philos. Mag. Ser. 7 **44**, 854 (1953).

[37] J. Franks, Nature **177**, 984 (1956).

[38] J. Franks, Acta Metall. **6**, 103 (1958).

[39] S. Amelinckx, W. Bontinck, W. Dekeyser, and F. Seitz, Philos. Mag. **2**, 355 (1957).

[40] G. W. Sears, Acta Metall. **1**, 457 (1953).

[41] G. W. Sears, Acta Metall. **3**, 367 (1955).

[42] G. W. Sears, Ann. N. Y. Acad. Sci. **65**, 388 (1957).

[43] G. W. Sears, J. Chem. Phys. **33**, 563 (1960).

[44] S. S. Brenner and G. W. Sears, Acta Metall. **4**, 268 (1956).

[45] C. Herring and J. Galt, Phys. Rev. **85**, 1060 (1952).

[46] M. Sobiech, M. Wohlschlögel, U. Welzel, E. J. Mittemeijer, W. Hügel, A. Seekamp, W. Liu, and G. E. Ice, Appl. Phys. Lett. **94**, 25 (2009).

[47] M. Sobiech, U. Welzel, E. J. Mittemeijer, W. Hügel, and A. Seekamp, Appl. Phys. Lett. **93**, 26 (2008).

[48] P. Sarobol, J. E. Blendell, and C. A. Handwerker, Acta Mater. **61**, 1991 (2013).

[49] S. J. Kim, E. A. Stach, and C. A. Handwerker, Appl. Phys. Lett. **96**, 144101 (2010).

[50] S. J. Kim, E. A. Stach, and C. A. Handwerker, Thin Solid Films **520**, 6189 (2012).

[51] P. Sarobol, Y. Wang, W. H. Chen, A. E. Pedigo, J. P. Koppes, J. E. Blendell, and C. A. Handwerker, JOM **65**, 1350 (2013).

[52] V. G. Karpov, Phys. Rev. Appl. **1**, 44001 (2014).

[53] D. Niraula and V. G. Karpov, J. Appl. Phys. **118**, 205301 (2015).

[54] D. Amram, O. Kovalenko, L. Klinger, and E. Rabkin, Scr. Mater. **109**, 44 (2015).

[55] J. W. Faust and H. F. John, J. Phys. Chem. Solids **25**, 1407 (1964).

[56] A. D. Gamalski, P. W. Voorhees, C. Ducati, R. Sharma, and S. Hofmann, Nano Lett. **14**, 1288 (2014).

[57] J. A. Venables, *Introduction to Surface and Thin Film Processes* (Cambridge University Press, 2000).

[58] G. W. Sears, Acta Metall. **3**, 361 (1955).

[59] V. Ruth and J. P. Hirth, J. Chem. Phys. **41**, 3139 (1964).

[60] R. Gomer, J. Chem. Phys. **28**, 457 (1958).

[61] W. Dittmar and K. Neumann, Zeitschrift Für Elektrochemie, Berichte Der Bunsengesellschaft Für Phys. Chemie **64**, 297 (1960).

[62] J. M. Blakely and K. A. Jackson, J. Chem. Phys. **37**, 428 (1962).

[63] J. P. Hirth and G. M. Pound, *Condensation and Evaporation-Nucleation and Grwoth Processes* (Macmillan, New York, 1963).

[64] J. P. Hirth and F. C. Frank, Philos. Mag. **3**, 1110 (1958).

[65] W. W. Webb, R. D. Dragsdorf, and W. D. Forgeng, Phys. Rev. **108**, 498 (1957).

[66] W. W. Webb, J. Appl. Phys. **33**, 1961 (1962).

[67] G. W. Sears and R. V. Coleman, J. Chem. Phys. **25**, 635 (1956).

[68] G. Richter, K. Hillerich, D. S. Gianola, R. Mönig, O. Kraft, and C. a Volkert, Nano Lett. **9**, 3048 (2009).

[69] K. Hillerich, Metallische Whisker: Wachstum Und Eigenschaften, Universität Stuttgart, 2007.

[70] L. Weissmayer, Keimbildung Und Wachstum Metallischer Whisker, University Stuttgart, 2013.

[71] D. A. Mortimer and M. Nicholas, J. Mater. Sci. **5**, 149 (1970).

[72] D. A. Mortimer and M. Nicholas, J. Mater. Sci. **8**, 640 (1973).

[73] J. R. Arthur and A. Y. Cho, Surf. Sci. **36**, 641 (1973).

[74] B. Lewis and M. R. Jordan, Thin Solid Films **6**, 1 (1970).

[75] W. F. Egelhoff and G. G. Tibbetts, Phys. Rev. B **19**, 5028 (1979).

[76] L. Mohaddes-Ardabili, H. Zheng, Q. Zhan, S. Y. Yang, R. Ramesh, L. Salamanca-Riba, M. Wuttig, S. B. Ogale, and X. Pan, Appl. Phys. Lett. **87**, 1 (2005).

[77] T. Hayashi, T. Ohno, S. Yatsuya, and R. Uyeda, Jpn. J. Appl. Phys. **16**, 705 (1977).

[78] M. D. Uchic, D. M. Dimiduk, J. N. Florando, and W. D. Nix, Science **305**, 986 (2004).

[79] Y. Hanaoka, K. Hinode, K. Takeda, and D. Kodama, Mater. Trans. **43**, 1621 (2002).

[80] Q. Huang, Size and Surface Effects on the Electrical Properties of Metallic Nanowires, University of Illinois at Chicago, 2008.

[81] E. Stefan Kooij and B. Poelsema, Phys. Chem. Chem. Phys. **8**, 3349 (2006).

[82] D. Stichtenoth, C. Ronning, T. Niermann, L. Wischmeier, T. Voss, C. J. Chien, P. C. Chang, and J. G. Lu, Nanotechnology **18**, 435701 (2007).

[83] L. Sun, Y. Hao, C. L. Chien, and P. C. Searson, IBM J. Res. Dev. **49**, 79 (2005).

[84] L. Sun, P. C. Searson, and C. L. Chien, Phys. Rev. B **61**, R6463 (2000).

[85] M. Hanson, O. Kazakova, P. Blomqvist, R. Wäppling, and B. Nilsson, Phys. Rev. B **66**, 144419 (2002).

[86] M. Respaud, J. M. Broto, H. Rakoto, A. R. Fert, L. Thomas, B. Barbara, M. Verelst, E. Snoeck, P. Lecante, A. Mosset, J. Osuna, T. Ould Ely, C. Amiens, and B. Chaudret, Phys. Rev. B **57**, 2925 (1998).

[87] P. Briot, A. Auroux, D. Jones, and M. Primet, Appl. Catal. **59**, 141 (1990).

[88] J. T. Miller, A. J. Kropf, Y. Zha, J. R. Regalbuto, L. Delannoy, C. Louis, E. Bus, and J. A. van Bokhoven, J. Catal. **240**, 222 (2006).

[89] G. Cheng, T. H. Chang, Q. Qin, H. Huang, and Y. Zhu, Nano Lett. **14**, 754 (2014).

[90] W. D. Nix, Metall. Trans. A **20**, 2217 (1989).

[91] P. A. Gruber, C. Solenthaler, E. Arzt, and R. Spolenak, Acta Mater. **56**, 1876 (2008).

[92] C. A. Volkert and E. T. Lilleodden, Philos. Mag. **86**, 5567 (2006).

[93] C. P. Frick, B. G. Clark, S. Orso, A. S. Schneider, and E. Arzt, Mater. Sci. Eng. A **489**, 319 (2008).

[94] A. Sedlmayr, Experimental Investigations of Deformation Pathways in Nanowires, Karlsruher Institute of Technology, 2012.

[95] C. Ensslen, O. Kraft, R. Mönig, and A. Materials, **4**, 83 (2014).

[96] C. Schopf, M. Schamel, H. P. Strunk, and G. Richter, Adv. Eng. Mater. **14**, 975 (2012).

[97] A. Sedlmayr, E. Bitzek, D. S. Gianola, G. Richter, R. Mönig, and O. Kraft, Acta Mater. **60**, 3985 (2012).

[98] L. G. Machado and M. A. Savi, Brazilian J. Med. Biol. Res. **36**, 683 (2003).

[99] I. Gotman, J. Endourol. **11**, 383 (1997).

[100] J. Van Humbeeck, J. Alloys Compd. **355**, 58 (2003).

[101] G. Song, N. Ma, and H. N. Li, Eng. Struct. **28**, 1266 (2006).

[102] W. Betteridge, Prog. Mater. Sci. **24**, 51 (1980).

[103] J. W. Christian, Proc. R. Soc. A Math. Phys. Eng. Sci. **206**, 51 (1951).

[104] J. G. Wright, Thin Solid Films **22**, 197 (1974).

[105] O. S. Edwards and H. Lipson, Proc. R. Soc. A Math. Phys. Eng. Sci. **180**, 268 (1942).

[106] E. A. Owen and D. M. Jones, Proc. Phys. Soc. Sect. B **67**, 456 (1954).

[107] J. E. Fisher, Thin Solid Films **5**, 53 (1970).

[108] H. T. Hesemann, P. Müllner, O. Kraft, D. Nowak, S. P. Baker, K. Finkelstein, and E. Arzt, Scr. Mater. **48**, 1129 (2003).

[109] H. T. Hesemann, P. Müllner, O. Kraft, and E. Arzt, MRS Proc. **594**, 219 (2011).

[110] F. E. Luborsky, E. F. Koch, and C. R. Morelock, J. Appl. Phys. **34**, 2905 (1963).

[111] R. Bauer, E. A. Jägle, W. Baumann, and E. J. Mittemeijer, Philos. Mag. **91**, 437 (2011).

[112] H. Sato, O. Kitakami, T. Sakurai, Y. Shimada, Y. Otani, K. Fukamichi, and I. Introduction, J. Appl. Phys. **81**, 1858 (1997).

[113] O. Kitakami, H. Sato, Y. Shimada, F. Sato, and M. Tanaka, Phys. Rev. B **56**, 849

(1997).

[114] W. Zhang, Z. Liu, Z. Zhang, and G. Wang, Mater. Lett. **91**, 158 (2013).

[115] C. Z. Li and J. C. Lodder, J. Magn. Magn. Mater. **88**, 236 (1990).

[116] D. S. Choi, J. Park, S. Kim, D. H. Gracias, M. K. Cho, Y. K. Kim, A. Fung, S. E. Lee, Y. Chen, S. Khanal, S. Baral, and J. H. Kim, J. Nanosci. Nanotechnol. **8**, 2323 (2008).

[117] K. K. Mehta, T. H. Wu, and E. P. Y. Chiou, Appl. Phys. Lett. **93**, 254102 (2008).

[118] J. M. Park, S. J. Kim, J. H. Jang, Z. Wang, P. G. Kim, D. J. Yoon, J. Kim, G. Hansen, and K. L. DeVries, Compos. Part B Eng. **39**, 1161 (2008).

[119] L. Piraux, J. M. George, J. F. Despres, C. Leroy, E. Ferain, R. Legras, K. Ounadjela, and A. Fert, Appl. Phys. Lett. **65**, 2484 (1994).

[120] G. Beck, K. Petrikowski, and H. Khan, Microstruct. Anal. Mater. Sci. 15-17 (2005).

[121] L. C. Ma, J. M. Zhang, and K. W. Xu, Phys. E Low-Dimensional Syst. Nanostructures **50**, 1 (2013).

[122] A. Akhtari-Zavareh, L. P. Carignan, A. Yelon, D. Ménard, T. Kasama, R. Herring, R. E. Dunin-Borkowski, M. R. McCartney, and K. L. Kavanagh, J. Appl. Phys. **116**, 23902 (2014).

[123] K. Honda and S. Kaya, Sci. Rep. Tohoku Imp. Univ **15**, 721 (1926).

[124] S. Kaya, Sci. Repts. Tôhoku Imp. Univ **17**, 639 (1928).

[125] W. Sucksmith and J. E. Thompson, Proc. R. Soc. A Math. Phys. Eng. Sci. **225**, 362 (1954).

[126] T. Suzuki, D. Weller, C. A. Chang, R. Savoy, T. Huang, B. A. Gurney, and V. Speriosu, Appl. Phys. Lett. **64**, 2736 (1994).

[127] B. Cullity and C. Graham, *Introduction to Magnetic Materials*, 2nd ed. (John Wiley & Sons, 2011).

[128] C. Kittel, Rev. Mod. Phys. **21**, 541 (1949).

[129] L. Landau, E. Lifshitz, and E. Lifshits, Phys. Zeitsch. Der Sow. **169**, 153 (1935).

[130] H. Kronmüller and M. Fähnle, *Magnetism and the Microstructure of Ferromagnetic Solids* (Cambridge University Press, 2003).

[131] H. Hoffmann and F. Steinbauer, J. Appl. Phys. **92**, 5463 (2002).

[132] T. Shinjo, Science **289**, 930 (2000).

[133] W. F. Brown, J. Appl. Phys. **39**, 993 (1968).

[134] R. S. Alex Hubert, *Magnetic Domains* (1998).

[135] J. P. Chen, C. M. Sorensen, K. J. Klabunde, and G. C. Hadjipanayis, Phys. Rev. B **51**, 11527 (1995).

[136] C. Kittel, Phys. Rev. **70**, 965 (1946).

[137] R. W. De Blois, C. D. Graham, R. W. Deblois, C. D. Graham, R. W. De Blois, C. D. Graham, R. W. Deblois, and C. D. Graham, J. Appl. Phys. **29**, 931 (1958).

[138] R. W. De Blois and C. P. Bean, J. Appl. Phys. **30**, S225 (1959).

[139] R. W. De Blois, J. Appl. Phys. **36**, 1063 (1965).

[140] H. R. Khan and K. Petrikowski, MRS Proc. **581**, 245 (1999).

[141] L. Mohaddes-Ardabili, H. Zheng, S. B. Ogale, B. Hannoyer, W. Tian, J. Wang, S. E. Lofland, S. R. Shinde, T. Zhao, Y. Jia, L. Salamanca-Riba, D. G. Schlom, M. Wuttig, and R. Ramesh, Nat. Mater. **3**, 533 (2004).

[142] N. Biziere, C. Gatel, R. Lassalle-Balier, M. C. Clochard, J. E. Wegrowe, and E. Snoeck, Nano Lett. **13**, 2053 (2013).

[143] B. Hillebrands, J. Fassbender, R. Jungblut, G. Güntherodt, D. Roberts, and G. Gehring, Phys. Rev. B **53**, R10548 (1996).

[144] M. Ohtake, O. Yabuhara, J. Higuchi, and M. Futamoto, J. Appl. Phys. **109**, 07C105 (2011).

[145] R. Cowburn, D. Koltsov, A. Adeyeye, M. Welland, and D. Tricker, Phys. Rev. Lett. **83**, 1042 (1999).

[146] A. Tonomura, T. Matsuda, J. Endo, T. Arii, and K. Mihama, Phys. Rev. Lett. **44**, 1430 (1980).

[147] R. P. Cowburn, J. Phys. D. Appl. Phys. **33**, R1 (2000).

[148] M. Miyata, S. Nonoguchi, S. Yakata, H. Wada, and T. Kimura, IEEE Trans. Magn. **47**, 2505 (2011).

[149] A. Bid, A. Bora, and A. K. Raychaudhuri, Phys. Rev. B **74**, 35426 (2006).

[150] N. Stojanovic, D. H. S. Maithripala, J. M. Berg, and M. Holtz, Phys. Rev. B **82**, 75418 (2010).

[151] M. Ohring, *Materials Science of Thin Films* (Academic press, 2001).

[152] M. Schamel, C. Schopf, D. Linsler, S. T. Haag, L. Hofacker, C. Kappel, H. P. Strunk, and G. Richter, Int. J. Mater. Res. **102**, 828 (2011).

[153] T. Yamamoto, H. Nishizawa, and K. Tsuno, Philos. Mag. **34**, 311 (1976).

[154] D. Williams and C. Carter, *Transmission Electron Microscopy: A Textbook for Materials Science*, 3rd ed. (Springer US, 2009).

[155] R. E. Dunin-Borkowski, T. Kasama, A. Wei, S. L. Tripp, M. J. Hÿtch, E. Snoeck, R. J. Harrison, and A. Putnis, Microsc. Res. Tech. **64**, 390 (2004).

[156] H. Lichte and M. Lehmann, Reports Prog. Phys. **71**, 16102 (2008).

[157] D. Gabor, Nature **161**, 777 (1948).

[158] D. Gabor, Proc. R. Soc. London A Math. Phys. Eng. Sci. **197**, (1949).

[159] J. M. Cowley, Ultramicroscopy **41**, 335 (1992).

[160] G. Möllenstedt and H. Düker, Naturwissenschaften **41**, 42 (1955).

[161] E. Völkl, L. F. Allard, and D. C. Joy, *Introduction to Electron Holography* (Springer US, Boston, MA, 1999).

[162] A. Tonomura, Adv. Phys. **41**, 59 (1992).

[163] R. E. Dunin-Borkowski, M. R. McCartney, D. J. Smith, and S. S. P. Parkin, Ultramicroscopy **74**, 61 (1998).

[164] G. Ehrlich and F. G. Hudda, J. Chem. Phys. **44**, 1039 (1966).

[165] R. L. Schwoebel and E. J. Shipsey, J. Appl. Phys. **37**, 3682 (1966).

[166] J. P. Spatz, S. Mössmer, C. Hartmann, M. Möller, T. Herzog, M. Krieger, H. G. Boyen, P. Ziemann, and B. Kabius, Langmuir **16**, 407 (2000).

[167] C. Kappel, Dissertation in Progress, Stuttgart University, n.d.

[168] V. Iota, J. H. P. Klepeis, C. S. Yoo, J. Lang, D. Haskel, and G. Srajer, Appl. Phys. Lett. **90**, 42505 (2007).

[169] G. L. Kellogg, Surf. Sci. Lett. **192**, L879 (1987).

[170] Y. G. Zhou, X. T. Zu, J. L. Nie, and H. Y. Xiao, Surf. Rev. Lett. **15**, 661 (2008).

[171] L. Vitos, A. Ruban, H. Skriver, and J. Kollar, Surf. Sci. **411**, 186 (1998).

[172] H. G. Tompkins and J. A. Augis, Oxid. Met. **16**, 355 (1981).

[173] S. C. Petitto, E. M. Marsh, G. A. Carson, and M. A. Langell, J. Mol. Catal. A Chem. **281**, 49 (2008).

[174] J. B. Newkirk and W. G. Martin, Trans. Am. Inst. Min. Metall. Eng. **212**, 398 (1958).

[175] L. Smardz, U. Köbler, and W. Zinn, J. Appl. Phys. **71**, 5199 (1992).

[176] A. Ashok, A. Kumar, R. R. Bhosale, M. A. H. Saleh, U. K. Ghosh, M. Al-Marri, F. A. Almomani, M. M. Khader, and F. Tarlochan, Ceram. Int. **42**, 12771 (2016).

[177] Y. Gao, L. Song, P. Jiang, L. F. Liu, X. Q. Yan, Z. P. Zhou, D. F. Liu, J. X. Wang, H. J. Yuan, Z. X. Zhang, X. W. Zhao, X. Y. Dou, W. Y. Zhou, G. Wang, S. S. Xie, H. Y. Chen, and J. Q. Li, J. Cryst. Growth **276**, 606 (2005).

[178] H. J. Yang, S. Y. He, and H. Y. Tuan, Langmuir **30**, 602 (2014).

[179] J. B. Wagner, K. R. Lawless, and A. T. Gwathmey, Trans. Metall. Soc. AIME

**221**, 257 (1961).

[180] C. Stockbridge, P. Sewell, and M. Cohen, J. Electrochem. Soc. **108**, 928 (1961).

[181] P. Franke and H. J. Seifert, in *Ternary Steel Syst. Phase Diagrams Phase Transit. Data* (Springer, Berlin, Heidelberg, 2012), pp. 33–33.

[182] L. A. J. Garvie, A. J. Craven, and R. Brydson, Am. Mineral. **79**, 411 (1994).

[183] R. Imlau, A. Kovács, E. Mehmedovic, P. Xu, A. A. Stewart, C. Leidinger, R. E. Dunin-Borkowski, G. Bihlmayer, H. Wiggers, R. Carius, U. Kolb, and M. Luysberg, Phys. Rev. B **89**, 54104 (2014).

[184] H. Jiang, C. S. Petersson, and M.-A. Nicolet, Thin Solid Films **140**, 115 (1986).

[185] L. Stolt, O. Thomas, and F. M. D'Heurle, J. Appl. Phys. **68**, 5133 (1990).

[186] P. Franke and D. Neuschütz, in *Bin. Syst. Part 3 Bin. Syst. from Cs-K to Mg-Zr* (Springer, Berlin, Heidelberg, 2005), pp. 1–3.

[187] A. Gonis, P. E. A. Turchi, and J. Kudrnovský, *Stability of Materials* (Springer, 1994).

[188] P. Franke and D. Neuschütz, in *Bin. Syst. Part 5 Bin. Syst. Suppl. 1* (Springer, Berlin, Heidelberg, 2007), pp. 1–4.

[189] F. C. Frank, Acta Metall. **1**, 15 (1953).

[190] T. Nishizawa and K. Ishida, Bull. Alloy Phase Diagrams **4**, 387 (1983).

[191] R. Kilaas, J. Microsc. **190**, 45 (1998).

[192] H. Shôji, Zeitschrift Für Krist. Mater. **84**, 74 (1933).

[193] Z. Nishiyama, Sci. Rep. Res. Inst. Tohoku Univ. A **25**, 76 (1936).

[194] C. Ensslen, Dissertation in Progress, Karlsruhe Institute of Technology, n.d.

[195] D. Zhang, J.-M. Breguet, R. Clavel, L. Phillippe, I. Utke, and J. Michler, Nanotechnology **20**, 365706 (2009).

[196] A. A. Karimpoor and U. Erb, Phys. Status Solidi **203**, 1265 (2006).

[197] A. Aharoni, J. Appl. Phys. **83**, 3432 (1998).

[198] C. A. F. Vaz, J. A. C. Bland, and G. Lauhoff, Reports Prog. Phys. **71**, 56501 (2008).

[199] D. Weller, G. R. Harp, R. F. C. Farrow, A. Cebouada, and J. Sticht, Phys. Rev. Lett. **72**, 2097 (1994).

[200] D. A. Allwood, G. Xiong, M. D. Cooke, C. C. Faulkner, D. Atkinson, N. Vernier, and R. P. Cowburn, Science **296**, 2003 (2002).

[201] E. R. Lewis, D. Petit, L. O'Brien, A. Fernandez-Pacheco, J. Sampaio, A.-V.

Jausovec, H. T. Zeng, D. E. Read, and R. P. Cowburn, Nat. Mater. **9**, 980 (2010).

[202] M. Kläui, J. Phys. Condens. Matter **20**, 313001 (2008).

[203] L. A. Rodríguez, C. Magén, E. Snoeck, L. Serrano-Ramón, C. Gatel, R. Córdoba, E. Martínez-Vecino, L. Torres, J. M. De Teresa, and M. R. Ibarra, Appl. Phys. Lett. **102**, 22418 (2013).

[204] D. Appy, H. Lei, Y. Han, C. Z. Wang, M. C. Tringides, D. Shao, E. J. Kwolek, J. W. Evans, and P. A. Thiel, Phys. Rev. B **90**, 195406 (2014).

[205] Z. G. Zou, K. Liu, Y. F. Shen, Z. G. Xiao, F. Long, and Y. Wu, Adv. Mater. Res. **415–417**, 368 (2011).

[206] R. A. Munson, Carbon **5**, 471 (1967).

[207] J. S. Chen, S. P. Lau, B. K. Tay, G. Y. Chen, Z. Sun, Y. Y. Tan, G. Tan, and J. W. Chai, J. Appl. Phys. **89**, 7814 (2001).

[208] A. Arya and E. A. Carter, J. Chem. Phys. **118**, 8982 (2003).

[209] P. I. Wang, Y. P. Zhao, G. C. Wang, and T. M. Lu, Nanotechnology **15**, 218 (2003).

[210] A. Zebda, H. Sabbah, S. Ababou-Girard, F. Solal, and C. Godet, Appl. Surf. Sci. **254**, 4980 (2008).

[211] S. Baylan, G. Richter, M. Beregovsky, D. Amram, and E. Rabkin, Acta Mater. **82**, 145 (2015).

[212] B. A. Wacaser, K. A. Dick, J. Johansson, M. T. Borgström, K. Deppert, and L. Samuelson, Adv. Mater. **21**, 153 (2009).

[213] K. N. Tu, Appl. Phys. Lett. **27**, 221 (1975).

[214] E. H. Conrad and T. Engel, Surf. Sci. **299–300**, 391 (1994).

[215] D. Zug, Zeitlicher Verlauf Des Wachstums von Kupferwhiskern, Universität Stuttgart, 2012.

[216] C. Jayaprakash, C. Rottman, and W. F. Saam, Phys. Rev. B **30**, 6549 (1984).

[217] T. Yamamoto, Y. Akutsu, and N. Akutsu, J. Phys. Soc. Japan **57**, 453 (1988).

[218] J. Steiger, D. Kramer, and R. Mönig, J. Power Sources **261**, 112 (2014).

[219] L. E. Murr, Scr. Metall. **6**, 203 (1972).

[220] K. K. Fung, B. Qin, and X. X. Zhang, Mater. Sci. Eng. A **286**, 135 (2000).